Christian Pock

Consistent Combination of Satellite and Terrestrial Gravity Field Observations in Regional Geoid Modeling

A Contribution to Austrian Geoid Computation

Doctoral Thesis

to achieve the university degree of
Doktor der technischen Wissenschaften

submitted to

Graz University of Technology

Supervisor

Univ.-Prof. Dr.-Ing. Torsten Mayer-Gürr
Institute of Geodesy, Graz University of Technology

Graz, November 2016

Affidavit

I declare that I have authored this thesis independently, that I have not used other than the declared sources/resources, and that I have explicitly indicated all material which has been quoted either literally or by content from the sources used. The text document uploaded to TUGRAZonline is identical to the present doctoral thesis.

Date	Signature

Danksagung

Ein herzliches Dankeschön an alle, die mich bei der Erstellung dieser Dissertation unterstützt haben! Insbesondere möchte ich mich bei meinem Doktorvater Univ.-Prof. Dr.-Ing. Torsten Mayer-Gürr bedanken, der mit seinen Ideen den Grundstein für diese Arbeit gelegt hat. Sein kompetenter Rat und die hervorragende Betreuung haben maßgeblich zum Gelingen dieser Dissertation beigetragen. Auch bedanken möchte ich mich für die Freiheiten welche er mir bei der Bearbeitung dieses Forschungsthemas gewährt hat.

Ein weiterer Dank gilt Univ.-Prof. Dr.techn. Mag.rer.nat Roland Pail für die Übernahme der Zweitbegutachtung. Seine wertvollen Ergänzungen haben signifikant zur Qualität dieser Arbeit beigetragen.

Danke auch an meine Kollegen des Instituts für Geodäsie, der Arbeitsgruppe Theoretische Geodäsie und Satellitengeodäsie für die vielen konstruktiven Gespräche. Fehlen wird mir in jedem Fall auch unsere gemeinsame sportliche Pausengestaltung im junior research room.

Bedanken möchte ich mich ebenfalls bei meiner Familie, vor allem bei meiner Frau Claudia für die Geduld, die Liebe und Ihre Unterstützung all die Jahre über!

Abstract

The combination of different gravity field quantities for the purpose of regional gravity field modeling has become a long term tradition in the Austrian scientific community. Numerous initiatives have addressed this issue, whereby the accuracy of today's official geoid solution is in the range of a few centimeters. However, this could only be achieved by means of a non-physical correction surface, which has been used to fit the computed geoid solution to GPS/leveling observations, provided by the Federal Office of Metrology and Surveying (BEV). Disadvantageously, due to this practical approach the geoid can not be considered as a free physical surface any longer.

To overcome this problem, a consistent combination of satellite and terrestrial gravity field observations is needed, and this in turn requires some methodological developments with reference to the Remove-Compute-Restore (RCR) technique. Such a new approach is, for example, the rigorous spectral separation of the different gravity field quantities in order to prevent an overlap in the spectral domain. This leads to a purely physically determined gravimetric geoid, which is on a comparable level of accuracy to the official geoid solution wherein the achieved root mean square (rms) value is 2.80 cm. Furthermore, problems connected to an inhomogeneous input data distribution are also solved. Moreover, the number of usable gravity data was always limited because of numerical stability reasons of the used computation method. Now, the introduced least squares approach with radial basis functions parametrization allows for an increased number of gravity field observations, and a dense spatial distribution of these points is no longer a problem. The variance component estimation method provides a-posteriori weights and thus an optimum relative weighting scheme of different gravity field quantities to each other. It could further be demonstrated, that within the RCR technique the isostatic component is already well represented by a global gravity field model which implies a sufficient choice of the series expansion degree. The so-called full vector approach also represents a methodological development, which means that within the reduction step the magnitude of the computed absolute gravity vector is subtracted from the measured value. Furthermore, an approximated geoid derived from a global gravity field model is introduced to minimize linearization errors.

Additionally, several investigations are part of this thesis. For example, it could be demonstrated how the use of a surface density model improves the computed geoid. The information content of the different gravity field quantities has also been investigated. It has been found that at least three times more gravity measurements than deflections of the vertical are required in order to ensure an equivalent geoid quality. This work has been completed with an estimation of deflections of the vertical maps, which are based purely on reduced gravity data. The validation with measured deflections of the vertical shows rms values of less than 0.61".

Zusammenfassung

Die Kombination von verschiedenen Schwerefeldgrößen für den Zweck der regionalen Schwerefeldmodellierung ist ein Thema, welches einschlägige österreichische Forschungsinstitutionen seit mehreren Jahrzehnten begleitet. Zahlreiche Initiativen beschäftigten sich bereits mit dieser Thematik, wodurch die Genauigkeit des heutigen, offiziellen Geoids im Bereich von wenigen Zentimetern liegt. Dies konnte allerdings nur unter Zuhilfenahme einer nicht physikalischen Korrekturfläche erreicht werden, welche die Lösung an GPS/Nivellement Beobachtungen, bereitgestellt vom Bundesamt für Eich- und Vermessungswesen (BEV), zwängt. Dieser Ansatz hat jedoch den Nachteil, dass damit der physikalische Charakter des Geoids verloren geht.

Basierend auf einer konsistenten Kombination von Satelliten- und terrestrischen Schwerefeldbeobachtungen konnte dieses Problem beseitigt werden, was wiederum Weiterentwicklungen im Rahmen der Remove-Compute-Restore (RCR) Technik voraussetzt. Ein solcher, neuer Ansatz ist beispielsweise die strikte spektrale Trennung der verschiedenen Schwerefeldgrößen, um eine Überlappung der Komponenten im Spektralbereich zu vermeiden. Dadurch konnte ein rein physikalisch bestimmtes Geoid auf dem gleichen Genauigkeitsniveau wie die offizielle, gelagerte Geoidlösung bestimmt werden, wobei der dabei ermittelte root mean square (rms) Wert bei 2.80 cm lag. In weiterer Folge wurden mittels der kleinste Quadrate Methode und einer Parametrisierung über radiale Basisfunktionen die Probleme, die mit einer inhomogenen Datenverteilung einhergehen, gelöst. Bis dato war die Anzahl sowie räumliche Verteilung der nutzbaren Schweremessungen aus rechentechnischen Gründen limitiert. Des weiteren ermöglicht die Varianzkomponentenschätzung eine Bestimmung von a-posteriori Gewichtseinheiten und somit eine optimale relative Gewichtung der verwendeten Schwerefeldgrößen zueinander. Darüber hinaus konnte gezeigt werden, dass die Isostasie bei entsprechender Wahl der Auflösung eines globalen Schwerefeldmodells bereits größtenteils von diesem repräsentiert wird und dadurch in der Geoidberechnung vernachlässigt werden kann. Ebenfalls als methodische Weiterentwicklung zu werten ist der als “full vector approach” bezeichnete Reduktionsschritt, bei dem der Betrag des ermittelten Schwerevektors vom gemessenen Schwerewert abgezogen wird, sowie die Einführung eines Näherungsgeoids, um Linearisierungsfehler zu minimieren.

Durch diverse Untersuchungen konnte unter anderem gezeigt werden, wie vorteilhaft sich die Verwendung eines Oberflächendichtemodells auf die Schwerefeldmodellierung auswirkt. Ebenso wurde auf den Informationsgehalt der verwendeten Schwerefeldgrößen eingegangen. Dabei zeigte sich, dass mindestens dreimal so viele Schwerewerte wie Lotabweichungen benötigt werden, um eine gleichwertige Geoidqualität sicherzustellen. Abgerundet wurde diese Dissertation mit der Schätzung von Lotabweichungskarten für Österreich, welche rein aus den reduzierten Schwerewerten bestimmt wurden, wobei die Validierung mit gemessenen Lotabweichungen rms Werte von weniger als 0.61” ergab.

Contents

1 Introduction and Motivation **1**
1.1 Main Research Goals . . . 2
1.2 Outline of this Thesis . . . 4

2 Height Systems **6**
2.1 Physical Background of Height Systems . . . 6
2.1.1 Equipotential Surface . . . 6
2.1.2 Geopotential Numbers . . . 7
2.2 Important Geodetic Height Systems . . . 8
2.2.1 Orthometric Heights . . . 8
2.2.2 Normal Heights . . . 10
2.2.3 Ellipsoidal Heights . . . 11
2.2.4 Spheroidal Heights . . . 11
2.3 Comparison of Height Systems . . . 13
2.4 General Information on the Austrian Height System . . . 13

3 Fundamentals of Physical Geodesy **17**
3.1 Newtons Law of Gravitation . . . 17
3.2 Important Relations in Physical Geodesy . . . 17
3.3 Spherical Harmonics . . . 20
3.3.1 Topographic/Isostatic Potential in Terms of Spherical Harmonics . . . 21
3.3.2 Atmospheric Potential in Terms of Spherical Harmonics . . . 24
3.4 Potential and Linearization . . . 26
3.4.1 Normal Potential . . . 26
3.4.2 Centrifugal Potential . . . 28
3.4.3 Disturbing Potential . . . 28
3.5 Functionals of the Disturbing Potential . . . 30
3.5.1 Gravity Anomalies . . . 30
3.5.2 Gravity Disturbances . . . 31
3.5.3 Deflections of the Vertical . . . 33
3.5.4 Geoid Heights . . . 34

4 Database for Austrian Geoid Determination **35**
4.1 History of the Austrian Geoid . . . 35
4.1.1 Project GEOnAUT . . . 36
4.1.2 Project GEOID+ . . . 39

4.1.3 Project GARFIELD . . . 41
4.2 Available Gravity Field Quantities for Geoid Computation . . . 42
4.2.1 Gravity Database . . . 42
4.2.2 Deflections of the Vertical . . . 45
4.2.3 GPS/Leveling Observations . . . 48
4.3 Digital Terrain Models . . . 51
4.3.1 Austrian Digital Terrain Model . . . 51
4.3.2 GTOPO Model - Global DTM Coverage . . . 52
4.4 General Aspects of Density Information . . . 53
4.4.1 2D Surface Density Model . . . 54
4.4.2 3D Seismic Density Model . . . 55
4.4.3 Hybrid Density Model . . . 56

5 Least Squares Adjustment 58
5.1 Principles of Least Squares Estimation . . . 58
5.2 Regularization Issues and Variance Components . . . 60
5.2.1 Tikhonov Regularization . . . 61
5.2.2 Variance Component Estimation . . . 63
5.2.3 Building Observation Groups . . . 65

6 Regional Gravity Field Modeling 67
6.1 Remove-Compute-Restore Technique . . . 67
6.2 Remove Step - Smooth the Gravity Field Signal . . . 69
6.2.1 Full Vector Approach . . . 69
6.2.2 Long-Wavelength Reduction and Global Gravity Field Model . . . 70
6.2.3 Short-Wavelength Reduction and Topographic/Isostatic Model . . . 72
6.2.4 Atmospheric Reduction and Atmospheric Density Model . . . 81
6.3 Compute Step - Estimate Gravity Field Quantities . . . 83
6.3.1 Radial Basis Function Parametrization . . . 83
6.3.2 Radial Basis Function Referred to Functionals of the Gravity Field . . . 84
6.3.3 Shape Giving Aspects of Radial Basis Functions . . . 86
6.3.4 Spatial Distribution of Radial Basis Functions . . . 88
6.4 Restore Step - Compute the Solution . . . 90
6.4.1 Long Wavelength Part . . . 91
6.4.2 Topographic/Isostatic Part . . . 92
6.4.3 Atmospheric Part . . . 94

7 Calculation and Results 95
7.1 Reduced Datasets for Gravity Field Estimation . . . 95
7.1.1 Reduced Gravity Data . . . 95
7.1.2 Reduced Deflections of the Vertical . . . 97
7.2 Estimated Residual Geoid Heights . . . 98
7.2.1 Gravimetric Solution . . . 99

7.2.2 Astrogeodetic Solution . . . 100
7.2.3 Combined Solution . . . 102
7.3 Validation Issues . . . 105
7.3.1 Validation of Input Data . . . 105
7.3.2 Gravimetric Solution . . . 106
7.3.3 Astrogeodetic Solution . . . 110
7.3.4 Combined Solution . . . 111
7.4 Selected Investigations . . . 112
7.4.1 Effect of Linearization . . . 112
7.4.2 Effect of Different Density Information . . . 116
7.4.3 Effect of Different DTM Resolutions . . . 118
7.4.4 Effect of Distant Topographic Masses . . . 120
7.4.5 Effect of Different RBF Shapes . . . 121
7.4.6 Effect of Amount of Incorporated Gravity Field Quantities . . . 123
7.4.7 Effect of Isostasy . . . 125
7.5 Estimated Maps of Deflections of the Vertical . . . 126

8 Summary and Recommendations **129**

List of Abbreviations **134**

List of Figures **138**

List of Tables **140**

Bibliography **141**

1 Introduction and Motivation

Knowledge about the Earth's gravity field is important for many scientific applications. In physical geodesy, the geoid acts as a role model for the physical Earth and serves as a reference surface for height systems. Therefore, a precisely determined geoid is essential in order to realize the idea of orthometric heights, derived from the Global Navigation Satellite System (GNSS), which is expected to replace classical geodetic spirit leveling during future decades.

To make a steps towards this idea, the main focus of this thesis is to develop an optimum and consistent combination of terrestrial gravity field data, which consists of absolute and relative gravity measurements as well as deflections of the vertical with the complementary satellite derived Global Gravity field Models (GGM) in order to compute a high quality regional geoid solution. The terrestrial gravity field data contain local components of the gravity field, whereas the satellite data provides global information. These circumstances are very important for the combination of both data types because, the terrestrial data covers mainly the short- to mid wavelengths of the gravity field, whereas a GGM represents the long wavelengths. Especially with reference to the Remove-Compute-Restore (RCR) technique, which provides the framework of geoid computation in this research, this fact has to be considered. In order to simplify the prediction process, the gravity field signal needs to be smoothed in a first step. Due to the influence of topographic masses, which are of mainly of short wavelength character, a highly variable gravity field signal is induced and therefore the influence of the topographic masses needs to be removed from the signal. Furthermore, terrestrial gravity data are usually not available on a global scale. In case of regional gravity field modeling, indeed the data are only used in a restricted area of interest and a GGM is used to model long wavelength effects which are removed from the gravity field signal in advance. The smoothed input data lead to a computation of a residual gravity field, where all previously removed parts need to be restored afterwards in order to establish the final gravity field solution.

A common method for residual gravity field computation is Least Squares Collocation (LSC). This method has also been used for the determination of the official Austrian geoid solution in the year 2007 *(Pail et al, 2008)*. Since that time, for instance, highly accurate global gravity field data from the Gravity field and steady-state Ocean Circulation Explorer (GOCE) satellite mission (2009-2013) has become available *(Drinkwater et al, 2003)*. The scientific goal of this mission was to determine the static Earth gravity field with a geoid height accuracy of about 1-2 cm and a spatial resolution of approximately 80 km. Additionally, the Gravity Recovery and Climate Experiment (GRACE) satellite mission *(Tapley et al, 2004)*, has been collecting gravity field information since the year 2002 and is expected to continue its mission until the

end of 2016. The combined information from mainly these two satellite missions allows for an unprecedented accuracy of the long wavelength component and leads to the high resolution global model GOCO05s *(Mayer-Gürr et al, 2015)*, which is considered as reference GGM in this research. Moreover, Digital Terrain Models (DTM) provided by the Federal Office of Metrology and Surveying (BEV) are available to cover the very high frequent part of the gravity field signal within the central European region. In order to ensure global topographic coverage, a corresponding DTM model is available too.

In this thesis an alternative approach for regional gravity field modeling by means of a least squares estimation process - a Gauss Markov model in association with Radial Basis Functions (RBF) - is used instead of LSC. This new approach for the Austrian gravity field recovery enables the handling of an inhomogeneous input data distribution. Therefore, the amount of data which can be incorporated to a geoid solution increases. The weighting scheme is based on the Variance Component Estimation (VCE) method, which provides a proper relative weighting among different observation groups.

Furthermore, this research follows the idea to incorporate as much information as possible into the gravity field estimation process. This includes the use of all available DTM information, (beyond the Hayford zone of 167 km) and also the full information in terms of degree and order (d/o) provided by a GGM. This in turn will lead to a spectral overlap of long- and short wavelength components within the RCR procedure and in an inconsistent treatment of the gravity field quantities. To avoid this problem, a rigorous separation of the global and local remove and restore step is recommended [see e.g. *(Pock et al, 2014)* or *(Rieser, 2015)*]. By means of a spherical harmonic expansion of the DTM and a proper combination with the GGM, a spectral separation is possible. This finally reveals in a significant improvement of the computed geoid solution. Dividing the topographic masses into a long wavelength and a remaining high frequency part was one of the key applications to remove the inconsistencies between a gravimetric geoid and GPS/leveling measurements, which has always been occurred in previous Austrian geoid computation projects.

Further methodological improvements are based on the introduction of an approximated geoid and replacing the usually used normal gravitational potential of a rotating ellipsoid by introducing a more realistic Taylor point in order to minimize linearization errors. In addition, the incorporation of density information into the computation process, is only one example mentioned at this point to improve the quality of the computed gravity field solutions.

1.1 Main Research Goals

The starting point of this thesis deals with previous Austrian geoid computation initiatives. Despite strenuous efforts, the national geoid solution still suffers from inconsistencies between GPS/leveling observations and the computed gravimetric geoid. As a consequence, the geoid was fitted to GPS/leveling measurements, but disadvantageously the pure physical nature

of the geoid as an equipotential surface is lost. This practical approach follows the requirements specified by the BEV and reveals a highly accurate geoid solution due to the applied constraints.

A main aim of this research is to establish a gravimetric geoid or a combined solution with deflections of the vertical at least on the same level of accuracy as the present national geoid solution but without applying constraints. This is only possible if a proper combination of different gravity field quantities can be found and the reasons for the inconsistencies are identified. One possible reason for this problem is attributed to a spectral overlap in the combination of long wavelength and low frequency satellite derived data, with the medium to high frequency short wavelength data provided by a DTM. This is illustrated in Fig. 1.1. A practical solution to overcome this problem is to introduce a non-physical correction surface which absorbs all inconsistencies in the modeling, but this will not be the approach of this research.

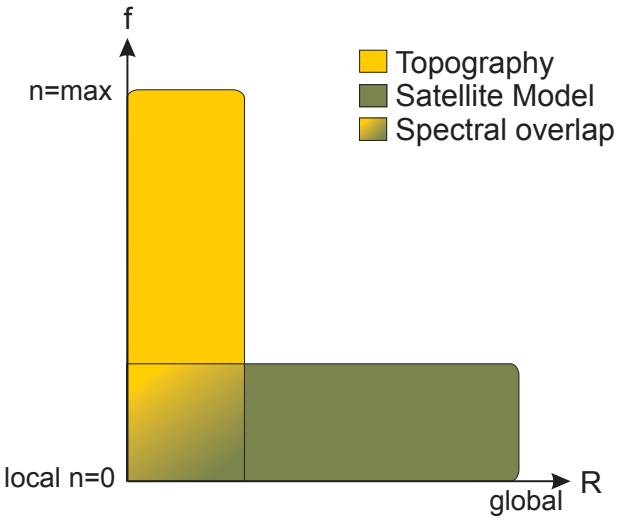

Figure 1.1: Combination of heterogeneous data within the RCR technique and spectral overlap

Apart from this important aim, several methodological developments and their impact on the geoid computation are part of investigations, which are carried out on the example of Austria. The findings can of course be applied to larger areas. Some of the investigated effects have a minor impact on the computed geoid, but some of them are recommended to be considered in the computation in order to improve the geoid quality. This, for example, includes the effect of the atmospheric correction of the gravity field quantities. Another investigation deals with linearization. The introduction of a new Taylor point, represented by an approximated geoid instead of the common ellipsoidal representation, leads to minimized linearization errors in the computation process. In this case the normal gravity field is also exchanged. Further improvements are attributed to a more realistic topographic density assumption and the use of the full gravity vector instead of only the radial derivation of the potential. The effect of a global DTM coverage is also presented. Additionally, the impact of different DTM resolutions on the geoid computation have been investigated. For a combined geoid solution,

the contribution of each gravity field quantity is shown and also the relative weighting scheme of the individual observation groups is discussed in more detail.

For validation purposes, 192 GPS/leveling observations and their corresponding geopotential numbers are available. Additionally, the official Austrian geoid is available on a grid. As a side product, a dense map of deflections of the vertical is estimated and validated with real measured ξ and η quantities. It must be noted, that the achieved results are established within the "Geoid for Austria - Regional gravity FIELD improved" (GARFIELD) project. A second approach within this project was undertaken by *(Rieser, 2015)*, who mainly focused on the LSC method and the combination of terrestrial data with GOCE gravity gradients.

1.2 Outline of this Thesis

At the beginning **chapter 2** provides an overview of relevant height systems which are essential for regional gravity field modeling. Initially, the physical background is presented and after a discussion of important geodetic height systems, the chapter ends with a closer look at special features of the Austrian height system. This leads to corrections which have been applied to the gravity field data in order to obtain the desired orthometric heights.

In **chapter 3** fundamentals of physical geodesy are presented. Important relations and potential theory are discussed in a first step with a special focus on spherical harmonics and its corresponding representation of the Earth gravitational potential. Afterwards, functionals of the disturbing potential and spherical approximation as well as linearization issues are discussed.

An overview about the available database for Austrian geoid determination is presented in **chapter 4**. This includes a historical review, starting from the early beginnings of the Austrian geoid computation and moving through several geoid projects carried out in the recent past. It continues with background information to the national geoid solution. Different relevant input datasets are later discussed in more detail. This is important because these datasets such as gravity measurements or deflections of the vertical, are inhomogeneous and historically compiled. This provides a first indicator of the challenging task of precise regional gravity field modeling. Finally, several density models are presented.

The principles of least squared adjustment are shown in **chapter 5**. The chapter continues with a closer look at the VCE method, as well as the relative weighting and regularization issues. This is also an important discussion, because VCE provides not only a proper weighting between different observation groups, it is also used for the determination of the regularization parameters. Lastly, the obtained observation groups are presented.

The estimation of regional gravity field solutions based on the concept of a least squares approach with RBF parametrization is discussed in **chapter 6**. This new approach for Austrian geoid computation is the backbone of this thesis and represents the compute step within the

RCR procedure. Several effects and results concerning the remove and the restore steps are presented in this chapter. Furthermore, degree variances and their shape controlling character for RBFs are discussed.

The main results of this thesis are presented in **chapter 7**. An initial step shows the reduced input datasets and the resulting residual geoid heights, based on the RBF approach. Next, the achieved results are validated with independent GPS/leveling observations and also with the official Austrian geoid which is given on a grid. Afterwards, the effects of several methodological developments are presented. This also includes small effects on the geoid estimation process, from which a recommendation of whether the single effect is important for precise geoid determination is desired. This holds for manifold investigations which are presented subsequently. At the end of the chapter, estimated maps of deflections of the vertical and their corresponding validation are shown.

Finally, **chapter 8** summarizes the achieved results and makes some recommendations related to the Austrian geoid computation. Some open questions for further gravity field studies are also discussed.

In general, the computation of the results have been undertaken with the Gravity Object Orientated Programming System (GROOPS) software, which was originally developed under the lead of Univ.-Prof. Dr.-Ing. Torsten Mayer-Gürr. The package is equipped with a Graphical User Interface (GUI), based on the Extensible Markup Language (XML) and all C++ routines, developed as part of this thesis are included in the software package. The software interface is shown in Fig. 1.2.

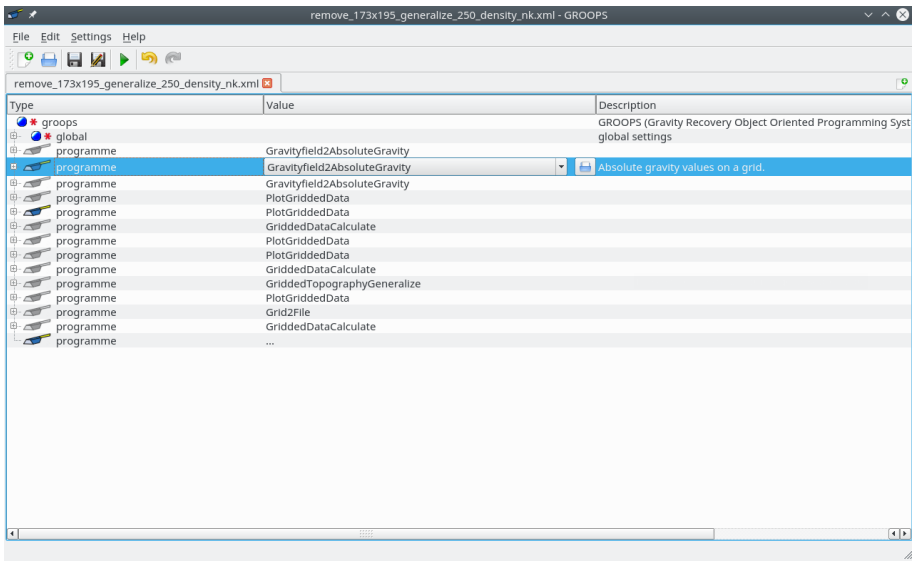

Figure 1.2: Example of GROOPS software interface

2 Height Systems

This chapter discusses different height systems which are important for regional gravity field modeling. At the beginning, the physical background is presented, and due to the fact that heights are closely connected to physical geodesy, these topics can not be easily separated from each other. Furthermore, a closer look at the Austrian height system is more than justified. Due to historical reasons close attention must be paid to some special characteristics and corrections which are recommended for consideration in order to obtain rigorous orthometric heights.

In general, an arbitrary physical height expressed in SI units is defined as

$$\text{Height} = \frac{\text{Potentential difference}}{\text{Gravity}} = \frac{\text{m}^2/\text{s}^2}{\text{m}/\text{s}^2} = [\text{m}] \ .$$

This equation shows that a height depends on the potential difference of a point with respect to the geoid, as well as on gravity. The potential difference is denoted as geopotential number, which in turn is connected to an equipotential surface.

2.1 Physical Background of Height Systems

2.1.1 Equipotential Surface

According to *(Heiskanen and Moritz, 1967)* a surface which is characterized by the same constant potential value is defined as an equipotential surface (see also sec. 3.2). Another characterization is determined by the fact that these surfaces are not parallel to each other, because the passing gravity vector is orthogonal to each equipotential surface. Hence, the corresponding plumb lines are curved, due to mass anomaly and mass inhomogeneity in the interior of the Earth.

The length of such a curved plumb line, starting from the Earth's surface towards the geoid, is referred to as orthometric height H (see sec. 2.2.1) and the Austrian height system is defined by orthometric heights. The relationship between equipotential surface, plumb line and the corresponding gravity vector is illustrated in Fig. 2.1. In general, the geoid as a special equipotential surface is defined as

$$W = W_0 = const. \tag{2.1}$$

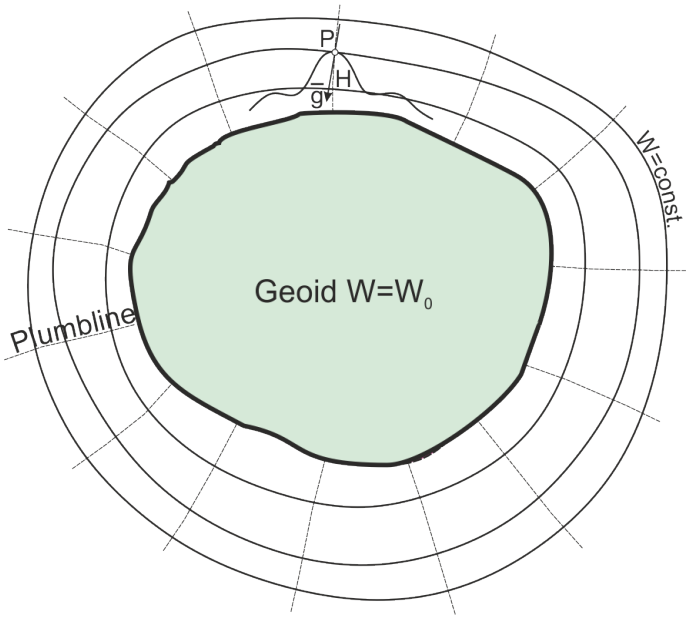

Figure 2.1: Level surfaces and plumb lines; Inspired by *(Hofmann-Wellenhof and Moritz, 2006)*

In a first approximation, a global geoid with constant geopotential W_0 corresponds to the mean sea level and conceptual continuation of the ocean surface underneath the Earth's solid continents *(Hofmann-Wellenhof and Moritz, 2006)*.

2.1.2 Geopotential Numbers

A single geopotential number C is defined as the potential difference between two points connected by spirit leveling. It can be obtained by precise spirit leveling, in combination with gravity measurements along the leveling line. If the potential difference is given between a point P, located on the Earth's surface, and the geoid, the following relationship is valid

$$C = W_0 - W_P = -\Delta W = \int_0^P g \; dn \approx \sum_0^P \Delta n \; \cdot g_0 \; , \tag{2.2}$$

where Δn is the height difference obtained by spirit leveling and g_0 denotes the measured gravity. The physical dimension of a geopotential number is $[m^2/s^2]$ and it is characterized as path-independent.

Different heights may be obtained by means of dividing the geopotential number with different gravity definitions. This demonstrates how the geopotential number is converted into a length unit. Related to this work, geopotential numbers are also used for validation purposes. The potential is independent of an error related to the ellipsoidal height and may provide an indicator for the quality of the corresponding GPS/leveling observations. If the potential and geoid height deviations are on the same level of accuracy, the corresponding ellipsoidal height

of the GPS/leveling measurement is reliable and the main part of the error is supposed to be in the orthometric height component.

2.2 Important Geodetic Height Systems

2.2.1 Orthometric Heights

The orthometric height H is defined as height above the geoid measured along the curved plumb line. Through examination of Fig. 2.2 the orthometric height is seen as the plumb line segment between a point P located on the Earth's surface and the geoid point P_0. This segment is curved since the equipotential surfaces are not parallel (see sec. 2.1.1). The orthometric height is mathematically defined as

$$H = \frac{C}{\overline{g}} \ , \tag{2.3}$$

where the geopotential number of the point P is determined as $C = W_0 - W_P$. The mean gravity as the average value of gravity along the plumb line reads

$$\overline{g} = \frac{1}{H} \int_0^H g(H) \ dH \ , \tag{2.4}$$

where $g(H)$ denotes the actual gravity of a variable point at any height.

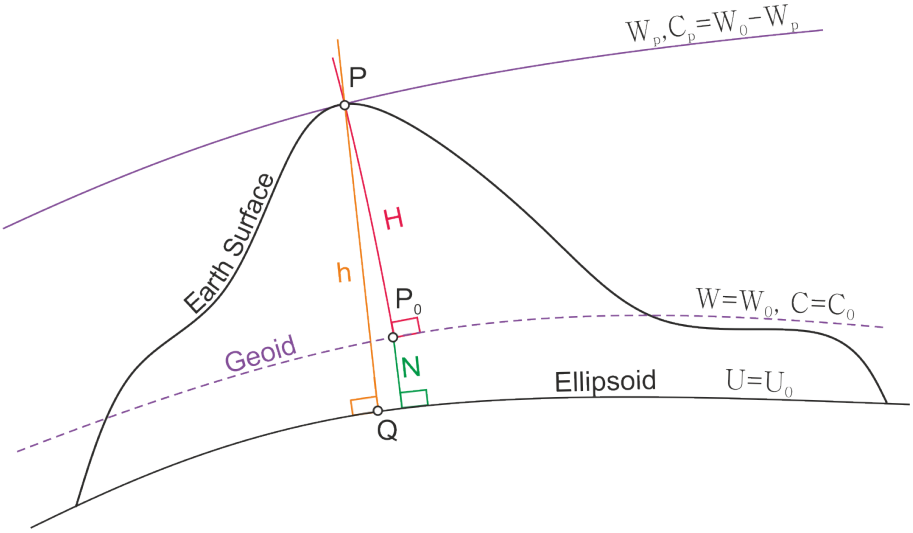

Figure 2.2: General definition of the ellipsoidal height h, the orthometric height H and the geoid height N

The rigorous computation of the mean gravity value $\overline{g}$ along the plumb line is impossible because this requires knowledge about the complete mass and density distribution of the Earth's crust. Therefore, the orthometric height is not determined rigorously. Different ways to derive the mean gravity on purely hypothetical assumptions are based on following prominent approaches:

- Prey-Poincare: $\overline{g} = g + 0.0424\ H$ (g $[gal]$, H $[km]$),
- Helmert: $\overline{g} = g + (0.3086 - 0.08382\sigma)\frac{H}{2}$ (g $[gal]$, σ $[g/cm^3]$, H $[km]$),
- Mader: $\overline{g} = \frac{1}{2}(g + g_0)$, ($g$, g_0 $[gal]$).

The latter approach presupposes that the gravity varies only linearly along the plumb line which is only an approximation of reality.

In case of the Austrian orthometric height system, the Federal Office of Metrology and Surveying (BEV) decided to follow their own approach, tailored to the needs of the special topographic situation within Austria. In general, the mean gravity determination is based on the Prey-Poincare method but with some refinements. The computation is divided into three steps:

1. Remove the impact of the masses onto point P,
2. compute the gradient correction to point P',
3. restore the masses in point P'.

The point P' can be any arbitrary point along the plumb line. The computation of the mean gravity is critical, because the mass effects do not vary linearly along the plumb line which leads to errors in orthometric heights. Moreover, also the mean gravity value along the plumb line computed from Prey-Poincare does not match the modeling requirements *(Ruess, 2001)*. Several refinements related to gravity weighting and different numbers of nodal points along the plumb line have been investigated by the BEV. The optimum results are achieved for points with a height of < 1400 m by using a weighted Kepler integral approach based on three weighted nodal points. For heights > 1400 m a Simpson integral approach based on five weighted nodal points is required which leads to minimized gravity errors of < 1.1 mgal *(Ruess, 2001)*. Further details related to this topic can be found in e.g. *(Meurers et al, 2001)*.

The geoid height N is geometrically defined as the difference between the ellipsoidal height h and the orthometric height H (see Fig. 2.2). Depending on the chosen reference ellipsoid which represents an idealized figure of the Earth, global geoid variations up to $\pm$ 100 m occur. The geoid, which is a special equipotential surface (see sec. 2.1.1), is irregular in its shape but considerably smoother than the physical Earth topography and coincides with the ocean surface in a first approximation. The geoid height is given as

$$N = h - H \ . \tag{2.5}$$

From this point of view the geoid represents a combination of a geometrical quantity h, obtained from Global Positioning System (GPS) measurements and a physical quantity H, based on spirit leveling in combination with gravity measurements. If two of the quantities in Eq. (2.5) are known, the third can be computed immediately, due to this linear relationship. This is the basic idea of the GPS/leveling concept (see sec. 4.2.3). Therefore, an important aspect is the computation of centimeter and sub-centimeter geoid solutions. One may conclude, if the geoid is accurate enough, the spirit leveling can be omitted and the orthometric height is calculated directly. This would represent a significant progress in the field of geodesy, because spirit leveling is a very time consuming work.

2.2.2 Normal Heights

It is also possible to define a height H_N, which avoids a density hypothesis for the Earth's crust. This was shown for the first time by *M.S. Molodensky* who introduced this method of determining the physical surface of the Earth. It can be calculated through introducing an approximation of the real gravity field by a normal reference field with normal potential. In this case, all physical quantities can be calculated in a rigorous mathematical process.

Conventionally, normal heights are defined as measured values starting from a point P, on the Earth's surface along the plumb line towards a point P_0, on the quasigeoid. The quasigeoid is smoother compared to the geoid, but has no physical meaning *(Heiskanen and Moritz, 1967)*. In Austria the differences to the geoid are of approximately ± 30 cm, based on the quasigeoid solution of *(Denker and Torge, 1998)*. The normal height is mathematically defined as

$$H_N = \frac{C}{\overline{\gamma}} \ , \tag{2.6}$$

where C is the potential difference in point P. The mean normal gravity $\overline{\gamma}$ along the plumb line is given as

$$\overline{\gamma} = \frac{1}{H_N} \int_0^{H_N} \gamma(H_N) \, dH_N \ , \tag{2.7}$$

where $\gamma(H_N)$ is the gravity according to (3.40). Furthermore, the difference between the ellipsoidal height and the normal height is denoted as height anomaly ζ

$$\zeta = h - H_N \ , \tag{2.8}$$

where in turn the relationship to the orthometric height H can be found by

$$N - \zeta = H_N - H \ . \tag{2.9}$$

2.2.3 Ellipsoidal Heights

If points, located on Earth's surface are determined with respect to a reference ellipsoid, they are categorized as ellipsoidal or sometimes also denoted as geodetic coordinates φ and λ, respectively. This pair of coordinates is referred to a corresponding ellipsoidal height h, which is connected to an ellipsoid of revolution, completing the coordinate triple. This ellipsoid is more appropriate to approximate the Earth shape, compared to an ordinary sphere. For applications as GPS, the Word Geodetic System-84 (WGS-84) was established. The corresponding WGS-84 ellipsoid parameters are presented in Tab. 2.1.

Table 2.1: Parameters of the WGS-84 ellipsoid *(Hofmann-Wellenhof and Moritz, 2006)*

Parameter	**Value**	**Meaning**
a	6378137 $[m]$	semi-major axis of ellipsoid
GM	$3986004.418 \cdot 10^8$ $[m^3 s^{-2}]$	Earth grav. constant $\times$ mass
w	$7292115 \cdot 10^{-11}$ $[rad\ s^{-1}]$	Earth angular velocity
f	1/298.257223563	ellipsoid flattening

The ellipsoidal height is independent of the Earth's gravity field, because it is defined in a purely geometrical sense. Nevertheless, it depends on the chosen reference ellipsoid, because h is defined as height above the ellipsoid (see Fig. 2.2). From a historical point of view, WGS-84 is based on the GRS80 reference system *(Moritz, 1980b)*. The reference ellipsoid of WGS-84 differs slightly from GRS80 due to later refinements. Most of these refinements are essential for high-precision satellite orbit calculation, but have a rather small effect on terrestrial applications.

2.2.4 Spheroidal Heights

The Austrian height system is characterized by differences between rigorously defined orthometric heights H (see sec. 2.2.1) and so-called "MGI Gebrauchshöhen", denoted as $H_{sph.}$, which have the character of an orthometric height but are effected by systematic errors due to historical reasons. The use of spheroidal heights, also sometimes denoted as normal-orthometric heights, is a result of the fact that real gravity measurement along the leveling line could not always be carried out in the 19^{th} century. This holds true especially for measurements in mountainous regions. Therefore, the normal gravity along the spirit leveling line, denoted as γ^*, is computed and the spheroidal heights are obtained from normal geopotential numbers C^*. A spheroidal height is defined as

$$H_{sph.} = \sum_{0}^{P} \Delta n \cdot \frac{\gamma^*}{\overline{\gamma}} = \frac{C^*}{\overline{\gamma}} \ , \tag{2.10}$$

where the combination of the geometrically defined normal gravity and the measured height differences Δn, which is physically defined, can not be clearly classified either as a physical or geometrical quantity anymore. Finally, division by the mean normal gravity $\overline{\gamma}$ converts it into a spheroidal height.

This height can only be interpreted as an approximation of an orthometric height because of missing real physical gravity measurements. The height definition of Eq. (2.10) is the basis for many products, distributed by the BEV. This is important because it also includes the Austrian gravity data, which are originally related to spheroidal heights. The transition from spheroidal to orthometric heights is discussed in sec. 2.4.

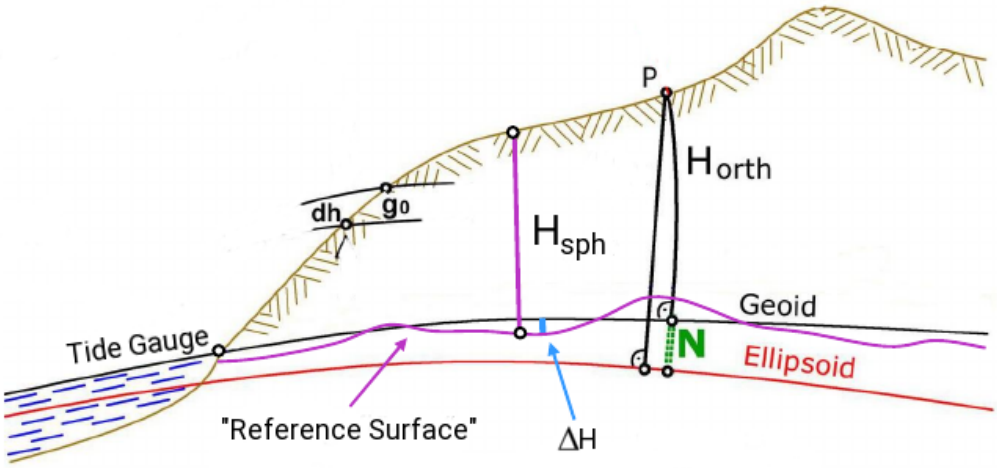

Figure 2.3: Special characteristics of the Austrian height system - The reference surface is connected to spheroidal heights whereas the orthometric heights are related to the geoid. The deviation from spheroidal to the orthometric heights, which are needed for geoid determination is denoted as ΔH. [courtesy by BEV[1]]

[1] www.bev.gv.at

2.3 Comparison of Height Systems

Each height system has its own characteristic. By means of the geopotential number C, defined in Eq. (2.2), it is possible to obtain different kinds of heights, depending on the chosen gravity value. In particular, this leads to

- Orthometric heights: $\overline{g}$,
- Normal heights: $\overline{\gamma}$.

In theory, this gives an unlimited number of height systems by calculating the gravity in slightly different ways. Focusing on the height systems treated in this chapter, one can state that unlike orthometric heights, normal heights can be determined exactly and without any hypothesis. Another aspect is that normal heights are as accurate as the geopotential numbers because the normal gravity can be calculated in a rigorous mathematically manner. For the definition of a national height reference system, orthometric heights as well as normal heights are suitable. For example, the German height system is related to normal heights. Both heights are based on geopotential numbers and therefore defined path-independent. Related to this, an important difference is that the geoid has a physical meaning, whereas the quasigeoid which is connected to normal heights does not. A short summary of the different height systems discussed in this chapter is presented in Tab. 2.2.

Table 2.2: Characterization of different height systems *(Marti and Schlatter, 2002)*

Criteria	**Geop. number**	**Orthometric**	**Ellipsoidal**	**Normal**
Notation	C	H	h	H_N
SI-unit	m^2/s^2	m	m	m
Hypothesis-free	yes	no	yes	yes
Reference	geoid	geoid	ellipsoid	quasigeoid
Determination	spirit leveling	spirit leveling	GNSS	spirit leveling
Gravity meas.	yes	yes	no	yes

2.4 General Information on the Austrian Height System

The Austrian height system has historically developed, and is grounded on measurements conducted by the Militär- Geographisches Institut (MGI). This spirit leveling and the height system is connected with the Mediterranean sea. The corresponding reference point was defined as the local sea level in the year 1875 at Molo Sartorio, Trieste, Italy. All Austrian heights are originally related to this fundamental point. In 1923 the MGI was replaced by the newly established Federal Office of Metrology and Surveying (BEV). After the war the Austrian height system was still connected to Molo Sartorio but the reference point for new

spirit leveling campaigns had changed to Bruck/Fusch, Salzburg, where a spheroidal height (see sec. 2.2.4) representation was available at the train station building. After 1962 modern measurement equipment has become available and old measurements were replaced and during 1966-2001 steady improvements have been applied to the height system.

The Austrian spirit leveling is linked with international measurement campaigns. Under the lead of the German Federal Agency for Cartography and Geodesy (BKG) there is currently work in progress to unify the different height systems within Europe. This initiative is called the United European Leveling Network (UELN) and is connected to the tide gauge datum point of Amsterdam, The Netherlands. The differences of the manifold height systems, with respect to this datum point with its realization in the EVRS2007 system, are illustrated in Fig. 2.4. More details on this topic can be found in *(Sacher et al, 1999)* or *(Mäkinen, 2008)*.

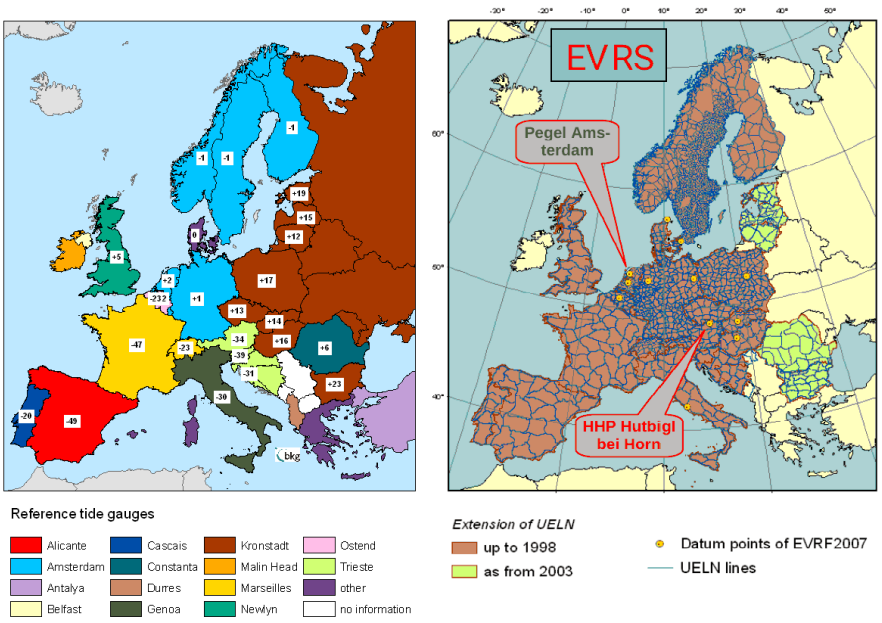

Figure 2.4: National reference levels with respect to the EVRS2007 [cm] (left); Realization of the UELN-net and 11 reference points of the EVRS2007, where one of this points is located within Austria (right) [courtesy by BKG[2]]

Based on overlapping spirit leveling measurements collected during the last 70 years, a vertical height change in Austria has been observed by the BEV. A map providing information on the velocity of the height change per year is shown in Fig. 2.5. Currently, the BEV is working on a kinematic height adjustment based on all available spirit leveling observables in order to provide to the community time dependent geopotential numbers and their corresponding vertical velocity. These time dependent changes are a potential error source, especially for GPS/leveling observations, because the Austrian spirit leveling is not carried out within a single measurement epoch and is therefore affected by such a height change.

[2] www.bkg.bund.de

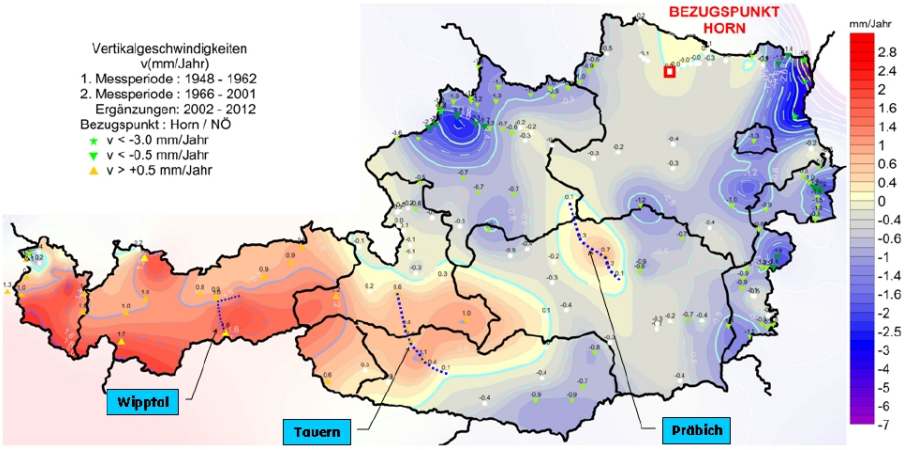

Figure 2.5: Vertical changes over the last 70 years derived from redundant spirit leveling measurements [mm/year]; *(Ruess and Mitterschiffthaler, 2015)*

The height differences occurring between Austria and neighbouring countries are shown in Fig. 2.6. These differences must be considered in case of any cross-border projects.

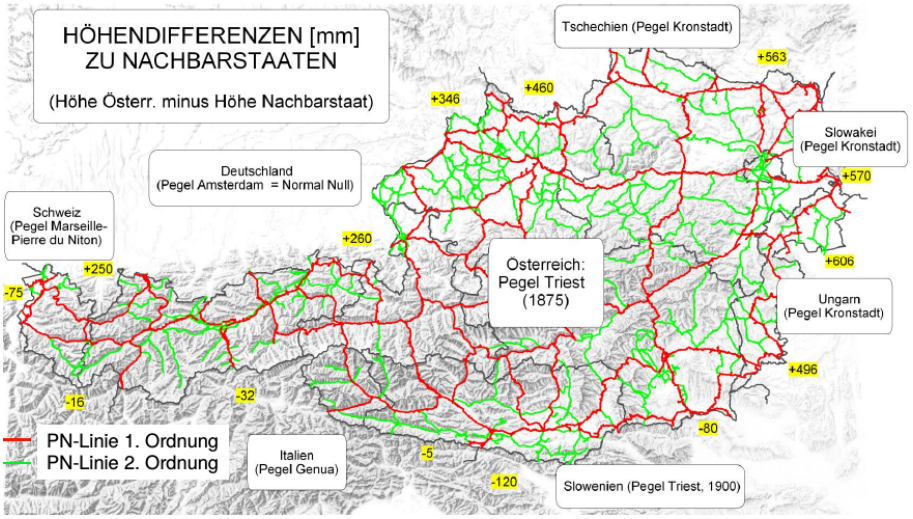

Figure 2.6: Differences between the Austrian height system and the neighbouring counties [mm]; [courtesy by BEV[3]]

For Austrian geoid computation the orthometric height is of special interest because it defines the official height system. The gravity measurements are connected to spheroidal heights and a transition from spheroidal to orthometric heights is needed.

[3] www.bev.gv.at

Transition from Spheroidal to Orthometric Heights

For the transition of the spheroidal heights to orthometric heights the BEV provides a transformation grid where every grid point is assigned with an individual ΔH value (see sec. 2.2.4). The orthometric heights are the desired quantity related to the geoid computation but the measured gravity is originally related to spheroidal heights. The transformation to a rigorous orthometric heights is given as

$$H = H_{sph.} + \Delta H \ , \tag{2.11}$$

where, in a practical approach, ΔH is computed using a third degree polynomial to interpolate the positions of the gravity measurements. In a first step, the corresponding heights of all gravity measurements within Austria are transformed. The occurring height changes are shown in Fig. 2.7. The corrections for the gravity measurements located in the western part of Austrian are smaller because of the geographical location which is closer to Molo Sartorio.

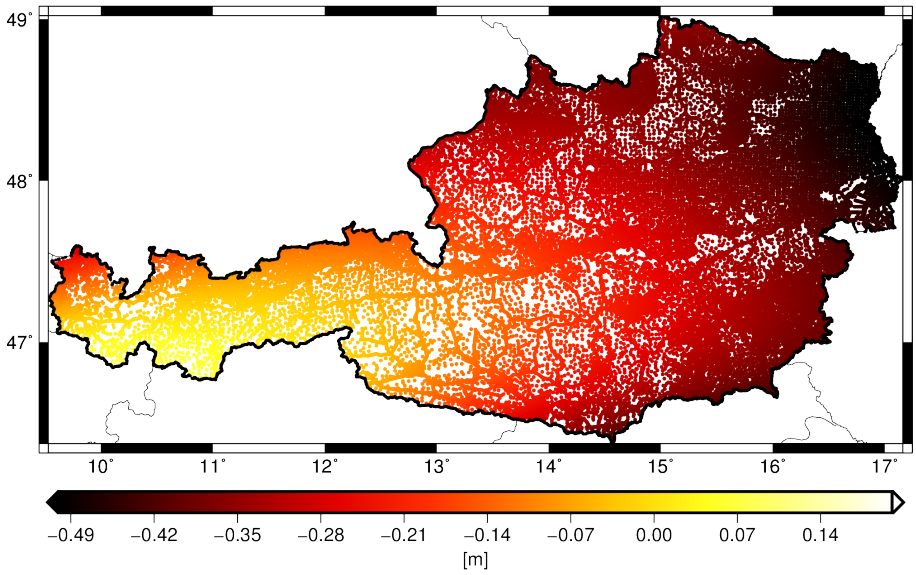

Figure 2.7: Applied height differences ΔH to the gravity stations within Austria based on the BEV transformation grid

The range of the height corrections is -0.5 m to 0.2 m and has been applied to all gravity stations within Austria. The BEV specifies the accuracy of the height grid of approximately 6 cm. Due to the lack of information for neighbouring countries, no corrections are applied and the heights are assumed to be orthometric. A detailed description how to perform the transformation and many more details related to the Austrian height system can be found in *(Briese et al, 2011)*.

3 Fundamentals of Physical Geodesy

In this chapter the fundamentals of physical geodesy are presented. This work follows the ideas of *Torben Krarup*, *Aleksanteri Heiskanen* and *Helmut Moritz (Heiskanen and Moritz, 1967)*, who are three prominent pioneers in the field of physical geodesy. Hence, important parts from those works, with a connection to this thesis, are described in a compact way.

3.1 Newtons Law of Gravitation

This section provides a basic summary of potential theory. On the basis of Newton's law of gravitation, the force of attraction between two bodies with mass m_1 and with mass m_2 at distance r from each other is given as

$$F = G\frac{m_1 m_2}{r^2} \ , \tag{3.1}$$

with the Newtons gravitational constant $G = (6.6742 \ \pm 0.0010) \cdot 10^{-11} m^3/kg \ s^2$. The combination of Eq. (3.1) with Newton's second law $F = ma$, which is valid in case of constant masses, provides the acceleration of the body of mass m_1 with respect to the center mass of both bodies according to

$$a = \frac{Gm_2}{r^2} \ . \tag{3.2}$$

In case of the equivalence principle, a vector representation of the acceleration $\boldsymbol{a}$ or $\boldsymbol{g}$ can be obtained by deriving the acceleration from a scalar function denoted as gravitational potential V (see sec. 3.2). For the exterior of the Earth, the Laplace equation is valid and the gravitational potential can be expressed by spherical harmonic functions. This is essential and gives the starting point for the development of different potentials in terms of spherical harmonics as it is done in this chapter. A basic introduction to spherical harmonics is given in sec. 3.3.

3.2 Important Relations in Physical Geodesy

Initially, forces or accelerations acting on an arbitrary body located on the Earth's surface must be defined. The two main accelerations are the gravitational acceleration $\boldsymbol{g}_{grav}$ caused by the gravitational attraction of Earth's mass, and the centrifugal acceleration $\boldsymbol{g}_{acc}$ which is

caused by Earth's rotation. The latter depends directly on the distance to the Earth rotation axis and reaches its maximum at the equator, whereas at the poles the centrifugal acceleration vanishes. An Earth located gravimeter is also affected by these forces. Additionally, masses in the solar system (e.g. sun and moon) must also be considered, because they are introducing a time-varying field due to their motion relative to the Earth. In potential theory all masses are generating potentials. On the one hand, the gravitational potential V and on the other hand, the centrifugal potential Φ exists, which in turn are causing accelerations. In a first step, the combination of gravitational acceleration and centrifugal acceleration is denoted as gravity vector $\boldsymbol{g}$ and it follows

$$\boldsymbol{g} = \boldsymbol{g}_{grav} + \boldsymbol{g}_{cen} \ , \tag{3.3}$$

where every single acceleration is equipped with an associated potential. The Earth's gravity potential is then given according to

$$W = V + \Phi \ . \tag{3.4}$$

In general, a potential is defined as work which is needed to transport a mass from a certain point to infinity *(Heiskanen and Moritz, 1967)*. In a geodetic sense, such an equipotential surface (see sec. 2.1.1) is denoted as geoid if it coincides with the mean sea surface. It serves as a reference surface for height systems. The gravity vector $\boldsymbol{g}$ can be expressed by the gradient operator applied on the Earth's gravity potential W

$$\boldsymbol{g} = \nabla W = \begin{pmatrix} \frac{\partial W}{\partial x} \\ \frac{\partial W}{\partial y} \\ \frac{\partial W}{\partial z} \end{pmatrix} \ . \tag{3.5}$$

The magnitude of the gravity acceleration vector $\|\boldsymbol{g}\|$ provides the scalar absolute gravity value. Gravity has the physical dimension of an acceleration and is, due to historical reasons, measured in *gal*, named after *Galilio Galilei*. The link to SI units is given with

$$1 \ gal = 0.01 \ m/s^2 \ . \tag{3.6}$$

The same relation also holds for the gravitational potential V, where the derivatives are related to the components of the gravitational acceleration according to

$$\boldsymbol{g}_{grav} = \nabla V = \begin{pmatrix} \frac{\partial V}{\partial x} \\ \frac{\partial V}{\partial y} \\ \frac{\partial V}{\partial z} \end{pmatrix} \ . \tag{3.7}$$

This also holds true for the centrifugal potential which is described in more detail in sec. 3.4.2. For several point masses the superposition principle is valid

$$V = \frac{Gm_1}{l_1} + \frac{Gm_2}{l_2} + \cdots + \frac{Gm_n}{l_n} = G\sum_{i=1}^{n} \frac{m_i}{l_i} \ , \tag{3.8}$$

where G is the gravitational constant and m_i the mass of the attracting point. The Euclidean distances are denoted with l_i. Assuming a continuous mass distribution and a corresponding density ρ, the gravitational potential can be expressed as Newtonian volume integral formula according to

$$V = G \iiint_{\Omega} \frac{\rho}{l} \, d\Omega \ . \tag{3.9}$$

Furthermore, a point which is located outside the masses fulfills the Laplace equation which is characterized as harmonic

$$\Delta V = \frac{\partial^2 V}{\partial x^2} + \frac{\partial^2 V}{\partial y^2} + \frac{\partial^2 V}{\partial z^2} = 0 \ . \tag{3.10}$$

This in turn provides the opportunity to represent the exterior potential by spherical harmonics (see sec. 3.3). For the interior potential, the Poisson equation is valid because of non-vanishing density according to

$$\Delta V = -4\pi G\rho \ . \tag{3.11}$$

More details on interior and exterior potentials can be found in sec. 3.3.1. The general topic of potential theory is characterized as fundamental knowledge in physical geodesy and is well documented in literature [cf. *(Moritz, 1980a)* or *(Hofmann-Wellenhof and Moritz, 2006)*].

3.3 Spherical Harmonics

Due to the fact that the exterior potential is characterized as harmonic, the gravitational potential V can be expanded into spherical harmonics. One possible way to solve the Laplace equation [Eq. (3.10)] is to express it in terms of spherical coordinates. The Laplace equation is a partial differential equation of 2^{nd} order, and expressed in terms of spherical coordinates it follows

$$r^2\frac{\partial^2 V}{\partial r^2} + 2r\frac{\partial V}{\partial r} + \frac{\partial^2 V}{\partial \vartheta^2} + \cot\vartheta\frac{\partial V}{\partial \vartheta} + \frac{1}{\sin^2\vartheta}\frac{\partial^2 V}{\partial \lambda^2} = 0 \ . \tag{3.12}$$

Two possible solutions of this differential equation are given for the interior $[^i]$ and the exterior $[^e]$ potential of a unit sphere as

$$V^i(r,\vartheta,\lambda) = \sum_{n=0}^{\infty} r^n Y_n(\vartheta,\lambda) \ , \tag{3.13}$$

$$V^e(r,\vartheta,\lambda) = \sum_{n=0}^{\infty} \frac{1}{r^{n+1}} Y_n(\vartheta,\lambda) \ , \tag{3.14}$$

with $Y_n(\vartheta,\lambda)$ as the Legendre surface spherical harmonics, which in turn can be reformulated to the following equations, either

$$Y_n(\vartheta,\lambda) = P_{nm}(\cos\vartheta)\cos m\lambda \ , \tag{3.15}$$

or

$$Y_n(\vartheta,\lambda) = P_{nm}(\cos\vartheta)\sin m\lambda \ , \tag{3.16}$$

where the P_{nm} are the associated Legendre functions and n and m denote the degree and order. The Legendre functions can be found according to

$$P_{nm}(t) = (1-t^2)^{\frac{m}{2}}\frac{d^m P_n(t)}{dt^m} \quad \text{with} \quad P_n(t) = \frac{1}{2^n n!}\frac{d^n}{dt^n}(t^2-1)^n \quad \text{and} \quad t = \cos\vartheta \ . \tag{3.17}$$

After a combination of all possible solutions of the differential equation, the Laplace series reads

$$Y_n(\vartheta,\lambda) = \sum_{n=0}^{\infty}\left[c_{nm}P_{nm}(\cos\vartheta)\cos m\lambda + s_{nm}P_{nm}(\cos\vartheta)\sin m\lambda\right] \ , \tag{3.18}$$

where the c_{nm} and s_{nm} coefficients are arbitrarily chosen in a first step. Later, the coefficients from e.g. a Global Gravity field Model (GGM) or the topographic potential coefficients will be used in the calculation. In general, after combining Eq. (3.18) with Eq. (3.15) and Eq. (3.16), two different representations in terms of interior and exterior potential are found

$$V^i(r,\vartheta,\lambda) = \sum_{n=0}^{\infty} r^n \sum_{m=0}^{n} \left[c_{nm} \underbrace{P_{nm}(\cos\vartheta)\cos m\lambda}_{C_{nm}} + s_{nm} \underbrace{P_{nm}(\cos\vartheta)\sin m\lambda}_{S_{nm}} \right] , \tag{3.19}$$

$$V^e(r,\vartheta,\lambda) = \sum_{n=0}^{\infty} \frac{1}{r^{n+1}} \sum_{m=0}^{n} \left[c_{nm} \underbrace{P_{nm}(\cos\vartheta)\cos m\lambda}_{C_{nm}} + s_{nm} \underbrace{P_{nm}(\cos\vartheta)\sin m\lambda}_{S_{nm}} \right] . \tag{3.20}$$

It is possible to write both equations in a more compact notation by taking fully normalized Legendre functions denoted as $\bar{P}_{nm}$, into account [see *(Hofmann-Wellenhof and Moritz, 2006, p.23)*]. This leads to

$$V^i(r,\vartheta,\lambda) = \sum_{n=0}^{\infty} r^n \sum_{m=-n}^{n} \bar{a}^i_{nm} \bar{Y}_{nm}(\vartheta,\lambda) , \tag{3.21}$$

$$V^e(r,\vartheta,\lambda) = \sum_{n=0}^{\infty} \frac{1}{r^{n+1}} \sum_{m=-n}^{n} \bar{a}^e_{nm} \bar{Y}_{nm}(\vartheta,\lambda) , \tag{3.22}$$

where the difference is again only attributed to the distance r, which is either inside or outside the attracting masses. Finally, introducing boundary conditions according to *(Hofmann-Wellenhof and Moritz, 2006, p.27, p.56)*, to Eq.(3.19) and Eq.(3.20), the following expressions are found

$$V^i(r,\vartheta,\lambda) = \frac{GM}{R} \sum_{n=1}^{\infty} \left(\frac{r}{R}\right)^n \sum_{m=0}^{n} \bar{a}^i_{nm} \bar{Y}_{nm}(\vartheta,\lambda) , \tag{3.23}$$

$$V^e(r,\vartheta,\lambda) = \frac{GM}{R} \sum_{n=1}^{\infty} \left(\frac{R}{r}\right)^{n+1} \sum_{m=0}^{n} \bar{a}^e_{nm} \bar{Y}_{nm}(\vartheta,\lambda) . \tag{3.24}$$

3.3.1 Topographic/Isostatic Potential in Terms of Spherical Harmonics

In general, spherical harmonic coefficients in the spectral domain represent the global structure and the irregularities of the geopotential field. If it is required to express the geopotential field in terms of spherical harmonics, first the fundamental Newtonian integral formula for the gravitational potential is given according to Eq. (3.9). A closed solution of the triple integral

is impossible, due to the unknown density and mass distribution inside the Earth. Taking into account that the solid spherical harmonics are an orthogonal set of solutions, which are satisfying the Laplace equation represented in a system of spherical coordinates, the reciprocal distance between integration point Q and computation point P can be expressed as a series of Legendre polynomials *(Heiskanen and Moritz, 1967)*. Now the addition theorem of spherical harmonics can also be applied [see e.g. *(Hobson, 1931)* or *(Freeden, 1985)*]. Finally, the equation which connects the spatial and spectral domains of the interior potential, in a fully normalized representation is given according to

$$V^i(P) = \frac{GM}{R} \sum_{n=1}^{\infty} \left(\frac{r}{R}\right)^n \sum_{m=-n}^{n} \underbrace{\frac{1}{M(2n+1)} \iiint_{\Omega} \left(\frac{R}{r'}\right)^{n+1} \bar{Y}_{nm}(Q)\rho(Q)d\Omega(Q)}_{\bar{a}^i_{nm}} \bar{Y}_{nm}(P) \ , \tag{3.25}$$

where the fully normalized coefficients $\bar{a}^e_{nm}$ are of interest. This also holds for the exterior potential. Analogously to the interior potential it follows

$$V^e(P) = \frac{GM}{R} \sum_{n=1}^{\infty} \left(\frac{R}{r}\right)^{n+1} \sum_{m=-n}^{n} \underbrace{\frac{1}{M(2n+1)} \iiint_{\Omega} \left(\frac{r'}{R}\right)^{n} \bar{Y}_{nm}(Q)\rho(Q)d\Omega(Q)}_{\bar{a}^e_{nm}} \bar{Y}_{nm}(P) \ , \tag{3.26}$$

These two equations, Eq. (3.25) and Eq. (3.26), are the basis for the development of spherical harmonics based on topographic, isostatic or the atmospheric potential.

In the following, a detailed explanation on how the topographic potential may be expressed in terms of spherical harmonics is provided. This approach and its implementation is of essential interest, in order to avoid a double consideration of the topographic/isostatic masses within the Remove-Compute-Restore (RCR) procedure. The gravitational potential coefficients derived from topography in the spectral domain are computed from a Digital Terrain Model (DTM). After applying the series expansion for the inverse distance $\frac{1}{l}$ and introducing Legendre polynomials as well as the addition theorem of spherical harmonic functions, Eq. (3.9) can be reformulated to Eq. (3.24). This procedure is well documented and can be found in numerous publications [cf. *(Rummel et al, 1988)*, *(Denker, 1988)*, *(Tsoulis, 1999)*, *(Kuhn and Seitz, 2010)*, *(Wild-Pfeiffer, 2007)*, *(Grombein et al, 2013)*, *(Rieser, 2015)* or *(Kuhn and Hirt, 2016)*].

The topographic potential coefficients, here denoted as $\bar{a}^e_{nm}$, are derived by introducing a constant crustal density ρ as

$$\bar{a}^e_{nm} = \frac{\rho}{M(2n+1)} \iiint_{\Omega} \left(\frac{r}{R}\right)^n \bar{Y}_{nm}(\lambda,\vartheta)\ d\Omega\ . \tag{3.27}$$

The infinitesimal volume element can be computed according to $d\Omega = r^2 d\sigma = r^2 sin\vartheta\ dr\ d\lambda\ d\vartheta$, when inserted in Eq. (3.27), it reads

$$\bar{a}^e_{nm} = \frac{\rho}{M(2n+1)} \frac{1}{R^n} \iint_{\sigma} \int_{r_l}^{r_u} r^n\ \bar{Y}_{nm}(\lambda,\vartheta)\ r^2 sin\vartheta\ dr\ d\lambda\ d\vartheta\ . \tag{3.28}$$

The integration in radial direction is now applied

$$\bar{a}^e_{nm} = \frac{\rho}{M(2n+1)} \frac{1}{R^n} \iint_{\sigma} \int_{r_l}^{r_u} r^{n+2}\ \bar{Y}_{nm}(\lambda,\vartheta)\ dr\ d\sigma\ , \tag{3.29}$$

and after insertion of the upper and lower integration boundaries, finally the topographic potential coefficients $\bar{a}^e_{nm}$ are obtained according to

$$\bar{a}^e_{nm} = \frac{\rho}{M(2n+1)(n+3)} \iint_{\sigma} \left(\frac{r_u^{n+3}}{R^n} - \frac{r_l^{n+3}}{R^n}\right) \bar{Y}_{nm}(\lambda,\vartheta)\ d\sigma\ . \tag{3.30}$$

The integration with respect to r is rigorously solved and is valid for the exterior potential. Following the aim of minimized linearization errors, r_u is determined as the orthometric height of the DTM, plus the geoid height based on a GGM and therefore an approximated ellipsoidal height is available (see also sec. 6.2.3). The lower integration boundary r_l is attributed to only the geoid height. Therefore, the origin of computation refers to a previously introduced global geoid solution. Additionally, the spherical harmonics $\bar{Y}_{nm}(\lambda,\vartheta)$ of the DTM integration points and the area elements $d\sigma$ of the DTM are known. For the solution of the radial integral kernel no binomial series e.g. *(Wild-Pfeiffer, 2007)* or condensed topography *(Kern et al, 2003)* is needed. Please note, that the constant crustal density $\rho = 2670\ kg/m^3$ can easily be replaced by, for example, a 2D surface density model. This provides individual density information for each mass column, in order to additionally help to improve the geoid *(Tziavos et al, 1996)*, which is described in more detail in sec. 4.4.

According to the topographic reduction, the complementary isostatic part may also developed into spherical harmonics. The isostatic potential coefficients can be found after the radial integration analogously to Eq. (3.30). In contrast to the topographic potential, a constant density contrast $\Delta\rho$ is used instead of the density ρ. This is due to the representation of the Airy-Heiskanen system, which is based on a condition of floating equilibrium. Furthermore, also the integration boundaries in the radial direction are different. For the upper boundary

r_u the normal thickness of the Earth's crust T = -30 km is introduced. The lower boundary r_l is provided by the corresponding root t according to

$$t = \frac{\rho}{\Delta\rho} H \ , \tag{3.31}$$

and for the ocean covered regions

$$t = \frac{\rho - \rho_w}{\Delta\rho} H \ . \tag{3.32}$$

In this case the lower integration boundary $r_l = T - t$ is scaled by the orthometric height above the geoid, whereas the relation between the two densities ρ and $\Delta\rho$ is assumed to be constant. For the ocean regions, $\rho_w = 1027\ kg/m^3$ is a common assumption. The model of isostatic compensation is presented in more detail in sec. 6.2.3. The impact of the isostasy on reduced gravity and the computed geoid is discussed in sec. 7.4.7.

3.3.2 Atmospheric Potential in Terms of Spherical Harmonics

The treatment of masses located above the gravity station is also important for a consistent geoid computation. Nevertheless, this effect is small compared to others, for example the topographic reduction, but needs to be considered. Analogously to the topographic reduction, the atmospheric potential is considered as a spherical harmonic representation by radial integration. Compared to the density of the topography ρ, the atmospheric density ρ^a is not a constant value for one single mass column, but depends on the actual height. Its value decreases with increasing height and a proper model for the potential representation has to be found. This research uses the ITSG atmospheric density model developed by *(Rieser, 2015)* to consider the masses above the measured gravity values. This model in turn is based on the US standard atmosphere model USSA76 *(NOAA et al, 1976)*.

ITSG Atmospheric Density Model

As an essential requirement, the radial or vertical integration of the atmospheric potential has to be performed in order to obtain a set of spherical harmonic coefficients for the exterior, as well well as for the interior space. Therefore, a layer approach according to the USSA76 was chosen where the parametrization is split into two different altitudes. According to *(Rieser, 2015)* for the density distribution it follows

$$\rho^a(h) = \begin{cases} \rho_0 \left(\frac{R}{R+h}\right)^{\nu} & 0 \leq h \leq 11\ km \ , \\ \rho^a(11\ km) \left(\frac{R+11\ km}{R+h}\right)^{\nu'} & 11\ km \leq h \leq Z \ . \end{cases} \tag{3.33}$$

In this case Z indicates the chosen maximum height. The coefficients $\nu = 680$ and $\nu' = 932$ respectively, are two degrees of freedom to perform a proper fit to the USSA76 model. The initial values are given with $\rho_0 = 1.225\ kg/m^3$ and $\rho^a\ (11\ km) = 0.3648\ kg/m^3$. The final outcome as stated by *(Rieser, 2015)* was that the residuals, compared to the USSA76, are small and the ITSG model fits quite well. This is very important for the lower altitudes up to 20 km, because most of the atmospheric masses are concentrated in this region. The atmospheric potential coefficients are derived by spherical harmonic expansion as described in the following. The atmospheric exterior potential coefficients are given as

$$\bar{a}_{nm}^{atm,e} = \frac{1}{M(2n+1)} \iint\limits_{\sigma} \int\limits_{r} \left(\frac{r}{R}\right)^n \rho^a(r)\ r^2\ \bar{Y}_{nm}\ dr\ d\sigma\ . \tag{3.34}$$

Introducing the atmospheric density $\rho^a(r)$, which in turn is a function of height, subsequently applying the radial integration, and additionally taking the difference between the ellipsoid and the sphere into account, the exterior atmospheric potential coefficients are found according to

$$\bar{a}_{nm}^{atm,e} = \begin{cases} \frac{\rho_0 R^3}{M(2n+1)(3+n-\nu)} \iint\limits_{\sigma} \bar{Y}_{nm} \left(\frac{\bar{R}}{R}\right)^{n+3} \times \\ \left[\left(1+\frac{Z}{\bar{R}}\right)^{n+3-\nu} - \left(1+\frac{h}{\bar{R}}\right)^{n+3-\nu}\right] d\sigma & \forall\ n \in \mathbb{N} \setminus (\nu-3) \\ \frac{\rho_0 R^3}{M(2n+1)} \iint\limits_{\sigma} \bar{Y}_{nm} \left(\frac{\bar{R}}{R}\right)^{n+3} \ln\left(\frac{\bar{R}+Z}{\bar{R}+h}\right) d\sigma & n = \nu - 3 \end{cases} \tag{3.35}$$

where $\bar{R}$ denotes the geocentric Earth radius. The treatment of the spherical harmonic degree $n = \nu - 3$ is special because of an occurring discontinuity, which is only attributed to the exterior potential. Fortunately, the treatment of the interior potential is much easier. The spherical harmonic coefficients are given as

$$\bar{a}_{nm}^{atm,i} = \frac{1}{M(2n+1)} \iint\limits_{\sigma} \int\limits_{r} \left(\frac{R}{r}\right)^{n+1} \rho^a(r)\ r^2\ \bar{Y}_{nm} dr\ d\sigma\ , \tag{3.36}$$

and again, after radial integration and rearrangements of the formulas, the atmospheric potential coefficients for the interior potential can be obtained by

$$\bar{a}_{nm}^{atm,i} = \frac{\rho_0 R^3}{M(2n+1)(2-n-\nu)} \iint\limits_{\sigma} \bar{Y}_{nm} \left(\frac{\bar{R}}{R}\right)^{2-n} \left[\left(1+\frac{Z}{\bar{R}}\right)^{2-n-\nu} - \left(1+\frac{h}{\bar{R}}\right)^{2-n-\nu}\right] d\sigma\ . \tag{3.37}$$

The distinction between interior and exterior potential depends on the location of the computation point P. If the solution of the Laplace equation is located inside ($r_P < R$), a sphere

with radius R, the corresponding solution is given according to Eq. (3.37). In case of $r_P > R$, the exterior potential according to Eq. (3.35) is valid.

In case of terrestrial gravity measurements the interior atmospheric potential is important because the attracting masses are located above the measurements. In contrast, if the geodetic measurements are taken at satellite altitudes of several hundred kilometers height, the atmospheric masses can be assumed to be underneath the measurement level, and therefore only the exterior potential is of further interest. Further details on this topic can be found in e.g. *(Rieser, 2015)*.

Typically, measured gravity datasets taken on the Earth's surface, are reduced by the atmospheric components following the International Association of Geodesy (IAG) approach. This approach accounts for the interior gravity effect in order to be conform with the Laplace assumption of mass-free exterior space *(Sjöberg, 1999)*. Additionally, the atmospheric masses are considered in the geopotential satellite models, as well as in the normal potential reference field. By reducing these effect from the measured gravity data and applying the atmospheric effect to the GGM, the gravity can be treated without atmosphere. Hence, the effect of atmospheric masses must be considered within the RCR procedure in order to ensure a consistent treatment. Results related to the atmospheric potential can be found in sec. 6.2.4 or sec. 6.4.3.

3.4 Potential and Linearization

In order to connect the non-linear relation of gravity field observables with the unknown geoid, some approximations of the Earth gravity field are required. To consider a linear relation between this quantities an approximation has to ensure only small deviations from the actual gravity field. Therefore, an ellipsoid of revolution with a corresponding normal potential is introduced as suitable counterpart of the Earth, which is briefly discussed in the following.

3.4.1 Normal Potential

The normal potential representation is based on the idea to split the Earth's gravity potential W into two parts. One normal part, with normal gravity and normal potential, which is related to a rotating ellipsoidal reference surface, and a small supplement. To ensure a similarity to the Earth's shape, a rotation ellipsoid can therefore be chosen with the benefit that the calculation can be carried out in a rigorous mathematically manner. In physical geodesy, a proper approximation of geometry and gravity of the Earth is required to perform a linearization between the geodetic observables and the Earth's gravity field which is in general a nonlinear relation. Therefore, a rotationally symmetric ellipsoid is used which does not deviate from the physical geoid by more than $\pm$ 100 m on a global scale.

According to *(Heiskanen and Moritz, 1967)* the normal potential can be written as

$$U = V_{ell} + \Phi \ , \tag{3.38}$$

where V_{ell} denotes the gravitational potential of the ellipsoid, and Φ is the centrifugal potential as described in sec. 3.4.2. The closed formulas, which are describing the normal potential or the ellipsoidal potential, can be found in e.g. *(Moritz, 1980a)*. For the exterior space, the spherical harmonic series notation of V_{ell} in a fully normalized form is again determined by Eq. (3.26). The magnitude of the normal gravity is given according to the Somiglianas formula

$$\gamma_0 = \frac{a\gamma_e \cos^2\varphi + b\gamma_p \sin^2\varphi}{\sqrt{a^2\cos^2\varphi + b^2\sin^2\varphi}} \ , \tag{3.39}$$

where γ_e, and γ_p respectively, denote the gravity at the equator and the poles. The major and semi-major axis of the ellipsoid are denoted with a and b. Due to the rotating symmetry of the ellipsoid, the normal gravity is only a function of the geodetic latitude. For details to the corresponding formulas, the reader is referred to *(Somigliana, 1929)* or *(Moritz, 1980a)*.

Somiglianas formula is only valid on the ellipsoidal surface. The gravity in an arbitrary ellipsoidal height h, can be approximated by a truncated series expansion according to

$$\gamma(h) = \gamma_0 \left[1 - \frac{2}{a}\left(1 + f + m - 2f\sin^2\varphi\right)h + \frac{3}{a^2}h^2\right] \ , \tag{3.40}$$

with the ellipsoidal flattening,

$$f = \frac{a-b}{a} \ . \tag{3.41}$$

The chosen reference ellipsoid is responsible for the quality of the geoid approximation. A common approach is to use the GRS80 ellipsoid, according to *(Moritz, 1980b)*, as a reference field. In general, the normal gravity vector can be computed with the gradient operator applied to the corresponding potential $\boldsymbol{\gamma} = \nabla U$.

This thesis is chasing a different approach, where the normal gravity is replaced by the gravity derived from a GGM. Also, the shape is approximated by a geoid model instead of the ellipsoid. In this case, a more realistic Taylor point can be obtained and therefore the linearization errors are minimized. The impact of this approach is presented in sec. 7.4.1.

3.4.2 Centrifugal Potential

The centrifugal potential Φ is part of the relation between the Earth's gravity potential W and the normal potential U. A simple analytical representation in terms of Cartesian coordinates is given by

$$\Phi = \frac{1}{2}\omega^2 \left(x^2 + y^2\right) \ , \tag{3.42}$$

where ω denotes the angular velocity of the Earth's rotation. Analogous to the gravity potential and the normal potential, the components of the centrifugal potential can be derived by the first derivative of the potential according to

$$\nabla\Phi = \begin{pmatrix} \frac{\partial\Phi}{\partial x} \\ \frac{\partial\Phi}{\partial y} \\ \frac{\partial\Phi}{\partial z} \end{pmatrix} \ . \tag{3.43}$$

If the Laplace operator is applied to the centrifugal potential

$$\Delta\Phi = \frac{\partial^2\Phi}{\partial x^2} + \frac{\partial^2\Phi}{\partial y^2} + \frac{\partial^2\Phi}{\partial z^2} = 2\omega^2 \ , \tag{3.44}$$

it reveals that Φ is not harmonic. The centrifugal acceleration depends on the distance to the Earth's rotational axis and acts in the opposite direction to the gravitational acceleration. Therefore, the centrifugal acceleration becomes stronger towards the equator *(Moritz, 1980a)*.

3.4.3 Disturbing Potential

The relation between the gravity potential of the Earth W and the normal potential U, which is usually used as reference potential, is affected by a small difference because the reference ellipsoid is only an approximation of the geoid and the real gravity field. The potential difference is referred to as disturbing potential T. Assuming that the geoid and the reference ellipsoid are very similar, the following relation is valid

$$W = U + T \ . \tag{3.45}$$

The disturbing potential satisfies the Laplace equation outside the attracting masses and $\Delta T = 0$ is valid. It is basically defined as the difference between the actual and the assumed potential. A proper approximation of the actual field leads to a small residual part and enables the opportunity for a truncated Taylor series expansion. The disturbing potential can therefore be expressed as

$$T = W - U = V - V_{ell} \ . \tag{3.46}$$

A representation in terms of spherical harmonics is possible and due to the cancellation of the centrifugal potential, finally the series reads

$$T(r, \vartheta, \lambda) = \frac{GM}{R} \sum_{n=0}^{\infty} \left(\frac{R}{r} \right)^{n+1} \sum_{m=-n}^{n} \Delta \bar{a}_{nm} \bar{Y}_{nm}(\vartheta, \lambda) \ . \tag{3.47}$$

The coefficients $\Delta \bar{a}_{nm}$ represent the linearized difference of the two fully normalized potentials in the spectral domain. The derivatives of the disturbing potential are also important and provide a connection of the individual gravity field quantity to the disturbing potential which can in turn expressed in spherical harmonics.

For the linearization a common way is to use the normal potential and the normal field for a first order approximation with its realization by the GRS80 ellipsoid shape and gravity *(Moritz, 1980b)*. This assumption, in combination with a spherical approximation of the Earth in mathematical calculation and physical geodesy, leads to a global geoid rms value of approximately ± 30 m, whereas the minimal and maximal deviations are of about ± 100 m. Therefore, in case of spherical approximation an error of about 0.3 % of the Earth flattening propagates in a geoid error of about ± 10 cm *(Moritz, 1980a)*, which is not the desired geoid quality nowadays.

Due to a steady progress in the processing and quality of GGMs during recent decades, it is more appropriate to use the shape and gravity from up to date GGM models. Investigations and different validation of geoid heights, derived from this gravity models with independent GPS/leveling observations, show a long wavelength agreement and a global rms of approximately ± 0.3 m [see e.g. *(Gruber and Köhl, 2008)* or *(Gruber et al, 2011)*].

Assuming the spherical approximation is used for GGM derived shape and gravity, this would lead to an improved first order approximation because of the improved long wavelength agreement. The remaining geoid rms is now expected to be on the millimeter level. The replacement of the normal field by a GGM and the occurring effect is discussed in more detail in sec. 7.4.1.

3.5 Functionals of the Disturbing Potential

3.5.1 Gravity Anomalies

Gravity anomalies are usually defined as the vector difference between a point P_0 located on the geoid and a point Q which is located on a reference ellipsoid, as illustrated in Fig. 3.1. In this original definition, based on a normal field ellipsoid the corresponding normal gravity vector $\boldsymbol{\gamma}$ is introduced as Taylor point for the linearization. In vector notation gravity anomalies are defined as

$$\Delta \boldsymbol{g} = \boldsymbol{g}_P - \boldsymbol{\gamma}_Q \ . \tag{3.48}$$

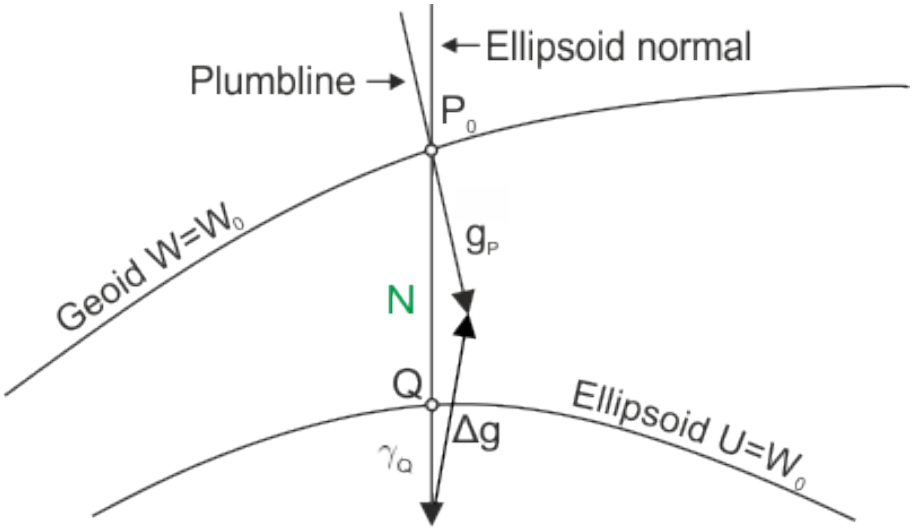

Figure 3.1: Common definition of gravity anomalies

It is also important to know that the difference of the directions of both gravity vectors $\boldsymbol{g}_P$ and $\boldsymbol{\gamma}_Q$ respectively, evaluated at the same point located on the Earth's surface, leads to deflections of the vertical (see Fig. 3.3). In turn this is connected to the definition of the gravity disturbance as discussed in sec. 3.5.2. Several results and validations concerning the deflection based astrogeodetic geoid computation can be found in sec. 7.2.2. However, gravity anomalies represent the basic input for gravimetric geoid determination. Due to the fact that there is a huge amount of gravity observations available, as will be discussed in sec. 4.2, a combined geoid solution which includes deflections of the vertical, heavily depends on gravity anomalies. This is shown in sec. 7.2.3.

Gravity anomalies can be represented by the fundamental equation of physical geodesy in spherical approximation. According to *(Hofmann-Wellenhof and Moritz, 2006, p.97)* it follows

$$\Delta g = -\frac{\partial T}{\partial r} - \frac{2}{r} T \ , \tag{3.49}$$

which allows the introduction of the disturbing potential in terms of spherical harmonics. Inserting Eq. (3.47) into Eq. (3.49) finally gives

$$\Delta g = \frac{GM}{R^2} \sum_{n=0}^{\infty} (n-1) \left(\frac{R}{r}\right)^{n+2} \sum_{m=-n}^{n} \left[\Delta \bar{c}_{nm} \cos m\lambda + \Delta \bar{s}_{nm} \sin m\lambda\right] \bar{P}_{nm} \ . \tag{3.50}$$

An alternative approach is to introduce an approximated geoid solution instead of the ellipsoid, to obtain a more realistic Taylor point for the linearization. This in turn leads to a different definition of gravity anomalies, because the reference surface changes and is now related to the a-priori geoid. The gravity anomaly vector related to the geoid, which is based on a GGM, is given according to

$$\Delta \boldsymbol{g} = \boldsymbol{g}_P - \boldsymbol{g}_{GGM} \ . \tag{3.51}$$

This alternative definition is illustrated in Fig. 3.2 and is used for this thesis.

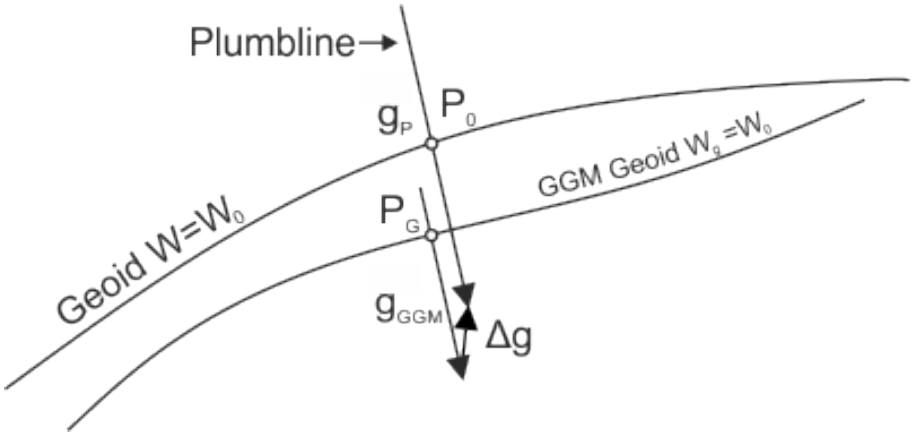

Figure 3.2: Alternative definition of gravity anomalies

3.5.2 Gravity Disturbances

In order to obtain the fundamental equation of physical geodesy a second quantity of the disturbing potential, namely the gravity disturbance, is required. The original definition of the gravity disturbance vector is given by comparing the gravity vector $\boldsymbol{g}$ and the normal gravity vector $\boldsymbol{\gamma}$ at the same point P. This can be done easily because vectors can be shifted in their line of action. The difference in magnitude between the actual and the normal gravity vector reads

$$\delta \boldsymbol{g} = \nabla T = \boldsymbol{g}_P - \boldsymbol{\gamma}_P \ , \tag{3.52}$$

and generally, this corresponds to the gradient of the disturbing potential T. The scalar valued gravity disturbance reads

$$\delta g = -\frac{\partial T}{\partial r} \ , \tag{3.53}$$

which gives the gravity disturbance and its connection to the disturbing potential *(Hofmann-Wellenhof and Moritz, 2006, p.94)*. The radial derivative of the disturbing potential which is given in Eq. (3.47) provides the gravity disturbance expressed in terms of spherical harmonics

$$T_r = \delta g = -\frac{GM}{R^2} \sum_{n=0}^{\infty} (n+1) \left(\frac{R}{r}\right)^{n+2} \sum_{m=-n}^{n} \left[\Delta \bar{c}_{nm} \cos m\lambda + \Delta \bar{s}_{nm} \sin m\lambda\right] \bar{P}_{nm} \ , \tag{3.54}$$

The gravity disturbance plays a major role in the topographic reduction, if the reduction follows the linearized approach and the reduction steps are carried out subsequently as described in sec. 7.4.1. The common definition of the gravity disturbance is shown in Fig. 3.3. If the evaluation is related to the same point P located on the Earth's surface and applying a projection into a local horizontal system, deflections of the vertical can be decomposed from it (see sec. 3.5.3). The radial component represents the difference in terms of magnitude.

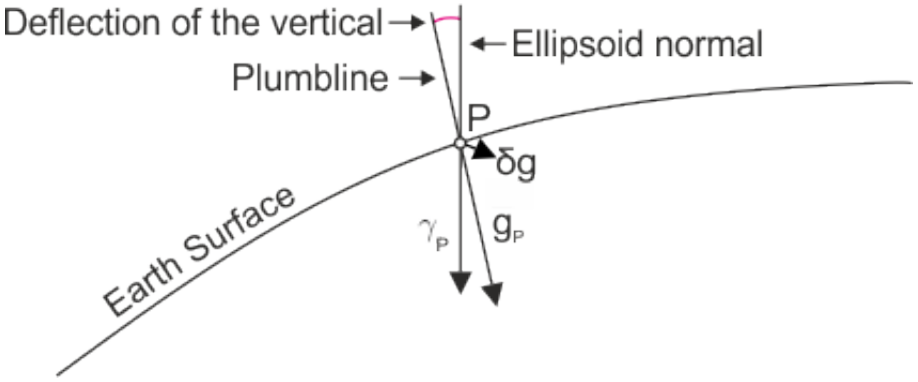

Figure 3.3: Common definition of the gravity disturbance

3.5.3 Deflections of the Vertical

Generally, deflections of the vertical are defined as the difference of the astronomical coordinates Φ and Λ which are connected to the actual plumb line, and the geodetic coordinates φ and λ which are related to the ellipsoid normal. Depending on the direction of the deflections, one may distinguish between a North-South, and an East-West component.

The North-South component ξ is conventionally defined as the coordinate difference

$$\xi = \varphi - \Phi \ , \tag{3.55}$$

whereas the East-West component η is given as

$$\eta = (\Lambda - \lambda)\cos\varphi \ . \tag{3.56}$$

The computation of deflections of the vertical from the disturbing potential can be achieved according to *(Hofmann-Wellenhof and Moritz, 2006, p.370)*. Depending on the chosen coordinate system it follows

$$\xi = -\frac{1}{\gamma r}\frac{\partial T}{\partial \varphi} \ , \quad \text{or} \quad \xi = \frac{1}{\gamma r}\frac{\partial T}{\partial \vartheta} \ , \tag{3.57}$$

and the East-West component, respectively

$$\eta = -\frac{1}{\gamma r \cos\varphi}\frac{\partial T}{\partial \lambda} \ , \quad \text{or} \quad \eta = -\frac{1}{\gamma r \sin\vartheta}\frac{\partial T}{\partial \lambda} \ . \tag{3.58}$$

In case of deflections of the vertical, the direction of the gravity vector is the important quantity. The link between gravity, or more specifically the gravity disturbance vector and deflections is given by subtracting the normal gravity vector from the gravity vector if the two vectors refer to the same point P. According to *(Hofmann-Wellenhof and Moritz, 2006, p.246)* the following relation is valid

$$\delta \boldsymbol{g} = \boldsymbol{g}_P - \boldsymbol{\gamma}_P \approx \begin{pmatrix} -\gamma\xi \\ -\gamma\eta \\ -\delta g \end{pmatrix} \ . \tag{3.59}$$

Due to spherical approximation the deflections can be directly obtained from Eq. (3.59) by only taking the horizontal components of the gravity disturbance vector into account. It follows

$$\xi = -\frac{1}{\gamma}\delta g_{\varphi} \ , \quad \text{and} \quad \eta = -\frac{1}{\gamma}\delta g_{\lambda} \ . \tag{3.60}$$

Furthermore, if the normalized gravity vector is evaluated in a local level coordinate system which corresponds to North, East and Up coordinates as defined in *(Hofmann-Wellenhof and Moritz, 2006, p.209)*, the deflections are derived from the two horizontal components of the local ellipsoidal system vector without linearization. All results achieved in sec. 7.1.2 and sec. 7.5 are based on this approach. A solely astrogeodetic geoid solution based on measured deflections of the vertical and a dense map of estimated deflections derived from gravity data are shown in the result chapter. A quality statement and validation issues are also presented therein

Performing the partial derivative of the disturbing potential, Eq. (3.47), leads to

$$T_{\vartheta} = \frac{GM}{R}\sum_{n=0}^{\infty}\left(\frac{R}{r}\right)^{n+1}\sum_{m=-n}^{n}\left[\Delta\bar{c}_{nm}\cos m\lambda + \Delta\bar{s}_{nm}\sin m\lambda\right]\frac{d\bar{P}_{nm}}{d\vartheta} \ , \tag{3.61}$$

$$T_{\lambda} = \frac{GM}{R}\sum_{n=0}^{\infty}\left(\frac{R}{r}\right)^{n+1}\sum_{m=-n}^{n} m\left[\Delta\bar{c}_{nm}\sin m\lambda - \Delta\bar{s}_{nm}\cos m\lambda\right]\bar{P}_{nm} \ , \tag{3.62}$$

which can now be used to compute the deflection components according to Eq. (3.57) and Eq. (3.58) in spherical harmonic representation.

3.5.4 Geoid Heights

The link between the disturbing potential and the geoid height is defined by Bruns equation *(Bruns, 1878)*

$$N = \frac{T}{\gamma} \ . \tag{3.63}$$

This equation is used to calculate the geoid if the disturbing potential is evaluated on the geoid surface. Inserting Eq. (3.47) into Eq. (3.63), the geoid in terms of spherical harmonics may be computed according to

$$N = \frac{GM}{R\gamma}\sum_{n=0}^{\infty}\left(\frac{R}{r}\right)^{n+1}\sum_{m=-n}^{n}\left[\Delta\bar{c}_{nm}\cos m\lambda + \Delta\bar{s}_{nm}\sin m\lambda\right]\bar{P}_{nm} \ . \tag{3.64}$$

4 Database for Austrian Geoid Determination

For the issue of geoid determination, a historical review on the Austrian geoid is provided. During recent decades different types of data, for example, gravity measurements, deflections of the vertical or GPS/leveling measurements have been collected by the Federal Office of Metrology and Surveying (BEV) and are available for this thesis. Austria is an interesting area for the purpose of gravity field modeling because of its manifold topography. On the one hand it consists of flatland with heights of approximately 200 m above sea level and on the other hand there are alpine areas with an elevation of 3800 m. The topography is covered by a high resolution Digital Terrain Model (DTM).

4.1 History of the Austrian Geoid

Returning to the beginnings of the Austrian geoid computation in the early 50s of the last century, *Josef Litschauer* provides a first astrogeodetic geoid solution based on only a few deflections of the vertical, which were located on geodetic triangulation points *(Litschauer, 1953)*. Furthermore, *Karl Rinner* and *Helmut Moritz* played a key role in Austrian gravity field determination. *Helmut Moritz* is one of the most recognized representatives in the field of physical geodesy. His publications have for a long time been considered as the standard literature in this field of research. The Least Squares Collocation (LSC) method provides one possible tool for combining heterogeneous datasets. Based on this approach, further geoid solutions were calculated by *Hans Sünkel* and *Norbert Kühtreiber*. Under the lead of *Hans Sünkel*, who is a pioneer in Austrian gravity field determination, much work has been carried out at Graz University of Technology since the 1980s. He published his astrogeodetic geoid solution in 1987 *(Sünkel et al, 1987)*. *Norbert Kühtreiber* calculated a pure gravimetric geoid solution in 1998 *(Kühtreiber, 1998b)* and also the first combined solution, which was based on gravity measurements and deflections of the vertical *(Kühtreiber, 2002)*.

In the year 2007 *Roland Pail* established the new official Austrian geoid *(Pail et al, 2008)*. This solution is currently still the national geoid provided by the BEV. A combination of heterogeneous data by the LSC method was applied in order to improve the Austrian geoid to the accuracy level of a few centimeters. Nevertheless, this solution is still affected by systematic errors between GPS/leveling measurements and the gravimetric geoid. The use of a non-physical correction surface could not be avoided. More details on the national geoid can be found in sec. 4.1.1.

Further historical information about the beginnings of the Austrian geoid computation is presented in *(Rinner, 1983)*. It should be mentioned that all geoid determination approaches,

as well as the official geoid solution, are based on the LSC method. In this thesis an alternative approach by a Gauss-Markov model in combination with Radial Basis Functions (RBF) is applied (see chap. 6).

4.1.1 Project GEOnAUT

The Austrian Geoid 2007 - GEOnAUT project, was the first in a series funded by the Austrian Research Promotion Agency (FFG). Under the lead of the Institute of Navigation and Satellite Geodesy (INAS) and in cooperation with project partners, namely the BEV and the Institute of Numerical Mathematics (INM), it was successfully carried out during the years 2006-2007. The BEV contributed as data provider, consultant and external evaluator of the results.

The main goal of the project was to compute a new geoid solution by combining all available data at that time. To ensure an optimal LSC result, the gravity data was thinned to approximately 4×4 km spatial resolution to avoid partly clustered observation sets, which can lead to a numerically unstable equation system for the LSC method. This approach has the drawback that not all available data can be used due to computational reasons. An overview about the different datasets used and their spatial distribution is illustrated in Fig. 4.1.

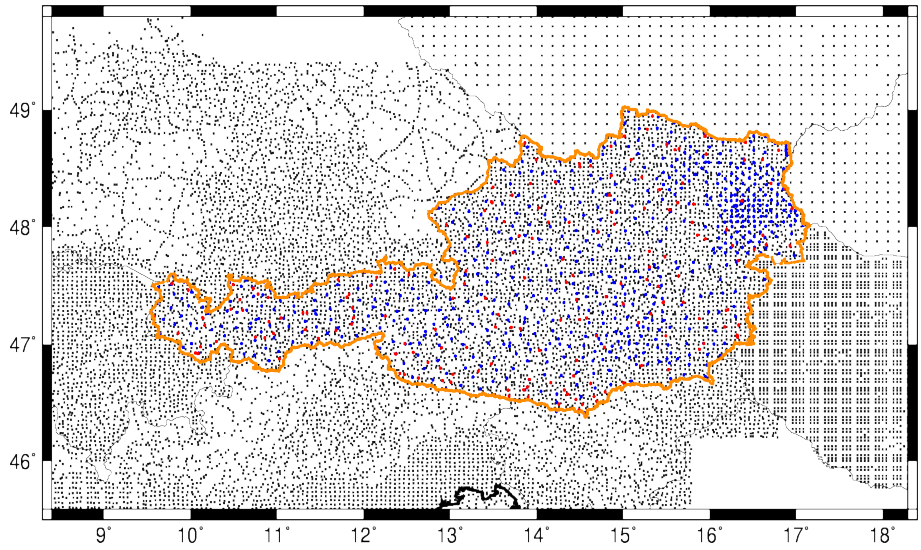

Figure 4.1: GEOnAUT data: gravity measurements (black), deflections of the vertical (blue) and GPS/leveling observations (red)

In particular, the dataset consists of:

- 14001 measured gravity
- 672 deflections of the vertical
- 170 GPS/leveling observations

The terrain model used is originally based on the work of *(Graf, 1996)* but includes minor updates, for example, new DTM information for Switzerland (see also sec. 4.3). The long

wavelength part of the gravity field was represented by the satellite-only EIGEN-GL04S1 model *(Förste et al, 2006)* up to d/o 70. The short wavelength part was determined by using the classic approach of Airy-Heiskanen topographic/isostatic compensation (see sec. 6.2.3). Further information on the GEOnAUT project can be found in *(Pail et al, 2007)*. The outcome of this project represents the present national geoid solution.

The geoid solution was driven by a practical approach to overcome inconsistencies in the geoid modeling and therefore a correction surface was applied. An illustration of the Austrian geoid based on the LSC approach is given in Fig. 4.2. This solution is not independent of GPS/leveling observations, which makes it difficult to provide reliable accuracy information. However, the geoid was re-evaluated based on 700 independent GPS/leveling observations available only in the Western part of Austria and the BEV specifies an overall geoid accuracy < 3 cm. Further validation results can be found in *(Pail et al, 2009)*.

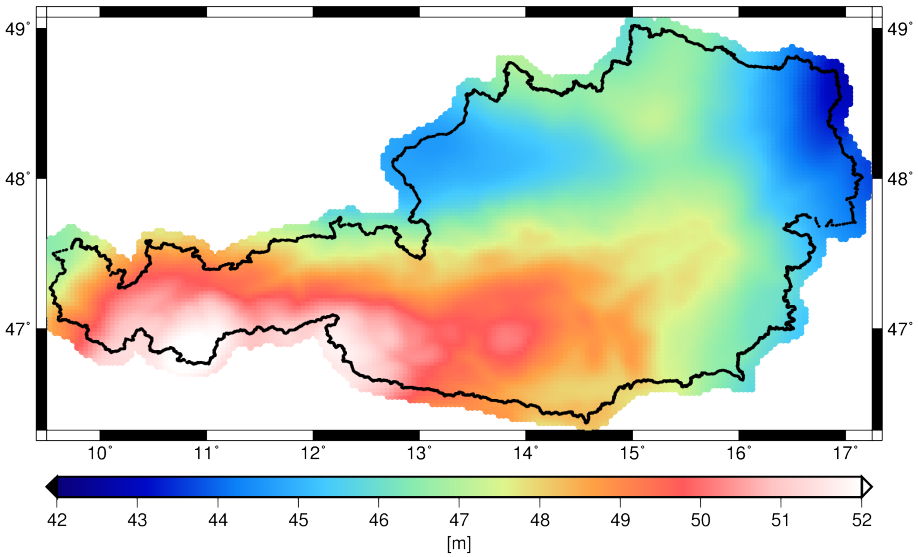

Figure 4.2: Official Austrian geoid solution based on the GEOnAUT project

The Austrian Geoid 2007

The framework for the geoid determination has been provided by the Remove-Compute-Restore (RCR) procedure and combination of different data types. Within this procedure the LSC method was utilized for the computation of the residual geoid. After some quality checks and a data preparation step (see sec. 4.2), the final gravity dataset of 14001 gravity measurements, with a spatial distance of about 4×4 km, was established. The spatial distribution was a requirement for the LSC procedure, in order to avoid computational problems. As a second gravity field quantity, 672 deflections of the vertical were available, representing a different kind of gravity field observation. Furthermore, 170 GPS/leveling observations were incorporated in the geoid estimation process to constrain the solution.

The Global Gravity field Model (GGM) EIGEN-GL04S1 *(Förste et al, 2006)* up to d/o 70 has been used to represent the long wavelength part of the gravity field. The short wavelength part was considered with the topographic/isostatic compensation according to Airy-Heiskanen with a constant standard crustal density of 2670 kg/m^3 for the topography and a constant density contrast of 600 kg/m^3 for the isostasy. A high resolution DTM (see sec. 4.3) was used to represent the topography in the vicinity of the observations ($<$ 15 km). Beyond a 15 km radius, until the Hayford zone radius of $<$ 167 km, a more generalized DTM was used to model the gravitational attraction. Distant topographic masses beyond a distance of 167 km were not considered. More details can be found in *(Pail et al, 2008)*.

With the chosen processing strategy, inconsistencies between a purely gravimetric geoid and GPS/leveling observation in the range of several meters could not be avoided. At that time, the reason for this trend field was supposed to be in a systematic inconsistent orthometric height system or remaining GPS height errors. To overcome these inconsistencies and to cope with the systematic effect, a non-physical correction surface was introduced. A practical way to handle these inconsistencies is to fit a polynomial surface to the differences, which is applied twice within the RCR procedure. In an initial step, the correction surface is reduced from the GPS/leveling observations within the remove step. In a second step, it has been restored to the estimated residual geoid (from LSC) during the restore step. The physical meaning of the geoid as an equipotential surface is lost, but the geoid solution fits very well to the GPS/leveling observations and therefore an improved geoid accuracy can be expected. This approach followed the requirements by the BEV, in order to use the geoid as a transformation surface from GPS heights to orthometric heights and vice versa. In Fig. 4.3 the correction surface which has been applied to the Austrian geoid 2007 is shown.

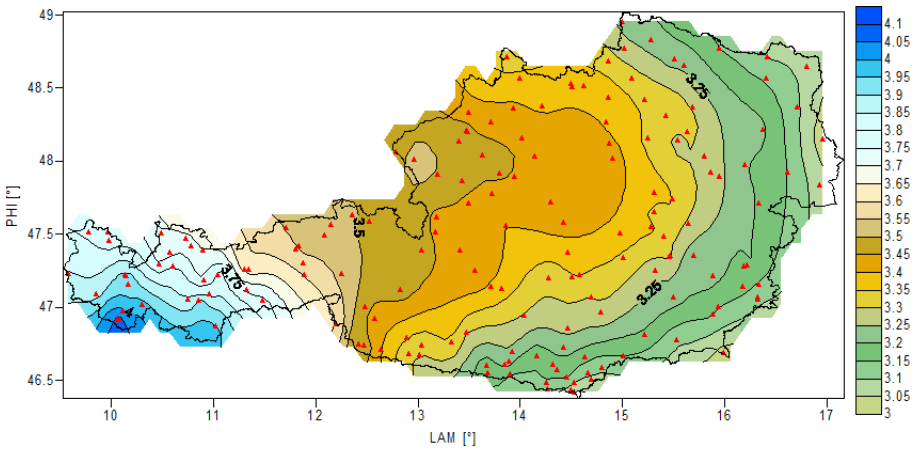

Figure 4.3: Correction surface given on a approximately 3×3 km grid used for the official Austrian geoid solution 2007 [m]; The positions of the 170 GPS/leveling observations are indicated in red *(Pock, 2011)*

In case of the Austrian geoid 2007, this surface was represented by a third degree polynomial. As can be clearly seen in Fig. 4.3, the correction surface, which is originally based on 170 GPS/leveling observations and their deviations to a gravimetric geoid, is in a range of several meters including bias and trend. Furthermore, investigations have shown that the correction

surface strongly depends on the chosen d/o of the GGM, leading to a long wavelength behavior with increasing degree and order [see *(Pock, 2011)*].

The relative weighting issue between different gravity field quantities was also part of investigations. In case of GPS/leveling, the weighting was applied as an iterative process in order to fit the geoid to these observations. In a first step, and in order to keep the residuals between predicted and observed geoid heights small, the GPS/leveling observations are assigned with an a-priori weight of 1 mm each *(Pail et al, 2008)*. This leads to residuals of only few millimeters. In a second step, these residuals in turn were introduced as individual a-priori weights and a geoid recalculation was carried out to compute the final official solution. The gravity anomalies were assumed to be known, with an a-priori accuracy of 1 mgal. For deflections of the vertical a sigma of the ξ and η components of 0.30" was assumed. For both aspects, an empirical approach was used to determine the a-priori weights. Due to a polynomial representation of the introduced correction surface, the accuracy of the computed geoid was specified by the BEV with < 3 cm. Further validation results and a LSC error estimate of the Austrian geoid can be found in *(Pail et al, 2009)*.

Since this practical approach of geoid determination was applied, the Austrian geoid 2007 heavily depends on GPS/leveling observations. This can cause problems especially if these observations are re-evaluated over the years. Indeed, this was undertaken in the follow-on GEOID+ project (see sec. 4.1.2) with the result that for many observations the geoid height has changed by some centimeters. Therefore, the geoid solution also needs to be recomputed in order to ensure consistency. Nevertheless, the BEV did not make use of the geoid update in the GEOID+ project as official solution, which leads to inconsistencies between the present national geoid and GPS/leveling observations (see also sec. 4.2.3).

4.1.2 Project GEOID+

The follow-on project to GEOnAUT was called GEOID+. This project was again funded by the FFG and the GEOnAUT research group constellation have teamed up again to improve the Austrian geoid during the years 2009-2010. In principle, the input datasets which are based on the previous project, remain the same, with the exception of minor DTM changes and some updates attributed to the gravity data thinning process. This also holds true for the LSC geoid computation method, as well as the RCR procedure. The only considerable difference is attributed to an updated GPS/leveling dataset and additional gravity data observations from Slovenia. The entire dataset for this project is illustrated in Fig. 4.4.

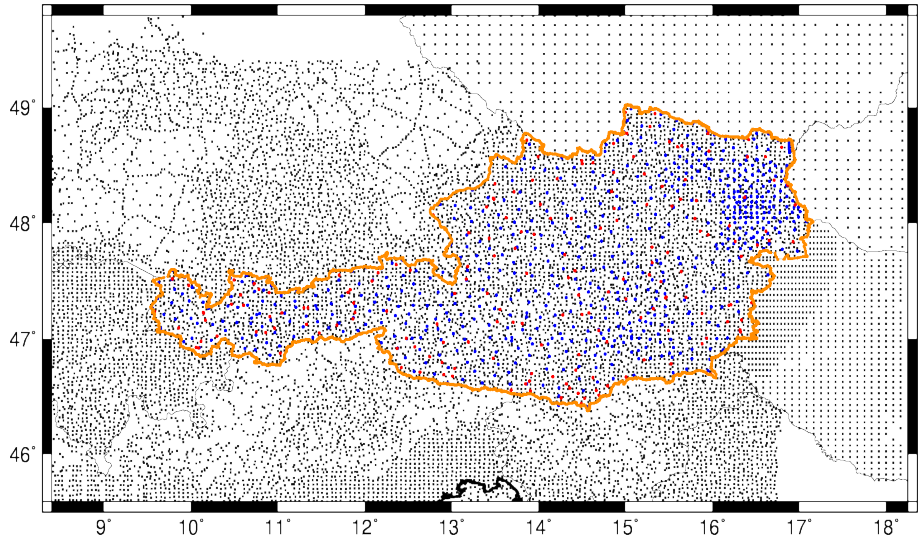

Figure 4.4: GEOID+ dataset: gravity measurements (black), deflections of the vertical (blue) and GPS/leveling observations (red)

In particular, the input dataset consists of:

- 13689 measured gravity
- 672 deflections of the vertical
- 192 GPS/leveling observations

Due to a new thinning process, the gravity input data are slightly different in comparison to the GEOnAUT project. The reason for this was connected to some problems with the gridded Hungarian data, which were now eliminated. In addition, the DTM has been improved by newly acquired data from Slovenia and South-Tyrol. In this project the first GGM incorporating GOCE data, the GOCO01s *(Pail et al, 2010)*, was available to represent the long wavelength part of the gravity field. Although some new datasets are included a correction surface was still required. Therefore, the BEV decided against a new geoid solution because the final improvements between the official geoid and the GEOID+ project did not justify this from their point of view. In contrast, a complete re-evaluation of GPS/leveling observations was carried out in the GEOID+ project. This in turn means that the official Austrian geoid derived from the GEOnAUT project is inconsistent compared to the updated set of GPS/leveling observations, because the height changes are significant (see sec. 4.2.3) and a corresponding new geoid solution, which is again fitted to these re-evaluated observations, has not replaced the official Austrian geoid. Further details related to GEOID+ can be found in *(Kühtreiber et al, 2011)*.

4.1.3 Project GARFIELD

The Geoid for Austria - Regional gravity FIELD improved (GARFIELD) project was launched in 2012 and officially ends at the beginning of 2016. It was funded by the Austrian Sciences Fund (FWF). The research group consists of the former Institute of Theoretical Geodesy and Satellite Geodesy (ITSG), under the lead of *Torsten Mayer-Gürr*, in cooperation with the INAS institute and the BEV.

The main goal was to derive a high quality regional gravity field solution for Austria with unprecedented accuracy. The gravity field determination should be based on an optimum combination of satellite observations and all complementary available terrestrial gravity field data. Another important aspect was to incorporate the final GOCE mission results and the latest satellite-only GGM. Further methodological developments were also important tasks of this project. This includes an adapted RCR procedure, as well as comparisons between the LSC method and an alternative parametrization based on RBF. The combination of heterogeneous data types additionally required a careful determination of weighting among different a-priori defined observation groups. This was achieved by utilizing the Variance Component Estimation (VCE) method. Main results of the project are derived from this thesis. The entire terrestrial dataset is shown in Fig. 4.5.

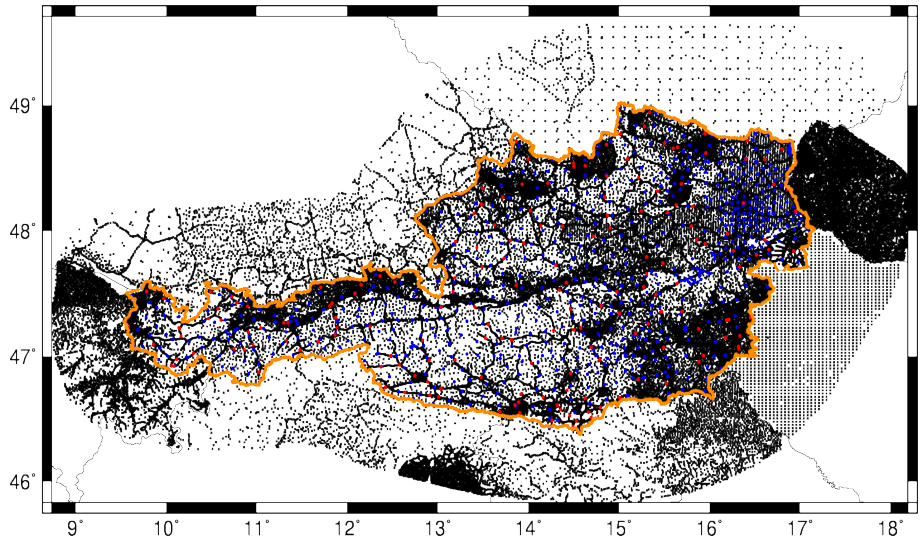

Figure 4.5: GARFIELD data: gravity measurements (black), deflections of the vertical (blue) and GPS/leveling observations (red)

In particular, the input dataset consists of:

- 72327 measured gravity
- 735 deflections of the vertical
- 192 GPS/leveling observations

The GPS/leveling observations remain the same as in the GEOID+ project. The number of deflections of the vertical could be increased, due to some additional measurements connected

to the Koralm and Semmering tunnel projects, measured with a digital astronomical measurement system *(Bürki et al, 2004)*. In addition, some real gravity measurements in Slovakia and the Czech Republic are now available. Previously only interpolated gravity data was available in those regions.

The entire gravity dataset is used and a down-sampling of the data, as it is required for the LSC method, is no longer a requirement and therefore the amount of input data increases. A new computation method using a Gauss-Markov model with RBF parametrization is applied (see sec. 6.3.1). The availability of the latest GOCO product, the satellite-only gravity field model GOCO05s *(Mayer-Gürr et al, 2015)*, (see sec. 6.2.2) also contributes to the success of the project. Improvements in the scope of the RCR technique, in order to avoid a double consideration of the topographic masses, are described in chapter 6. Furthermore, the topic of atmospheric effects is new in Austrian geoid computation.

4.2 Available Gravity Field Quantities for Geoid Computation

In this section a short overview of the most important gravity field quantities for geoid computation is provided. This includes a historical review as well as actual remarks on the datasets.

4.2.1 Gravity Database

The entire gravity database of Graz University of Technology and the BEV includes almost 132000 measurements. About 50000 of these are located within the Austrian territory. All gravity values are connected to the official Austrian gravity network (ÖSGN), [see *(Ruess, 1983)*] which consists of approximately 800 datum points and is further linked to 35 absolute gravity measurements. This gives the zero order net of Austria. The remaining gravity observations are based on relative measurements, connected to 1-3 order nets. During recent decades, a vast amount of gravity values were collected by *Norbert Kühtreiber*. The BEV is the owner of the entire dataset and distributes them on request.

The Austrian gravity dataset has been collected during the past 70 years and consists of data from several contributors. In particular, they are

- BEV, Austria
- Institute of Meteorology and Geophysics, University of Vienna, Austria
- Institute of Geophysics, Mining University of Leoben, Austria
- Institute of Geophysics, Technical University of Clausthal, Germany
- Institute of Geophysics, Technical University of Vienna, Austria
- OMV AG, Austria

In the 1950s the first gravity measurements were carried out along the spirit leveling lines using relative gravimeter. Today modern equipment is available as shown in Fig. 4.6a. The zero

order net values for the ÖSGN are measured with free fall absolute gravimeter, as illustrated in Fig. 4.6b. The absolute values of the gravity acceleration within Austria are approximately between 9.80 and 9.81 m/s^2 and can be seen in Fig. 4.7.

(a) Relative gravimeter (b) Absolute gravimeter

Figure 4.6: (a) Relative gravimeter LCR; (b) Absolute gravimeter FG-5

Since the end of the 1980s, high-precise absolute gravity measurements have been regularly performed by the BEV using the JILAg-6 instrument, which was able to measure the Earth's gravity acceleration with a standard deviation of ± 8 μgal[1] *(Ruess and Ulrich, 2011)*. Since 2010 the BEV commissioned a new, more accurate measurement system (FG-5). Currently there is work in progress to densify the net of absolute gravity measurements within Austria.

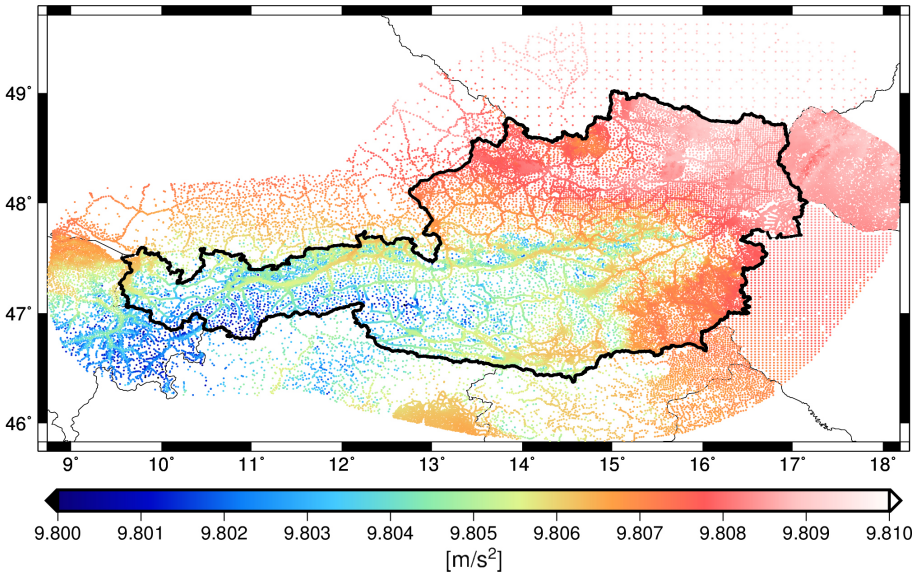

Figure 4.7: Gravity accelerations

[1] $1\mu gal = 10nm/s^2$

The relative gravity measurements were mostly performed with LaCoste Romberg (LCR) and Scintrex CG-3 instruments between 1980-2010. Since 2010 the new Scintrex CG-5 has been used to ensure an accurate constraint to the absolute gravimeter measurements. Additional measurements in the period between 1950-1980 provided by oil and gas companies, using the Worden 500 gravimeter, or data collected by other Universities, by means of the Noorgard gravimeter, completed the Austrian gravity database.

The motivation for the first gravity measurement campaign was to establish a height system for Austria. These old measurements were different in their offset behavior and calibration accuracy. During recent decades different measurements are combined and re-calibrated, which results in a unified Austrian gravity frame. This work has mostly been undertaken by *Diethard Ruess* from the BEV. Further information can be found in *(Ruess, 2001)*. Regarding the data from the neighbouring countries, a unified system can not be guaranteed. Nevertheless, in the boundary region between Austria and its neighbors a continuing similar behavior of the reduced cross-border gravity values can be observed. This is an indicator for a reasonable homogeneous gravity input, throughout the entire set of observations. Further details about the beginnings of the ÖSGN can be found in *(Ruess, 1995)*.

The accuracy information for the gravity data are provided by the BEV and is shown in Tab. 4.1 [see *(BEV, 2007)*. It describes the quality of the entire dataset, depending on the measurement system used. Due to different measurement epochs during the last decades, the specified quality only represents the reliability of the measurements not the overall accuracy of the measurement systems. Interpolated or estimated gravity data, as well as data with an uncertainty threshold > 0.40 mgal, are not considered for the geoid computation.

Table 4.1: Quality of Austrian gravity data *(BEV, 2007)*

Instrument	σ **[mgal]**	**Type**	**Number**
FG5 and JILAg-6	< 0.005	absolute	35
LCR-D	< 0.02	relative	11507
LCR-G	< 0.02	relative	15237
LCR-general	< 0.02	relative	9384
Scintrex CG-3	< 0.02	relative	422
Worden 500	< 0.07	relative	8939
Norgaard	< 0.30	relative	3816

Preprocessing of Gravity Data - Quality Check

In an initial step the quality of the input data has been evaluated by means of using the values of Tab. 4.1. Interpolated or estimated data has been rejected beforehand. Additionally, the associated height of the gravity measurements provided by BEV was subject of a quality check. Hence, only gravity measurements with a height uncertainty < 2 m, which corresponds to a gravity error of about 0.60 mgal have been taken into account. Moreover, a vast majority of gravity data is specified with a height uncertainty of < 0.1 m *(BEV, 2007)*. Another criterion is

the deviation between the terrain model and the gravity station height. For the high resolution DTM BEV00 (see sec. 4.3.1), the height differences are shown in Fig. 4.8. Here the nearest DTM point was chosen to calculate the deviation. For the gravity positional information no quality check has been conducted because the accuracy of the geodetic coordinates is not critical except of very rough terrain.

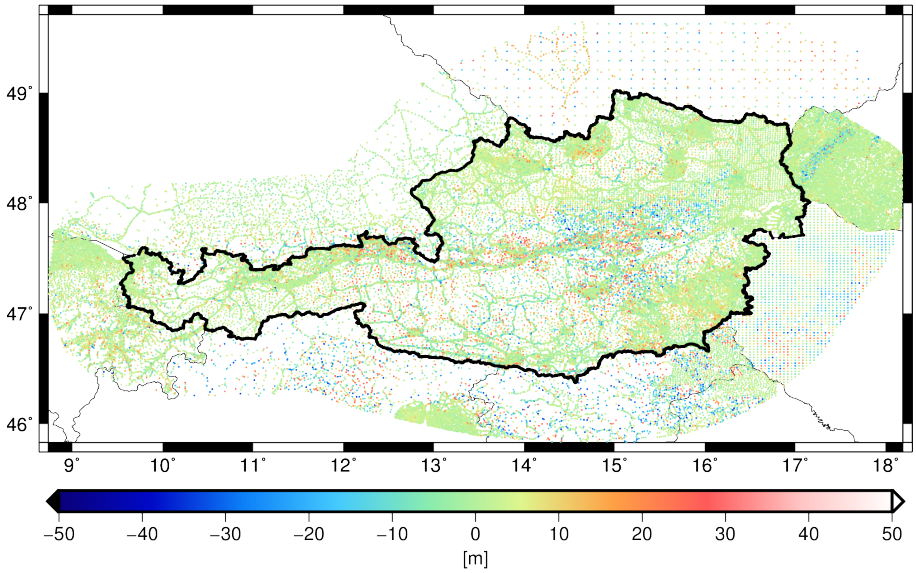

Figure 4.8: Differences between gravity station height and the nearest DTM point; Most of the occurring differences are located in the central part of Austria

The height differences in Fig. 4.8 are up to ± 120 m, and the biggest differences occur in certain regions, for example, transition from a mountainous region to flatland as it is the case in central Austria. However, only a few gravity points display such large differences. They have not been removed from the input dataset because the improvement on the final computed geoid turns out not being significant. This is connected to investigations on the impact of the differences between the gravity station height and the DTM height. The gravity data heights have been corrected for the deviation to the DTM heights and vice versa. However, it was not possible to identify whether a possible height error is attributed to the DTM or to the gravity height since the geoid validation with GPS/leveling does not show significantly improvements in either case. As a consequence the data remain unchanged.

4.2.2 Deflections of the Vertical

In physical geodesy deflections of the vertical are primarily important for astrogeodetic geoid determination. In Austria, the first accurate measurements were carried out by *Kurt Bretterbauer* and *Gottfried Gerstbach* from the Technical University of Vienna during the period of 1970-1990 [see *(Bretterbauer and Gerstbach, 1983)*]. In case of Graz University of Technology, *Karl Rinner*, *Herbert Lichtenegger* and later also *Hans Sünkel (Sünkel et al, 1987)* are the three pioneers who provided first astronomical measurements. Furthermore, the BEV carried

out precise deflection measurements during the 1980s. The estimated geoid solution was published by *Erhard Erker* in 1987 *(Erker, 1987)*. In the year 2006, *Bernadette Wasle* provided some additional measurements in the South-East of Austria in her masters thesis. The corresponding results of this work can be found in *(Wiesenhofer, 2007)*. During the period of 2010-2015 *Beat Bürki* from ETH Zürich measured deflection of the vertical for the Koralm and Semmering tunnel projects with a digital astronomical measurement system *(Bürki et al, 2004)*. Some of these points are now part of the entire dataset, which currently consists of 735 measurements. They are shown for each component in Fig. 4.9 and Fig. 4.10.

In summary, currently the astrogeodetic measurements in Austria are based on the following contributors:

- 1976-1982 measurements in the eastern part of Austria, conducted by TU Vienna, TU Graz and BEV
- 1983-1986 measurements in the western part of Austria, performed by BEV
- 2006 measurements in the south-eastern part of Austria, carried out by TU Graz
- 2010-2015 measurements for the Koralm and Semmering tunnel projects, provided by TU Graz and ETH Zürich

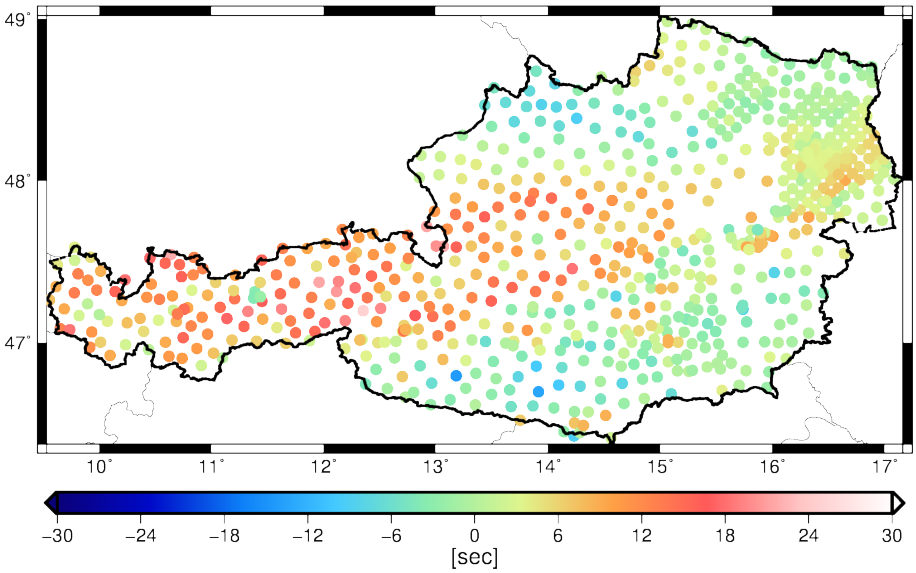

Figure 4.9: Measured 735 North-South ξ components

For the Austrian region the magnitude of the measured 735 deflections of the vertical is below $\pm$ 25". The statistics can be found in Tab. 4.2.

Another aspect which can directly be seen in both figures is the irregular point distribution of the measurements. A considerable amount of measurements is located in the eastern part of Austria, near Vienna. This is due to oil and gas exploration in those areas. Nevertheless, the deflections cover the entire Austrian territory but are notably sparse compared to the gravity measurements. In general, the overall precision of both, the ξ as well as the η component

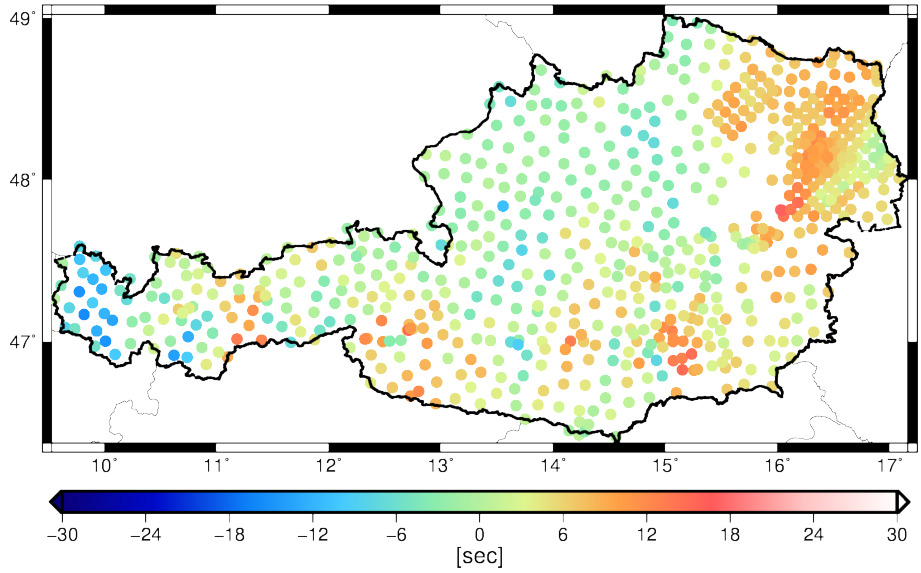

Figure 4.10: Measured 735 East-West η components

Table 4.2: Statistics of 735 measured deflections of the vertical

[sec]	min	max	mean
ξ	-14.18	24.78	3.59
η	-15.54	17.73	2.88

of the measurements, is assumed to be ± 0.30". This value was empirically determined in previous Austrian gravity field projects and is specified by the BEV. Results derived from the VCE method which are based on a relative weighting between the observation groups, are different. The corresponding investigation can be found in sec. 5.2.

A limiting factor for the practical use of deflections for precise geoid determination is linked to historical reasons because most of the Austrian measurements are taken before the GPS-based timing became available. To determine the East-West component of the deflections, accurate time measurements are needed because the determination of the astronomical longitude Λ was derived from the transition time of a star passing through the meridian. Further details related to astronomical measurements may be found in *(Wiesenhofer, 2007)*. In contrast, the North-South component is not affected by such a time component and can therefore been assumed as better determined in comparison to the East-West component. Nowadays, a modern zenith camera is equipped with a GPS antenna (see Fig. 4.11). Therefore, the ellipsoidal coordinates as well as the time stamp (global GPS time) can be derived exactly.

Today, measured deflections of the vertical can reach the ± 0.1" accuracy level. Such a modern system uses a star tracker to determine the astronomical latitude Φ and longitude Λ very accurately. By means of subtracting the ellipsoidal coordinates, the deflections can be directly obtained (see sec. 3.5.3). A zenith camera system allows for an automated and simplified observation process with the additional benefit of being independent of any subjective errors,

as they often occur in visual methods. In this case, the processing chain includes leveling as well as a star field, imaged on a CCD array and the data transfer. The determination of the ellipsoidal coordinates is less critical, and its accuracy is assumed to be of a few centimeters. By means of the rule of thumb, that 1" $\approx$ 30 m on the Earth's surface, this leads to errors of some milli-arcseconds and can be neglected in the deflection error budget. Depending on the weather conditions, about 50 measurements are carried out by a single station to obtain the final average value. Therefore, it is possible to determine several individual deflection measurements during a single night. More information related to this topic can be found in *(Hirt et al, 2010)*.

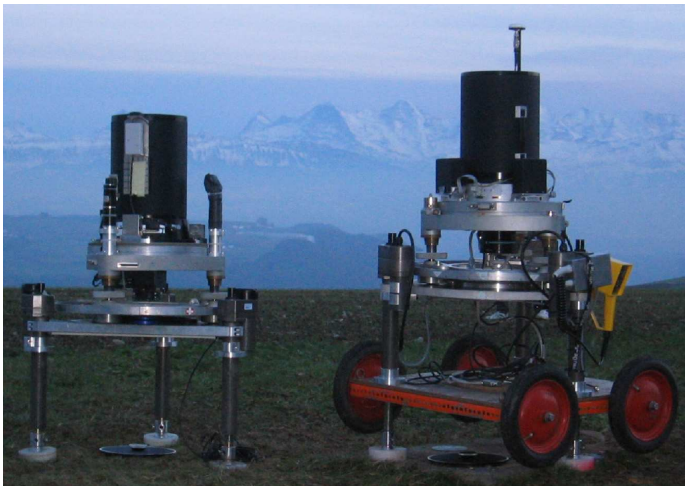

Figure 4.11: Digital zenith camera systems for the direct measurement of deflections of the vertical during a parallel observation session [courtesy by *(Hirt et al, 2010)*]

4.2.3 GPS/Leveling Observations

Currently there are 192 GPS/leveling observations available which are provided by the BEV. The present national Austrian geoid solution is highly constrained to a subset of 170 measurements. They are used as datum points to overcome inconsistencies in the geoid modeling and to obtain the correction surface (see sec. 4.1.1).

GPS/leveling observations are characterized by having both, on the one hand high precise spirit leveling which provides the orthometric height H component and and on the other hand GPS long-term measurements which are responsible for an accurate determination of the ellipsoidal height h. For the latter, the BEV specifies an accuracy of < 1 cm. For the orthometric height, no reliable accuracy information is provided. Nevertheless, the accuracy of these observations is expected to be on the level of a few centimeters. By means of $N = h - H$ the absolute geoid height with respect to the a reference ellipsoid can be directly obtained. In Fig. 4.12 the measurement principle is shown. In Fig. 4.13 the dataset of 192 measured geoid heights used for the validation is presented. The corresponding statistics may be found in Tab. 4.3.

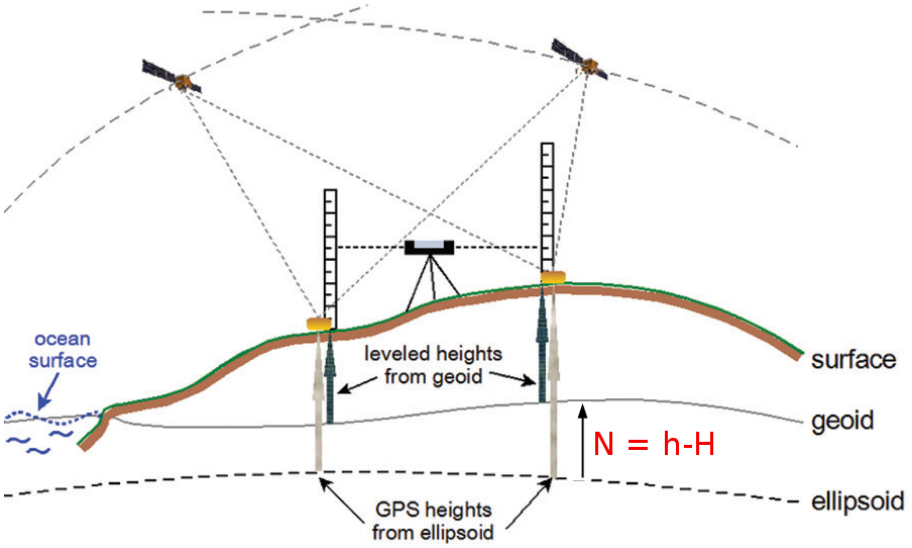

Figure 4.12: Measurement principle of GPS/leveling [courtesy by NRCAN[2]]

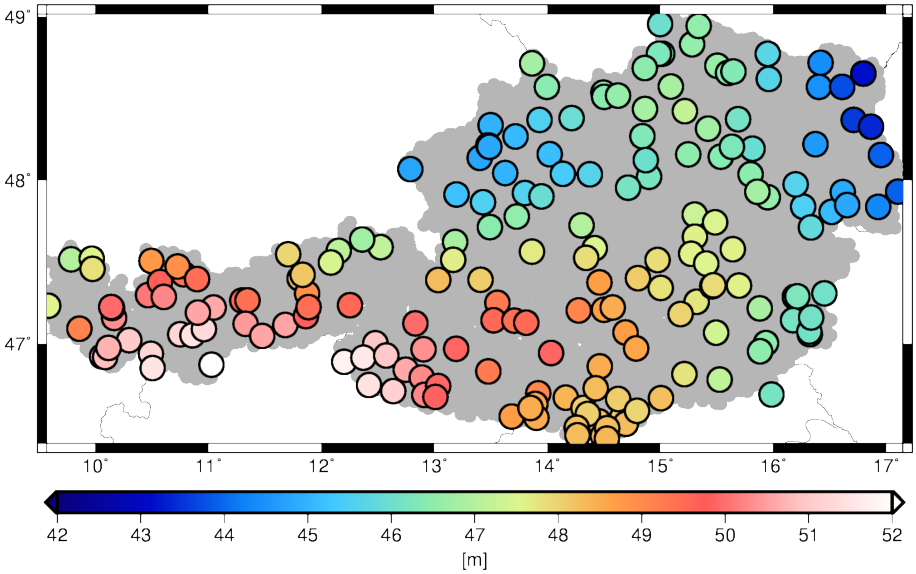

Figure 4.13: 192 measured geoid heights provided by the BEV

In contrast to the official Austrian geoid solution, these GPS/leveling observations are only used for validation purposes within this thesis. It is also important to understand that the GPS/leveling measurements are constraint to the European Vertical Reference System 2000, which is defined as tide-free system. This leads to inconsistencies and a possible mixture since the reference of most of the leveling datasets is unknown. This is also a probable source of errors when comparing the computed gravimetric geoid solution with GPS/leveling observations. More on this topic can be found in sec. 7.3.

[2] www.nrcan.gc.ca

Table 4.3: Statistics of 192 measured geoid heights

[m]	min	max	mean
N	43.14	52.15	47.69

The national Austrian geoid solution is constrained to 170 GPS/leveling observations (see sec. 4.1.1). The GPS/leveling observations are subject of continuous improvements. During the period of 2009-2010, the BEV undertook a re-evaluation of the entire dataset. As a result of the review process, about 30% of the GPS/leveling measurements changed significantly, either due to changes in the ellipsoidal heights or due to a corrected orthometric height. Unfortunately, these changes are not part of the official Austrian geoid solution. As the present national solution is highly constrained to the older set of 170 GPS/leveling observations it suffers from the evaluation process and is not consistent with the updated set of 192 measurements. During this period 22 measurements were newly established. The occurring geoid height changes are illustrated in Fig. 4.14.

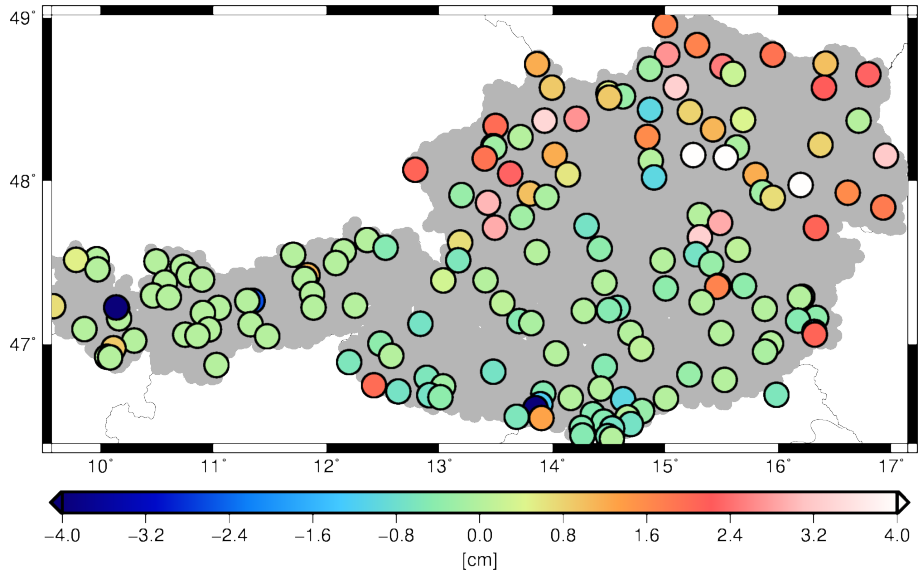

Figure 4.14: Changes of the GPS/leveling observations during the period of 2009-2010 initialized by the GEOID+ project

At some stations the differences are up to ± 8 cm and the rms is 1.6 cm. However, the new dataset is clean of big outliers and the accuracy of these observations are supposed to be on the level of a few centimeters. A comparison of the new dataset with the official Austrian geoid solution was conducted by *(Rieser, 2015)*. The results show a maximum variation from -6.4 cm to 7.5 cm with a corresponding rms value of 2.2 cm. Based on these differences it is possible to conclude that a change of the GPS/leveling heights would also require a complete recalculation of the official Austrian geoid. Further comparisons with the national geoid can be found in chapter 7.

4.3 Digital Terrain Models

4.3.1 Austrian Digital Terrain Model

The BEV provides a DTM up to a high resolution of 1.40625"×2.34375" which corresponds to approximately 44×49 m. This dense DTM is available only within the central European region. First work on the DTM goes back to *Diethard Ruess* and *Josef Graf* [see *(Ruess, 1984)* and *(Graf, 1996)*]. Based on new technologies, for example by the Space-Shuttle-Topography-Mission (SRTM), an ongoing process of DTM improvements can be observed over the years. In addition, new high-precise photogrammetric data from Austria, Switzerland, Slovenia and South Tyrol has been incorporated. The combination of the different data sources, for example, SRTM and airborne datasets, was the final step on the way to a complete and consistent Austrian DTM. In general, SRTM data was used to fill data gaps in the central European region and to form the final DTM as shown in Fig. 4.15. With the new SRTM+ data the bathymetrical information over the oceans is also available. The height accuracy of the SRTM-3 data has been specified by the Jet Propulsion Laboratory (JPL) with ± 20 m [see e.g. *(Smith and Sandwell, 2003)*]. More information on the SRTM mission can be found on the official SRTM web page.[3]

For a detailed description of DTM evolution the reader is referred to *(Mayerhofer, 2007)*. The currently available Austrian DTM is based on orthometric heights, whereas the horizontal coordinates are related to the WGS-84 system (see sec. 2.2.3).

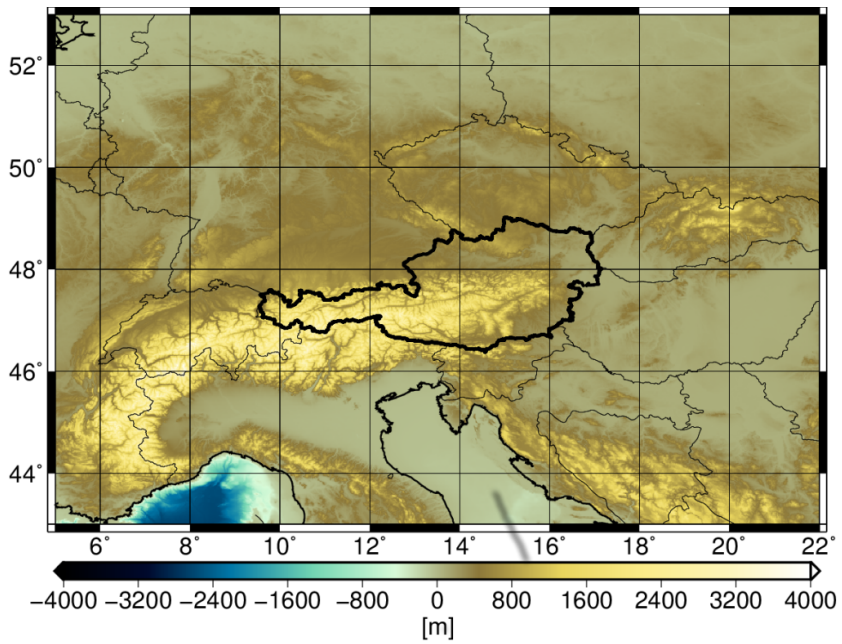

Figure 4.15: High resolution DTM within central Europe

[3] http://www2.jpl.nasa.gov/srtm/

In general, the DTM is given within the following borders:

φ= 43°-53° ,

λ= 5°-22° .

Based on the original resolution, different coarse DTM models have been derived by computing weighted mean values. In particular, the following resolutions are calculated:

Table 4.4: Different DTM resolutions

Notation	Resolution	Number of Points
BEV00	1.40625”×2.34375”	668.467.200
BEV01	2.8125”×4.6875”	167.116.800
BEV02	5.625”×9.375”	41.779.200
BEV03	11.25”×18.75”	10.444.800
BEV04	22.5”×37.5”	2.611.200
BEV05	45”×75”	652.800
BEV06	90”×150”	163.200

Due to a historical evolution of the DTM, uncertainties in the obtained orthometric heights of about ± 2.5 m within Austria can be expected. This specification depends on whether the terrain is flat or mountainous. In mountainous regions the uncertainty can reach the ± 20 m level, depending on the land coverage and recording method *(Mayerhofer, 2007)*. Besides the European coverage there is also a global coverage available, which is described in the following section.

4.3.2 GTOPO Model - Global DTM Coverage

In order to provide a global DTM coverage for investigations, the GTOPO[4] model, which consists of several data sources, has been additionally considered. The original GTOPO dataset was completed in 1996, during the following years ongoing improvements were applied and today the latest SRTM+ datasets are also incorporated to provide an updated topographic model. The GTOPO model essentially consists of different merged elevation information and is provided by the U.S. Geological Survey *(USGS, 2014)*. For the investigation of the distant zone contribution the originally given 30 arc seconds[5] resolution was not used. A data thinning step was applied. The coarse DTM resolution used is of about 4×4 km. In order to combine the high resolution DTM provided by the BEV with the GTOPO dataset, the height values are set to zero in the overlapping area. This is shown in Fig. 4.16.

As also can be clearly seen in Fig. 4.16, the GTOPO model only provides information above sea level. The ocean covered regions are set to zero. Furthermore, there is no corresponding

[4] https://lta.cr.usgs.gov/GTOPO30
[5] 30” ≈ 1 km

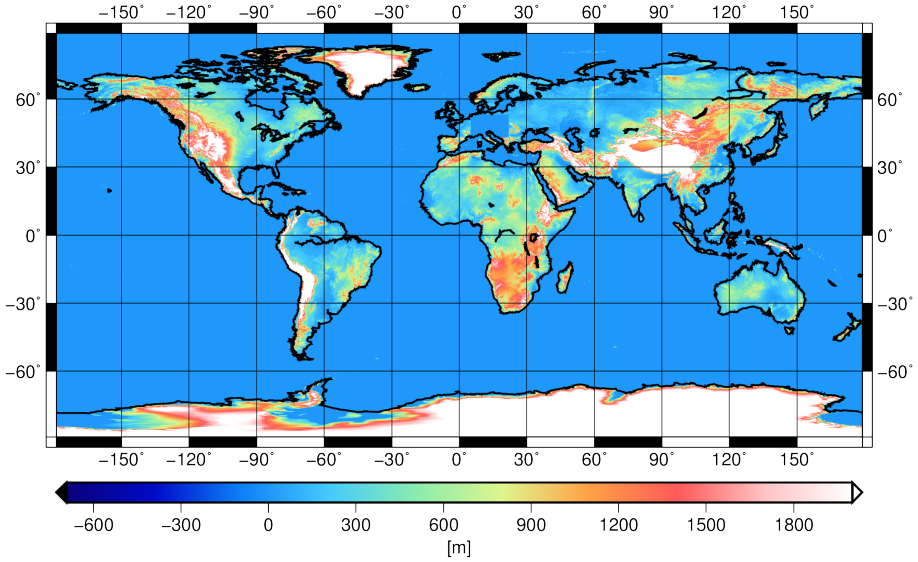

Figure 4.16: Global DTM coverage provided by the GTOPO model; For the combination with the Austrian DTM, the overlapping part is set to zero

density information available. For example, Greenland is completely covered by snow and ice which does not correspond to the density assumption of solid rock. The heights are also originally related to the WGS-84 system and geoid heights are necessary in order to provide orthometric heights *(USGS, 2014)*.

The impact of additional masses coming from the distant zones had never been investigated in the frame of Austrian geoid computation. With the GGM information on one hand, and the global DTM coverage on the other hand, both information types are now valid on a global scale. Results related to this topic can be found in sec. 7.4.4. A set of topographic coefficients has been computed for the GTOPO model in order to provide a correct representation of the topographic masses in the spectral domain. A general height accuracy of ± 30 m has been specified by the USGS depending on the individual data source.

4.4 General Aspects of Density Information

For the topographic/isostatic or atmospheric reduction, the knowledge of the topography, as well as an assumption about the density distribution is needed in order to calculate different kinds of reduction. In case of the topographic/isostatic compensation, a common approach is to use a standard crustal density value of 2670 kg/m^3 which refers to the density of the Earth's crust. In this case no further information about the density in the area of interest is available. Indeed, this is only an assumption and therefore density anomalies which are different from this standard value remain in the reduced gravity. A typical geological structure of different density is the so-called Tauern window [see e.g. *(Meurers et al, 2001)*]. Fortunately, there is density information apart from the constant standard assumption available.

This is not the first attempt to introduce density information into the geoid computation process for Austria. During the past decades, for example, *Norbert Kühtreiber* from Graz University of Technology has also used the same lateral density data for several investigations. The final outcome was that no significant differences, based on the density information in comparison to the constant standard crustal density assumption, can be observed [see *(Kühtreiber, 1998a)* or *(Kühtreiber et al, 2011)*]. Due to a more consistent RCR procedure this result has been revised. In sec. 7.4.2 at least a slight improvement of the results in the remove and restore steps, as well as in the final estimated geoid, can be observed. A visual representation of the different density models is provided in the following sections.

4.4.1 2D Surface Density Model

Based on geological observations a surface density model for the Austrian territory becomes available in the early 1950s. Initial work has been carried out by *Harald Granser* and further details are provided by *(Rinner, 1983)*. This type of information is closely connected to the rocks and geological structures (compare Fig. 4.17 and Fig. 4.18). It is valid for the Earth's surface, but no serious statement about the density distribution in the Earth's interior contributing towards the geoid level is possible. In this research the impact of this effect on the geoid computation is also of interest and has been investigated. The original density resolution has been interpolated to the corresponding DTM spacing, which makes it available for the RCR procedure.

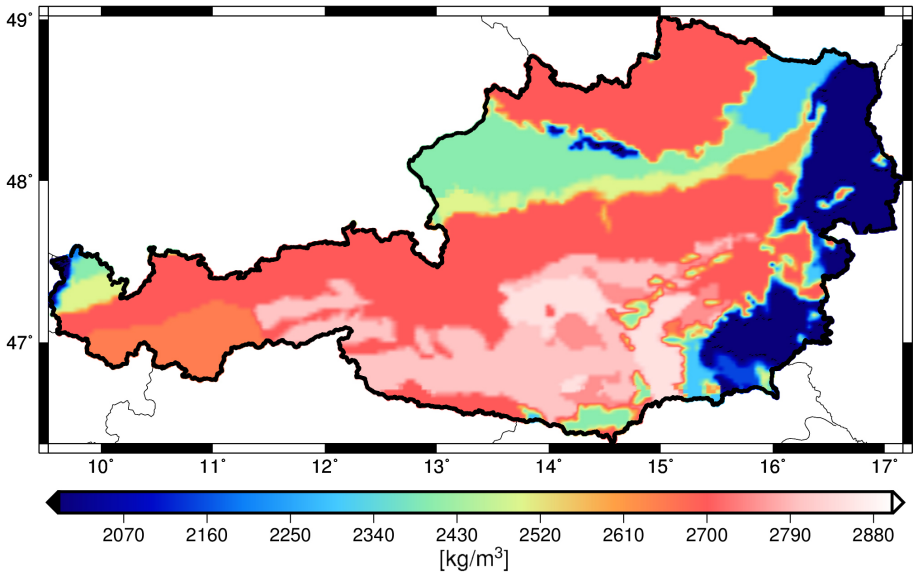

Figure 4.17: 2D Austrian density model based on geological observations

The use of a surface density model leads to smoother gravity data and to a slightly improved geoid, compared to GPS/leveling observations. To support this statement, the corresponding results can be found in sec. 7.4.2. This is important when discussing precise geoid computation requirements. In Fig. 4.18 the geological structures of Austria can be seen. The 2D density

model is strongly correlated with the rocks and provides many geological features. Not all of these are reflected in the density map, but in general a great deal of variety can be observed when compared to an ordinary constant standard density assumption of 2670 kg/m^3.

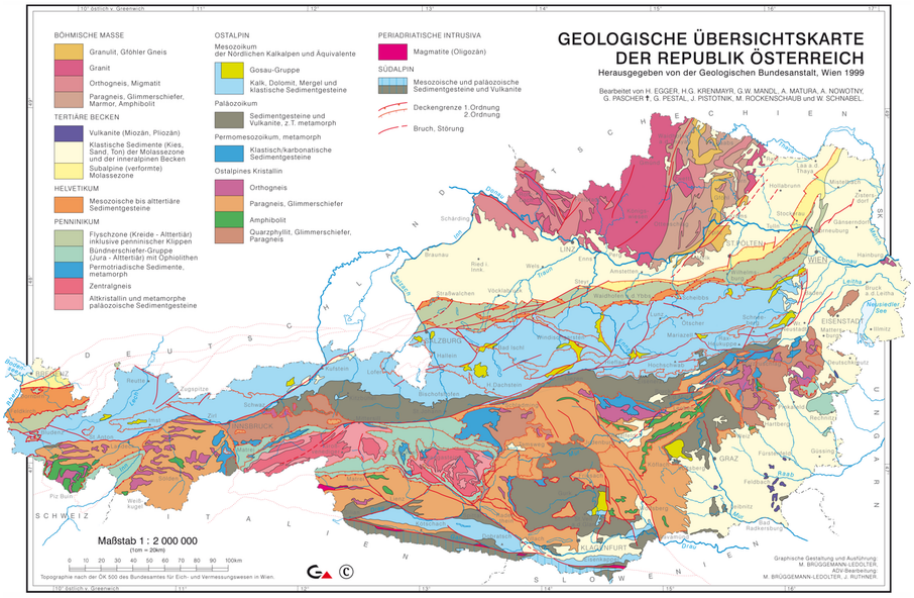

Figure 4.18: Geological map of Austria [courtesy by Geological Survey Austria[6]]

4.4.2 3D Seismic Density Model

For the purpose of scientific research a 3D density model for the central European region has been provided by the Technical University of Vienna for the GEOID+ project (see sec. 4.1.2). This model originally consists of ellipsoidal WGS-84 related coordinates and variable vertical density values, derived from seismic tomography *(Behm et al, 2008)*. Unfortunately, the model does not cover the entire Austrian territory. In the western part of Austria ($\lambda < 11°$) no seismic data are available (see Fig. 4.19). The relationship between seismic velocity and density is based on the Christensen-Mooney relation, where the seismic velocity is directly transformed into density information *(Christensen and Mooney, 1995)*.

The seismic model originally consists of 11 layers, starting from 0 km to -10 km and is actually able to cover deep and large scale structures. Within this research only the top layer (0 km) which refers to the sea level, and to a geoid given a global scale, has been used. The isostatic long wavelength components underneath are assumed to be well covered by a GGM and can be neglected within the RCR procedure as shown in sec. 7.4.7.

In sec. 7.4.2 an investigation on the impact and performance of different density assumptions has been made. One of these assumptions is the so-called hybrid model, which represents an attempt to combine geological and seismic data is briefly discussed in the following section.

[6] www.geologie.ac.at

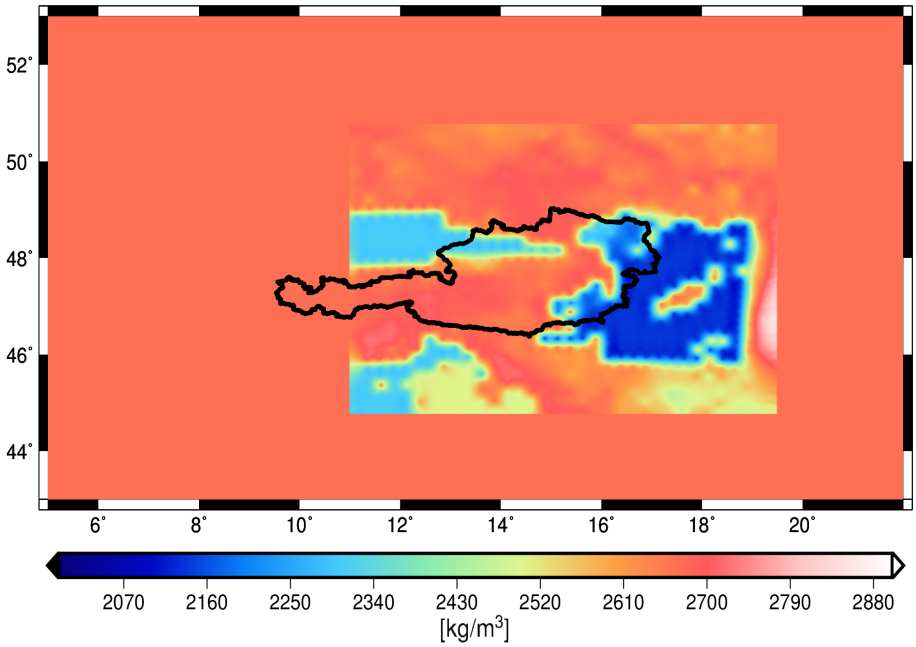

Figure 4.19: Top layer (0 km) of seismic 3D density information

4.4.3 Hybrid Density Model

Basically, this model consists of two different datasets. The top layer of the hybrid model is based on the 2D surface density information and the bottom layer is provided by 3D seismic tomography, as shown in Fig. 4.19. The remaining area was again filled with standard crustal density values, which also holds for the other models. The hybrid density combination is given according to

$$\rho_{hyb} = \frac{\rho_{2D} + \rho_{3D}}{2} \ , \tag{4.1}$$

and in areas where only the 3D information is available the standard crustal density ρ is introduced as

$$\rho_{hyb} = \frac{\rho + \rho_{3D}}{2} \ . \tag{4.2}$$

Please note, that this is only an attempt to combine these two different datasets for the purpose of geoid computation. For the purpose of an integrated interpretation, for example as it is necessary for gas and oil exploration decisions, it is not suitable. In the western part of Austria ($\lambda < 11°$) the hybrid model converts to the 2D surface density model, because here the 3D model does not provide information. Finally, the resulting hybrid density model is shown in Fig. 4.20.

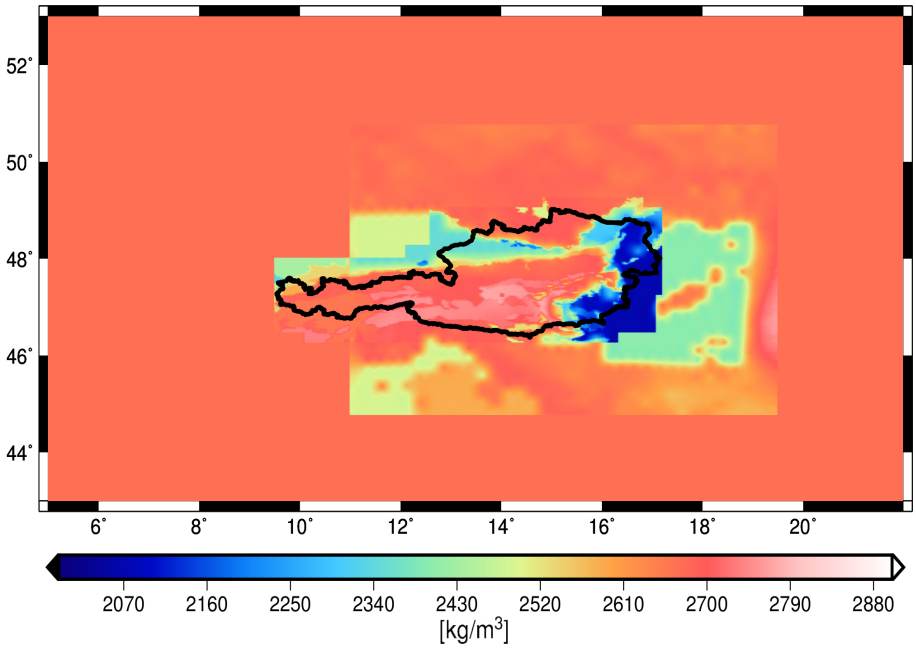

Figure 4.20: Hybrid density model

To summarize, a statistics of different density models used in this thesis can be found in Tab. 4.5. The original density information is given on an approximately 4×4 km resolution for the 2D surface density and on approximate 20×20 km for the seismic 3D measurements. To make this information usable, the density information has been interpolated to the resolution of the corresponding DTM, which is taken into account for the computation. In this case for every mass column a corresponding density value is available. In areas where the model does not provide density information, the standard crustal density value of 2670 kg/m^3 is assigned.

Table 4.5: Statistics of all used density models

Model	*min* $[kg/m^3]$	*max* $[kg/m^3]$	*mean* $[kg/m^3]$
Surface Density Model	2000.00	2852.00	2579.60
3D Density Model	2102.70	2870.56	2628.57
Hybrid Density Model	2054.95	2775.27	2641.67
Standard Density Model	2670.00	2670.00	2670.00

5 Least Squares Adjustment

5.1 Principles of Least Squares Estimation

The basics of a least squares approach (Gauss-Markov model) are explained in this section because it provides the mathematical backbone for the estimation of the unknown parameters. The used notation is taken from *(Montenbruck and Gill, 2000)*.

The observations and unknown parameters are linked by a functional model and noise. The observations are grouped in the observation vector $\boldsymbol{y}$. The functional model $\boldsymbol{f}$ includes observation equations related to the estimation parameters which are contained in the vector $\boldsymbol{x}$. Taking into account the residual vector $\boldsymbol{\epsilon}$, the observation equation reads

$$\boldsymbol{y} = f(\boldsymbol{x}) + \boldsymbol{\epsilon} \ . \tag{5.1}$$

The model is typically overdetermined, that means compared to the number of unknowns to determine a larger amount of observations is available. Furthermore, in case of a non-linear model the first step is to linearize it by means of approximated values for the unknown parameters. The linearization of the model can be performed by a Taylor series as

$$\boldsymbol{y} = \boldsymbol{y}_0 + \frac{\partial f(\boldsymbol{x})}{\partial \boldsymbol{x}}\Big|_0 (\boldsymbol{x} - \boldsymbol{x}_0) + ... \ , \tag{5.2}$$

which is truncated after the linear term. The linearization, attributed to a reference solution with a-priori values for the unknowns is given according to

$$\boldsymbol{y} = \boldsymbol{f}(\boldsymbol{x}_0) + \boldsymbol{A}\Delta\boldsymbol{x} + \boldsymbol{\epsilon} \ , \tag{5.3}$$

where $\boldsymbol{A}$ denotes the design matrix which is defined as

$$\boldsymbol{A} = \frac{\partial \boldsymbol{f}(\boldsymbol{x})}{\partial \boldsymbol{x}}\Big|_{x=x_0} \ . \tag{5.4}$$

The linearized model reads $\boldsymbol{y}_0 = f(\boldsymbol{x}_0)$, and reveals in linearized observations $\Delta\boldsymbol{y} = \boldsymbol{y} - \boldsymbol{y}_0$ as well as supplements to the unknown parameters $\Delta\boldsymbol{x} = \boldsymbol{x} - \boldsymbol{x}_0$. The entire linear system of equations in matrix notation can be written as

$$\Delta \boldsymbol{y} = \boldsymbol{A}\Delta \boldsymbol{x} + \boldsymbol{\epsilon} \ , \tag{5.5}$$

where the Gauss-Markov model assumes that the measurement errors have an expectation value of zero. The stochastic behavior of the model is characterized by the covariance matrix of the observations, denoted as $\boldsymbol{Q}$. This matrix is defined according to

$$\boldsymbol{Q} = \sigma_0^2 \ \boldsymbol{P}^{-1} \ , \tag{5.6}$$

where σ_0^2 is the unknown variance factor. Considering the weight matrix $\boldsymbol{P}$, the minimum condition of the normal equation system reads

$$\boldsymbol{0} = \boldsymbol{A}^T\boldsymbol{P}\boldsymbol{A}\Delta\hat{\boldsymbol{x}} - \boldsymbol{A}^T\boldsymbol{P}\Delta\boldsymbol{y} \ . \tag{5.7}$$

Rearranging Eq. (5.7) leads to supplements to the estimated parameter vector, given as

$$\Delta\hat{\boldsymbol{x}} = (\underbrace{\boldsymbol{A}^T\boldsymbol{P}\boldsymbol{A}}_{\boldsymbol{N}})^{-1}\boldsymbol{A}^T\boldsymbol{P}\Delta\boldsymbol{y} \ . \tag{5.8}$$

Therein $\boldsymbol{A}^T\boldsymbol{P}\boldsymbol{A}$ denotes the normal equation matrix $\boldsymbol{N}$. This matrix is characterized as symmetric. The final adjusted model parameters are now given by

$$\hat{\boldsymbol{x}} = \boldsymbol{x}_0 + \Delta\hat{\boldsymbol{x}} \ . \tag{5.9}$$

The entire adjustment process is solved iteratively and the connection to the Remove-Compute-Restore (RCR) technique (see sec. 6.1) is given by the linearized observations $\Delta\boldsymbol{y}$ which are introduced in the remove step, the supplements to the parameters $\Delta\hat{\boldsymbol{x}}$ are estimated in the compute step and the final parameters $\hat{\boldsymbol{x}}$ are used in the restore step.

The stochastic behavior of the estimated parameters can by scaled by an a-posteriori variance, which can be calculated according to

$$\hat{\sigma}_0^2 = \frac{\hat{\boldsymbol{\epsilon}}^T\boldsymbol{P}\hat{\boldsymbol{\epsilon}}}{n-u} \ , \tag{5.10}$$

where $n-u$ describes the degree of freedom computed as the difference between the number of observations n minus the number of estimated parameters u. Additionally, the covariance matrix of the estimated parameters can be obtained according to

$$\boldsymbol{Q}_{\hat{x}} = \hat{\sigma}_0^2\boldsymbol{N}^{-1} \ . \tag{5.11}$$

For the estimation of the a-posteriori variances, the Variance Component Estimation (VCE) method is used. More on this topic can be found in sec. 5.2. In addition, the quality of the chosen model can be verified by means of the corresponding residuals. The estimated observations $\hat{\boldsymbol{y}}$ are computed by

$$\hat{\boldsymbol{y}} = \boldsymbol{A}\hat{\boldsymbol{x}} \ , \tag{5.12}$$

and the post-fit residual vector follows according to

$$\hat{\boldsymbol{\epsilon}} = \boldsymbol{y} - \hat{\boldsymbol{y}} \ . \tag{5.13}$$

5.2 Regularization Issues and Variance Components

As will be shown in sec. 6.3.4, a vast amount of homogeneously distributed unknown parameters u to determine are needed in order to ensure a proper gravity field representation. Conversely, the amount of inhomogeneous distributed gravity field observations n is limited due to computational efforts. According to the least squares approach, an overdetermined system, that means more observations than unknown parameters, is assumed. In this case, the entire equation system (see sec. 5.1) can be solved under the assumption that the estimated parameter vector $\hat{\boldsymbol{x}}$ is replacing the exact solution vector $\boldsymbol{x}$, with the minimum condition of $\|\hat{\boldsymbol{\epsilon}}\|^2$, which represents the minimized square sum of the residuals.

In comparison to global gravity field modeling, where no spatial cut off errors occur, regional gravity field modeling is spatially limited within a certain region and an edge effect occur. Another aspect is the inhomogeneous input data distribution, which leads to the situation that the entire equation system might be ill-posed. Therefore, the least squares minimum condition itself does not lead to a stable solution and some kind of stabilization process needs to be applied in order to stabilize the entire equation system. From a mathematical point of view, the instability of the design matrix $\boldsymbol{A}$ can be treated by adding a-priori information about the solution to constrain the estimation result. One possible way in order to recognize an equation system to be well- or ill-posed, is to investigate the condition number, which is defined according to *(Higham, 1987)*

$$\mathrm{cond}(\boldsymbol{A}) = \|\boldsymbol{A}\|\|\boldsymbol{A}^{-1}\| \ . \tag{5.14}$$

If the condition number is small, the equation system or the matrix $\boldsymbol{A}$ is well conditioned. In case of a large condition number, the system needs to be stabilized in any way. There are several methods to deal with ill-posed systems as, for example, described in *(Naeimi, 2013)* or *(Eicker, 2008)*.

For geoid determination, the regularization is embedded within the Remove-Compute-Restore (RCR) procedure. The remove step provides the necessary a-priori information for the regularization due to the use of long- and short wavelength components which have been reduced from the original gravity field signal. In this thesis the approach of Tikhonov regularization *(Tikhonov, 1963)* has been applied, which is described in the following.

5.2.1 Tikhonov Regularization

Regularization may be applied by means of a refinement of the original observation model, which is provided in a least square sense by means of Eq. (5.5), with the corresponding weight matrix given by Eq. (5.6), which includes the covariance information of the observations. Following *(Naeimi, 2013)*, and supposing that this information can be expressed by a refined model as

$$\boldsymbol{L}\boldsymbol{x} = \boldsymbol{s} \ , \quad \text{with} \quad \boldsymbol{Q}_s = \sigma_s^2 \ \boldsymbol{P}_s^{-1} \ , \tag{5.15}$$

where $\boldsymbol{L}$ is the regularization matrix and $\boldsymbol{s}$ a functional of the unknown parameters $\boldsymbol{x}$. A combination with Eq. (5.5) obtains the following combined equation system

$$\begin{bmatrix} \boldsymbol{A} \\ \boldsymbol{L} \end{bmatrix} \boldsymbol{x} = \begin{bmatrix} \boldsymbol{y} \\ \boldsymbol{s} \end{bmatrix} \ . \tag{5.16}$$

This normal equation system can be further reformulated as

$$(\boldsymbol{N} + \boldsymbol{K})\boldsymbol{x} = \boldsymbol{y} + \boldsymbol{u} \ , \tag{5.17}$$

where $\boldsymbol{K} = \sigma_s^{-2}\boldsymbol{L}^T\boldsymbol{P}_s\boldsymbol{L}$ and $\boldsymbol{u} = \sigma_s^{-2}\boldsymbol{L}^T\boldsymbol{P}_s\boldsymbol{s}$. By means of introducing the regularization parameter

$$\gamma^2 = \frac{\sigma_0^2}{\sigma_s^2} \ , \tag{5.18}$$

the full equation system reads

$$(\boldsymbol{A}^T\boldsymbol{P}\boldsymbol{A} + \gamma^2\boldsymbol{K})\boldsymbol{x} = \boldsymbol{A}^T\boldsymbol{P}\boldsymbol{y} + \gamma^2\boldsymbol{L}^T\boldsymbol{P}_s\boldsymbol{s} \ , \tag{5.19}$$

with the equivalent minimum condition of

$$\min(\|\hat{\boldsymbol{\epsilon}}\|^2 + \gamma^2\|\hat{\boldsymbol{\epsilon}_s}\|^2) \ . \tag{5.20}$$

This gives the generalized form of regularization of an ill-posed problem, depending on the prior information introduced by $\boldsymbol{s}$. At this point it has to be mentioned that these information corresponds to the remove step as discussed in sec. 5.2 and the regularization is applied towards zero $\boldsymbol{s} = \boldsymbol{0}$. Further let $\boldsymbol{P}_s = \boldsymbol{I}$, Eq. (5.19) depends strongly on the a-priori chosen $\boldsymbol{L}$, as well as on the regularization parameter γ^2, which leads to Tikhonov regularization *(Tikhonov, 1963)* in a strict sense. For gravity field estimation this method is a common approach to solve ill-posed problems numerically. This type of regularization is characterized by a regularization matrix and a corresponding regularization parameter.

The so-called standard Tikhonov regularization may be derived by means of the additional assumption of $\boldsymbol{L} = \boldsymbol{I}$. With this assumption, the unit matrix is introduced and theoretically it is possible to refine the regularization. Then it is also possible to distinguish between land or ocean areas [see e.g. *(Eicker, 2008)*].

One constant regularization parameter is introduced for each unknown parameter and the regularization reads

$$(\boldsymbol{A}^T\boldsymbol{P}\boldsymbol{A} + \gamma^2\boldsymbol{I})\boldsymbol{x} = \boldsymbol{A}^T\boldsymbol{P}\boldsymbol{y} \ , \tag{5.21}$$

and the corresponding minimum condition is given as

$$\min(\|\hat{\boldsymbol{\epsilon}}\|^2 + \gamma^2\|\boldsymbol{x}\|^2) \ , \tag{5.22}$$

which further means that not only the norm of the residuals $\hat{\boldsymbol{\epsilon}}$ is minimized but also the norm of the solution $\boldsymbol{x}$. This circumstance implies the regularity of the solution. Finally, the regularized solution vector, here denoted as $\hat{\boldsymbol{x}}_\gamma$, can be obtained by

$$\hat{\boldsymbol{x}}_\gamma = (\boldsymbol{A}^T\boldsymbol{P}\boldsymbol{A} + \gamma^2\boldsymbol{I})^{-1}\boldsymbol{A}^T\boldsymbol{P}\boldsymbol{y} \ . \tag{5.23}$$

In this case the solution is strongly dependent on the chosen regularization parameter and this choice is also essential in order to keep the balance between the fit to a-priori information and the regularity of the solution *(Eicker, 2008)*. For this research, one regularization is applied for the complete region. This means that in areas with a vast amount of terrestrial data the chosen regularization might be too strong whereas in areas with sparse observations the regularization dominates the solution. Therefore, the regularization is a trade-off between data fitting and stabilizing the solution *(Metzler, 2007)*. By means of VCE, a regularization parameter which controls the power of the regularization is estimated.

5.2.2 Variance Component Estimation

The VCE applied within this thesis is based on *(Koch and Kusche, 2002)*. In general, it is suitable to iteratively determine a regularization parameter, and to find a proper weighting among the individual observation groups. Not only different types of observations are weighted relatively to each other, for example gravity data and deflections of the vertical. It is also possible to find an individual weight for observation groups which consist of the same type of observation.

The normal equation system $\boldsymbol{N}$ can be established by an accumulated sum of the weighted individual normal equation systems $\boldsymbol{N}_k$, depending on the different observation groups taken into account (see also 5.2.3 and sec. 7.2.3). Additionally, one group of regularization parameters for all basis functions is introduced. These parameters will be constant, representing one mean value for the entire area of interest. According to *(Eicker, 2008)*, the total system expressed as combination of the individual normal equations can be written as

$$\underbrace{\boldsymbol{A}^T\boldsymbol{P}\boldsymbol{A}}_{\boldsymbol{N}}\boldsymbol{x} = \underbrace{\boldsymbol{A}^T\boldsymbol{P}\boldsymbol{y}}_{\boldsymbol{n}} \ , \tag{5.24}$$

with

$$\boldsymbol{N} = \sum_k \frac{1}{\hat{\sigma}_k^2}\boldsymbol{N}_k \ , \quad \text{and} \quad \boldsymbol{n} = \sum_k \frac{1}{\hat{\sigma}_k^2}\boldsymbol{n}_k \ . \tag{5.25}$$

This includes an a-priori initial value $\hat{\sigma}_k^2$ for every individual observation group. The VCE weighting arguments are given as the reciprocal variances of the normal equation system according to

$$\hat{\sigma}_k^2 = \frac{\hat{\Omega}_k}{r_k} \ , \tag{5.26}$$

with $\hat{\Omega}_k$ being the square sum of the residuals of the k^{th} observation group

$$\hat{\Omega}_k = \hat{\boldsymbol{\epsilon}}_k^T\boldsymbol{P}_k\hat{\boldsymbol{\epsilon}}_k \ . \tag{5.27}$$

The partial redundancies are computed according to

$$r_k = n_k - \frac{1}{\hat{\sigma}_k^2}\text{trace}\left(\boldsymbol{N}_k\boldsymbol{N}^{-1}\right) \ , \tag{5.28}$$

with n_k denoting the number of observations of the k^{th} observation group. Finally, the overall redundancy can be computed as

$$\sum_k r_k = n - u \ . \tag{5.29}$$

In case of regularization, $\boldsymbol{s} = \boldsymbol{0}$, $\boldsymbol{L} = \boldsymbol{P}_s = \boldsymbol{I}$ is applied. The normal equation matrix $\boldsymbol{N}$ is extended to the regularized normal equation matrix as

$$\boldsymbol{N}_\gamma = \boldsymbol{A}^T \boldsymbol{P} \boldsymbol{A} + \gamma^2 \boldsymbol{I} \ . \tag{5.30}$$

The solution for $\hat{\boldsymbol{x}}$ and the variance components $\hat{\sigma}_k^2$ are a-priori unknown. Therefore, initial values must be defined for the iterative VCE process, which is utilized as:

1. Initial values $\hat{\sigma}_k^2$
2. Combining the normal equation matrix $\boldsymbol{N}$ and $\boldsymbol{n}$
3. Establish the system of equations $\boldsymbol{N}\boldsymbol{x}$=$\boldsymbol{n}$
4. Compute the solution for $\hat{\boldsymbol{x}}$ and estimate new variance components $\hat{\sigma}_k^2$ and r_k
5. If $\xrightarrow{convergence}$ STOP; if $\xrightarrow{no\ convergence}$ begin again at step 2

The VCE is a powerful tool to find a proper weighting among individual observation groups and also to determine a proper regularization parameter. By means of an appropriate initial choice of the variance components, the solution convergence is expected to be within a few iteration steps. In this thesis, the values from the official Austrian geoid solution 2007 have been used as initial values. The VCE method was utilized to check the empirically defined sigmas in previous Austrian geoid campaigns. To do so, only one set of observation groups representing the entire gravity dataset is considered. In addition, the following a-posteriori sigmas derived from VCE are obtained and compared with the empirical values chosen for the Austrian geoid solution. These values are shown in Tab. 5.1.

Table 5.1: Estimated σ compared to the official Austrian geoid solution

Parameter	**VCE method**	**Austrian geoid 2007**
Δg	0.95 mgal	1.00 mgal
ξ, η	0.54”	0.30”

The estimated sigma for the gravity anomalies is similar, whereas for the deflections of the vertical the sigma is different which is due to the redundancies and the relative weighting of the different observation groups using VCE.

5.2.3 Building Observation Groups

In order to define different observation groups for the same type of observation, some prior information is needed. This information has been provided by the Federal Office of Metrology and Surveying (BEV) (see sec. 4.2.1), where the gravity data within Austria can be separated according to the individual measurement systems and their corresponding accuracy information, which leads to three different groups. Another simple separation can be performed by means of the geographical location where the gravity data are divided by political boundaries, which leads to seven additional groups. For the sake of completeness it has to be mentioned that a few Lichtenstein gravity observations are merged with the Switzerland dataset. This also holds for some absolute gravity measurements within Austria because that small amount (35 measurements) does not justify an additional observation group, although they are the most accurate ones. Finally, this leads to ten individual gravity observation groups as shown in Fig. 5.1.

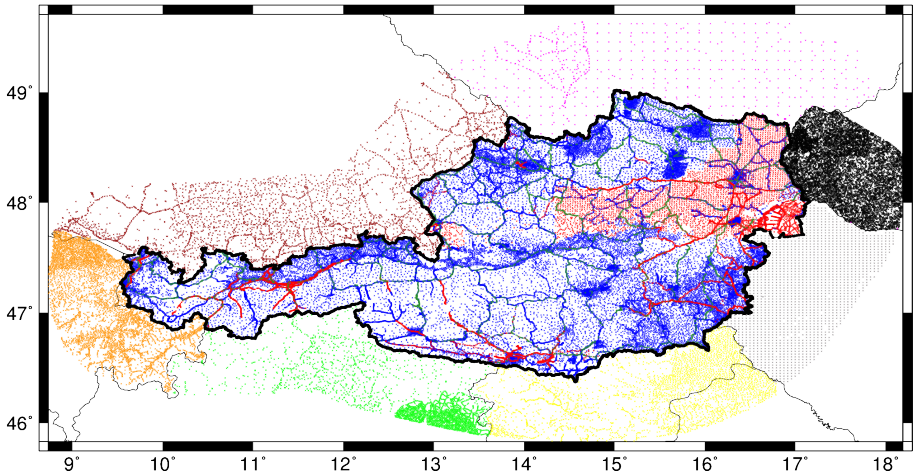

Figure 5.1: The entire gravity dataset of 72327 measurements divided into ten different observation groups; Within Austria the groups depend on the chosen measurement system with 35595 LCR and Scintrex in blue, 9339 Worden in red and 3818 Norgaard measurements in dark green; The remaining 23577 observations belong to the neighbouring countries

For the combined gravity field computation, the deflections of the vertical also have to be taken into account as an individual observation group. It turns out not being necessary to separate the ξ and η components, because their contribution to a combined solution is rather small (see sec. 7.2.3). The VCE method provides weighting among the different observation groups of the same type and also between different types of gravity field observations. Furthermore, a regularization parameter is estimated for every unknown RBF scaling coefficient in order to stabilize the entire equation system. The estimated variance components are of about 1 mgal within Austria and are shown in Tab. 5.2. It must be noted that the individual σ values are not comparable to the measurement accuracy, due to remaining modeling errors. More on this topic can be found in sec. 4.2.1.

Table 5.2: Estimated variance factors of the individual observation groups by means of VCE

Group	**Points**	$[\sigma]$
Austria - LCR	35595	1.10 mgal
Austria - Worden	9339	0.82 mgal
Austria - Norgaard	3818	0.85 mgal
Germany	3604	1.22 mgal
Switzerland	3150	1.13 mgal
Italy	2527	1.02 mgal
Slovenia	2236	1.05 mgal
Hungary	1535	0.22 mgal
Czech Republic	649	2.08 mgal
Slovakia	9282	0.58 mgal
Deflections of the vertical	735	0.54”
Regularization	37891	$1 \cdot 10^{-4}$

As can be seen in Tab. 5.2, the estimated variance components vary in the range of about 1 mgal. Especially in Hungary and Czech Republic, the estimated factors are too optimistic due to the fact the used input data are not real measurements but further processed and interpolated gravity. In general, for Austrian neighbouring countries, the quality of the measured gravity is unknown due to the fact that the measurements have grown historically, but VCE provides a method to deal with this problems.

6 Regional Gravity Field Modeling

The combination of various gravity field quantities and their different wavelengths behavior was one of the major challenges in this thesis. As shown in sec. 4.1, the official Austrian geoid solution is still affected by systematic errors between the gravimetric geoid solution and GPS/leveling observations. These errors are supposed to be coming from an inconsistent treatment of the topographic masses. Due to this reason, a non-physical correction surface, with a magnitude of several meters, has been introduced to absorb deficiencies in the modeling. This chapter presents a different approach, by means of a rigorous separation of the individual parts of the gravity field in the spectral domain. The general framework for gravity field modeling is the Remove-Compute-Restore (RCR) procedure, which will be described in the following.

6.1 Remove-Compute-Restore Technique

In general, the concept of the RCR approach *(Forsberg, 1984)*, *(Forsberg and Tscherning, 1997)*, or *(Hofmann-Wellenhof and Moritz, 2006)*, is to remove the short wavelength topographic, the atmospheric and the long wavelength part from the gravity field signal before computation. This results in gravity field quantities which are computed based only on a residual disturbing potential. Hence, the effect of the topographic and atmospheric masses, as well as the long wavelengths have to be restored after the computation. Finally, the achieved results will be validated with independent datasets. The RCR procedure is a common approach in regional gravity field modeling.

For the purpose of geoid modeling, and in order to fulfill the requirements of the Laplace equation, no attracting masses outside the geoid are permitted. If this is valid, the gravitational potential V and the disturbing potential T are characterized as harmonic (see sec. 3.1). In reality, topographic masses are located outside the geoid and in order to compute a geoid according to a harmonic function, which is based on the solution of the fundamental equation of geodesy (e.g. based on the Stokes formula *(Moritz, 1980a)* or *(Hofmann-Wellenhof and Moritz, 2006)*, or based on Fast Fourier Transformation *(Schwarz et al, 1990)*, or the Least Squares Collocation (LSC) method *(Moritz, 1962)* or *(Heiskanen and Moritz, 1967)*, these masses have to be removed in a mathematical manner.

In the framework of the RCR technique the a-priori non-linear observation equations are linearized. According to sec. 5.1, the general linearization of the equation system is given by

$$\Delta \boldsymbol{y} = \boldsymbol{A}\Delta \boldsymbol{x} + \boldsymbol{\epsilon} \ , \tag{6.1}$$

where the **remove step** is represented by $\Delta \boldsymbol{y} = \boldsymbol{y} - \Delta \boldsymbol{y}_0$. Within this step all known parts of the gravity field (long- and short wavelength components) are modeled and subtracted from the original measurements. Based on these linearized and reduced observations, supplements to the a-priori introduced parameters are estimated in the **compute step** according to

$$\Delta \hat{\boldsymbol{x}} = (\boldsymbol{A}^T \boldsymbol{P} \boldsymbol{A})^{-1} \boldsymbol{A}^T \boldsymbol{P} \Delta \boldsymbol{y} \ . \tag{6.2}$$

Finally, the estimated parameter vector is used in the **restore step** in order to calculate the quantities of the gravity field. It may expressed as

$$\hat{\boldsymbol{x}} = \boldsymbol{x}_0 + \Delta \hat{\boldsymbol{x}} \ . \tag{6.3}$$

All known quantities which can be modeled beforehand are subtracted from the input data in the remove step. Therefore, on the one hand Global Gravity field Models (GGM), are representing the long-wavelength components of the gravity field, and on the other hand Digital Terrain Models (DTM) with their corresponding high frequent characteristic, which is well suited for the representation of mountainous regions like the Alps, mainly represent the short wavelengths. The iteratively computation of the supplements to the a-priori parameters is based on smoothed data. Therefore, the estimated gravity field quantity is representing only a residual signal. In case of the Austrian gravimetric geoid, residual geoid heights of about $\pm$ 1 m occur. By adding the output from the compute step together with long- and short wavelength components, the restore step is accomplished.

In case of Austrian geoid computation, three main data sources can be identified. First, terrestrial measurements provide the opportunity to represent the fine structures of the gravity field. Furthermore, information among all spectral bands is provided by gravity anomalies and deflections of the vertical *(Denker, 1988)*.

The second data source is the long wavelength component, which is represented by a GGM. In case of geoid computation, it covers mainly the long wavelengths up to a certain degree. A GGM of d/o 250 corresponds to a spatial resolution of about 80 km. Consequently, high resolution geoid structures will not be recovered by these models.

The third data source are high resolution DTMs. It is possible to cover highly frequent parts of the gravity field but a density assumption with respect to topographic masses is needed. Especially in Austria, where a mixture between topography and flatland prevail, a high quality DTM is essential for precise geoid computation. Another important application is the smoothing of the input data based on a topographic reduction of the gravity field signal, where a double consideration of topographic masses needs to be avoided. Therefore, a proper

combination of these different data types and sources suggests itself. Another quantity which is relevant for geoid modeling is the atmospheric effect. The impact of both atmospheric potentials on the geoid computation is rather small, but significant, and has to be considered in order to ensure a consistent RCR procedure.

6.2 Remove Step - Smooth the Gravity Field Signal

The gravity field signal has to be smoothed due to several reasons within the geoid computation process. This includes different reduction steps which are discussed in this section. The focus is on an optimum combination of different spectral components in order to establish one consistent set of observations, which can be used to compute a high quality geoid.

6.2.1 Full Vector Approach

in this research the full vector approach is developed in order to minimize linearization errors and to improve the entire geoid computation (see sec. 7.4.1). A linearization according to

$$\boldsymbol{y}_0 = f(\boldsymbol{x}_0) \ , \tag{6.4}$$

is usually applied to transform from non-linear to linear functionals. The full vector approach prevents linearization and the complete reduction, including the topographic-isostatic components and atmospheric part from the measured gravity value g can therefore written as

$$\Delta g_{red} = g - \| \nabla V^{GGM} + \delta \boldsymbol{g}^{topo} + \boldsymbol{g}^{iso}_{SH} - \delta \boldsymbol{g}^{atm} + \boldsymbol{g}^{cen} \| \ , \tag{6.5}$$

where the individual quantities are treated as vectors instead of a scalar potential representation (see also sec. 3.2). ∇V^{GGM} denotes a reference field which is subtracted from the measured gravity data. This is discussed in more detail in sec. 6.2.2. The topographic reduction is denoted as $\delta \boldsymbol{g}^{topo}$ and represents the spectral part which is not yet covered by the GGM (see sec. 6.2.3). This also holds for the residual isostatic part, denoted as $\boldsymbol{g}^{iso}_{SH}$, which is representing only the remaining short wavelength component of the isostasy. The parts representing the removal of the atmosphere has been split into interior and exterior parts. The combined part $\delta \boldsymbol{g}^{atm}$ of both atmospheric potentials has been considered in Eq. (6.5). This is due to the fact that the GGM already includes atmospheric reduction below satellite's altitude but the affecting atmospheric masses are above the measured gravity field quantities which are located on the Earth's surface. This problem is treated in more detail in sec. 6.2.4. The centrifugal acceleration for the gravity computed from the Earth rotation is denoted as $\boldsymbol{g}^{cen}$.

6.2.2 Long-Wavelength Reduction and Global Gravity Field Model

The satellite-only model GOCO05s *(Mayer-Gürr et al, 2015)*, has been utilized in this research to cover the long wavelength part of the gravity field. Currently, the GOCO05s is the latest and most accurate in a row of Gravity Observation COmbination (GOCO) models, providing high accurate information of the long wavelength available up to N_{max}= 280. This d/o corresponds to a spatial resolution of approximately 70 km. Considering the fact that the long wavelengths behave with decreasing accuracy in the higher degrees, the practical consideration of this model is limited to d/o 250 within this thesis.

In Fig. 6.1 the development of GGMs used for Austrian geoid computation is shown in terms of geoid heights. The EIGEN-GL04S1 *(Förste et al, 2006)* or *(Förste et al, 2008)* model was used for the present Austrian geoid solution in 2007. The maximum d/o of the model is limited to 150, whereas only d/o 70 was taken into account for the geoid modeling. At the moment the GOCO05s represents the state of the art model. The signal degree variances, which represent the information content of every spherical harmonic degree, are illustrated as solid line, the formal errors (error degree variances) as dashed lines (see sec. 6.3.3), which indicates an improvement of the GOCO05s in comparison to the EIGEN model.

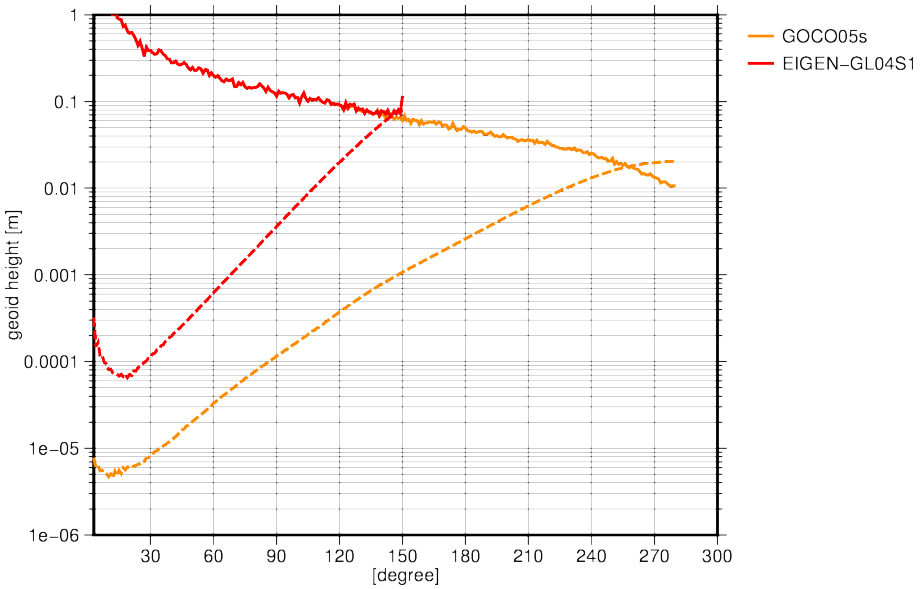

Figure 6.1: Signal degree variances of the GOCO and EIGEN models as solid lines; The formal errors of the models are illustrated as dashed lines in terms of geoid heights

Several data sources from 15 different satellites contribute to the GOCO05s. The main contributions are provided by dedicated gravity field missions. GRACE *(Tapley et al, 2004)* provides information below d/o 120, whereas GOCE *(Drinkwater et al, 2003)* mainly contributes between d/o 120-260. Beyond d/o 260 the model is driven by Kaula regularization *(Kaula, 1966)*. Moreover, the Satellite Laser Ranging (SLR) technique provides accurate information about the very long wavelengths. This technique contributes up to d/o 10, where the main

part of its contribution is attributed to d/o 2. More details related to the GOCO05s model can be found in *(Mayer-Gürr et al, 2015)*.

The spherical harmonic coefficients provided by the GOCO05s can directly be used to compute functionals of the disturbing potential such as geoid heights, where the spatial resolution depends on the chosen d/o (see sec. 3.5). In this section only an intermediate step of Eq. (6.5), representing the removal of the long wavelength components up to d/o 250 from the measured gravity, is shown in Fig. 6.2. The corresponding statistics can be found in Tab. 6.1.

At this point it has to be mentioned that for linearization issues and as a methodological development an approximated ellipsoidal height has been introduced for every gravity field observation and every DTM point in advance. The necessary geoid height is derived from the GOCO05s model up to d/o 250 according to

$$h \approx H + N^{GGM} \ . \tag{6.6}$$

Therefore, also the evaluation of the potential is related to that height. Furthermore, gravity derived from the GOCO05s model replaces the normal gravity. This has been discussed in sec. 3.5, whereas the impact of both effects is presented in sec. 7.4.1.

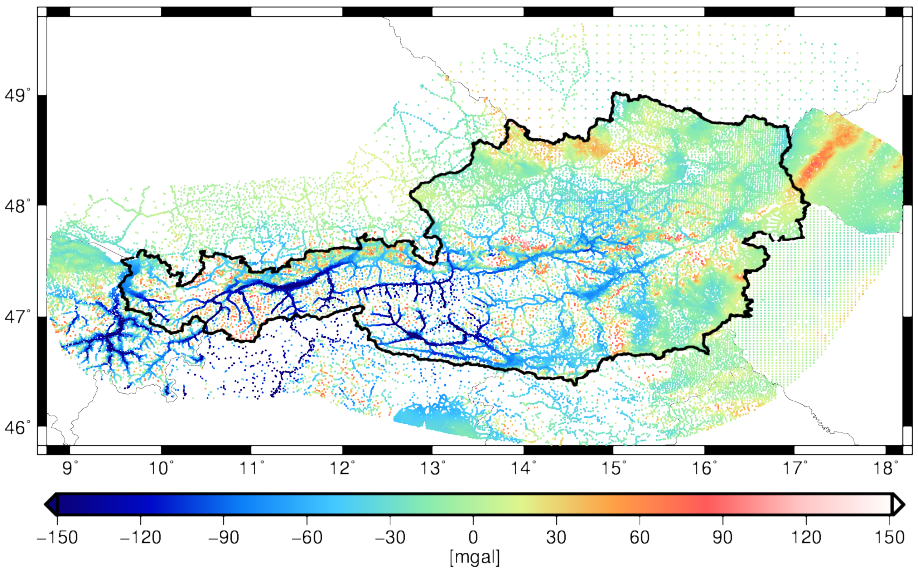

Figure 6.2: Remaining short wavelength part of gravity anomalies after long wavelength reduction up to d/o 250

Table 6.1: Statistics of long wavelength reduction of 72327 gravity observations

[mgal]	min	max	mean	rms
$g - \|\nabla V^{GGM} + \boldsymbol{g}_{cen}\|$	-231.13	143.89	-26.34	51.42

As expected, after applying a long wavelength reduction sharp structures and valleys show up in Fig. 6.2. Also a considerable mean value is remaining. This is due to the fact that

a vast amount of the gravity measurements are taken place in valleys and the mountainous regions are underrepresented. With this long wavelengths correction also the contribution from isostasy is well covered due to the fact the satellite derived GGM is representing the signal in the same spectral bandwidth.

6.2.3 Short-Wavelength Reduction and Topographic/Isostatic Model

From a spectral point of view, one can say that the entire reduction step needs to be corrected for long wavelength signals coming from the topographic reduction, as well as from the potential of the atmosphere. Parts of the topographic reduction are already included in the long wavelength GGM and this needs to be considered in the RCR procedure in order to avoid a double consideration of topographic masses. Therefore, only short wavelength parts of topography are needed.

Topographic Model

To be able to exploit the full available information from GGMs and to ensure a proper treatment of the topographic masses within the RCR technique, a spectral separation approach in long- and short wavelength parts is performed. For the remove as well as the restore step, the long wavelength components should only be represented by the information derived from the GGM. The short wavelength part beyond a certain d/o of the series expansion is therefore derived from topography, which ensures that the spectral component of topography which is already covered by the GGM is not taken into account twice. In mathematical notation the complete gravitational potential is therefore given according to

$$V(P) = \sum_{n=0}^{N} \underbrace{a_{nm}^{GGM} Y_{nm}(P)}_{long} + \sum_{n=N+1}^{\infty} \underbrace{a_{nm}^{topo} Y_{nm}(P)}_{short} , \tag{6.7}$$

where Y_{nm} are the spherical harmonics and the a_{nm} representing either short- or long wavelength components (see also sec. 3.1). To perform the spectral separation the gravitational potential of the topography has to be known and can be computed by e.g. prism representation as will be shown later in this section. For an arbitrary point P, this topographic gravitational potential in the spectral domain may be expressed as

$$V^{topo}(P) = \sum_{n=0}^{N} V_n^{topo}(P) + \sum_{n=N+1}^{\infty} V_n^{topo}(P) , \tag{6.8}$$

where the high frequent part of the topography, which is needed in addition to the part covered by the GGM, is given by spectral separation of Eq. (6.8). It follows

$$\sum_{n=N+1}^{\infty} V_n^{topo}(P) = V^{topo}(P) - \sum_{n=0}^{N} V_n^{topo}(P) \ , \tag{6.9}$$

where in turn $\sum_{n=0}^{N} V_n^{topo}(P)$ denotes the gravitational potential of the topography coming from the spherical harmonic expansion of the DTM up to d/o N, which is given according to Eq. (3.26). A proper choice of N is discussed in sec. 6.3.3. By means of introducing the topographic potential coefficients into the RCR procedure, a rigorous spectral separation between the different spectral bands is possible. The set of coefficients derived from the topography can be used for the series expansion of different functionals of the disturbing potential which is shown in, for example *(Mayer-Gürr and Pock, 2015)*.

The topography and its gravitational potential has to be removed to fulfill the Laplace equation (see sec. 3.2). Furthermore, the gravity field signal is smoothed by removing its high frequent topographic part. This is done by a topographic reduction, where the masses are treated depending on their spatial distance from the gravity station. In the vicinity of the gravity station, the gravitational potential of the topography is treated with the prism formula *(Mader, 1951)*. Beyond a certain distance, the topography is treated as a 2D integral with radial integration and another distinction is done for the distant zones, where the topography is assumed to be a point mass. This is due to a decreasing impact of the topographic masses with increasing distance. In summary, the topographic potential is approximated as

- $r < 50$ km prism formula,
- r= 51-100 km 2D integral with radial integration,
- $r > 100$ km point masses.

A visual interpretation of the different topographic treatments is shown in Fig. 6.3. It has to be noted that the entire topography is considered without a limiting radius for remove and restore steps. A common approach is to assign a constant density value to every individual mass column. To be more realistic, this information can also be derived from density models as discussed in sec. 4.4, where the constant standard value may be replaced.

In general, for the computation of the potential and its first derivatives, the topographic masses are separated into single volume elements. The gravitational effect is therefore computed over the sum of these single elements, where the type of the shape approximation method depends on the distance between the gravity station and the integration point of the DTM. Due to the fact that the fine structure of a field generating body is attenuated with increasing distance from the station, a simplification from prism representation to a 2D integral with radial integration and point masses is permitted. This simplification decreases computational efforts.

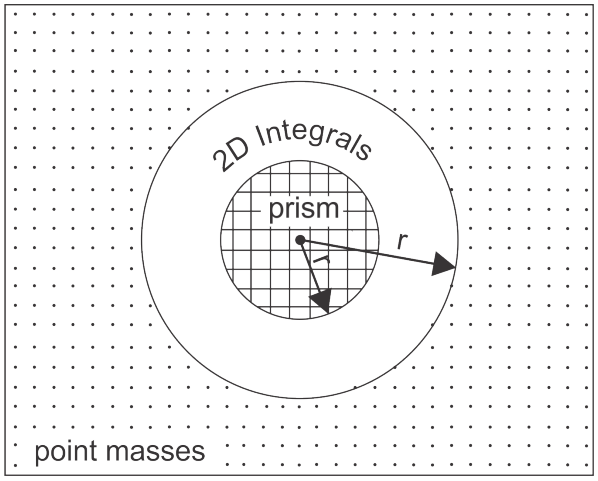

Figure 6.3: Different approximation approaches of the topography depending on the distance between the gravity station and the DTM point

Prism Representation

For the discretization of the topography, a DTM is used to enable the computation of the gravitational attraction. In case of representation as a prism shaped body, the gravitational potential in the vicinity of the gravity station for an arbitrary computation point P is given according to *(Mader, 1951)* or *(Nagy, 1966)*

$$V(x,y,z) = G\rho\Big[- \bar{y}\bar{z}\log(\bar{x}+l) - \bar{x}\bar{y}\log(\bar{z}+l) - \bar{x}\bar{z}\log(\bar{y}+l) + \frac{\bar{x}^2}{2}\arctan\left(\frac{\bar{y}\bar{z}}{\bar{x}l}\right) + \frac{\bar{y}^2}{2}\arctan\left(\frac{\bar{x}\bar{z}}{\bar{y}l}\right) + \frac{\bar{z}^2}{2}\arctan\left(\frac{\bar{y}\bar{x}}{\bar{z}l}\right)\Big] \Bigg|_{(\bar{x}=x-x_1)(\bar{y}=y-y_1)(\bar{z}=z-z_1)}^{(x-x_2)(y-y_2)(z-z_2)}, \quad (6.10)$$

where for a local Cartesian coordinate system, which is defined at the edges of the prism according to Fig. 6.4, the distance $l = \sqrt{\bar{x}^2 + \bar{y}^2 + \bar{z}^2}$ is given as the difference between computation and integration point. The three components of the gravity vector, which are needed for the full vector approach (see sec. 6.2.1), are derived from partial derivatives of the potential as follows

$$\boldsymbol{g}_x = \frac{\partial V(P)}{\partial x} = G\rho\left[\bar{y}\log(\bar{z}+l) + \bar{z}\log(\bar{y}+l) - \bar{x}\arctan\left(\frac{\bar{y}\bar{z}}{\bar{x}l}\right)\right] \Bigg|_{(\bar{x}=x-x_1)(\bar{y}=y-y_1)(\bar{z}=z-z_1)}^{(x-x_2)(y-y_2)(z-z_2)},$$

$$\boldsymbol{g}_y = \frac{\partial V(P)}{\partial y} = G\rho \left[\bar{z} \log(\bar{x} + l) + \bar{x} \log(\bar{z} + l) - \bar{y} \arctan\left(\frac{\bar{x}\bar{z}}{\bar{y}l}\right) \right]_{\substack{(\bar{x}=x-x_1)(\bar{y}=y-y_1)(\bar{z}=z-z_1) \\ (x-x_2)(y-y_2)(z-z_2)}},$$

$$\boldsymbol{g}_z = \frac{\partial V(P)}{\partial z} = G\rho \left[\bar{y} \log(\bar{x} + l) + \bar{x} \log(\bar{y} + l) - \bar{z} \arctan\left(\frac{\bar{y}\bar{x}}{\bar{z}l}\right) \right]_{\substack{(\bar{x}=x-x_1)(\bar{y}=y-y_1)(\bar{z}=z-z_1) \\ (x-x_2)(y-y_2)(z-z_2)}}. \tag{6.11}$$

The geometric situation for an individual prism is shown in Fig. 6.4.

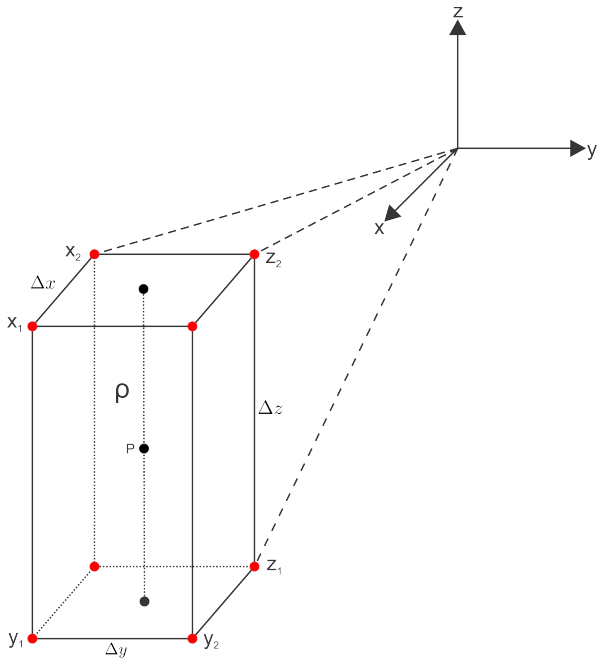

Figure 6.4: Geometric situation for a single prism with density ρ

As the gravity vector is needed in a global equatorial system, an ordinary coordinate transformation has to be considered. The corresponding matrices can be found in e.g. *(Kuhn, 2000)*. The spatial arrangement of the prism is shown on the right hand side of Fig. 6.5, whereas the evaluation and summation of the prism formula over every single mass column of the DTM gives the entire gravitational effect within a defined radius r. Due to decreasing gravitational influence with increasing distance and due to computational efforts, the effect beyond this is approximated with an approach based on tesseroids, as described in the following.

2D Integral and Radial Analytical Integration

The solution of the potential of a tesseroid shaped body (see Fig. 6.5) leads to elliptical integrals which are not directly solvable in an analytical sense *(Wild-Pfeiffer, 2007)*. Nevertheless, there are several approaches existing to solve, for example, a numerical solution such as 2D

integrals with radial integration *(Heck and Seitz, 2003)*. In this case, the originally given 3D volume element is split into a one-dimensional analytic integral in radial direction and one two-dimensional integral for the area element as described in *(Wild-Pfeiffer, 2007)*.

The tesseroid can be approximated by a prism shaped body, if the mass and the vertical extension are the same *(Hirt and Kuhn, 2014)*. In this case, the spatial orientation of both, the prism and the tesseroid coincide, leading to the same intersection points on the bottom, midpoint and top of the body. Nevertheless, the shapes are different and so the corner points differ as shown on the right hand side of Fig. 6.5. The relation to the prism is given according to *(Heck and Seitz, 2007)*

$$\Delta x = r_0 \Delta\varphi, \quad \Delta y = r_0 \cos\varphi_0 \Delta\lambda, \quad \Delta z = \Delta r \ , \tag{6.12}$$

where the Δx, Δy and Δz values refer to the prism geometry as shown in Fig. 6.4. $\Delta\varphi$, $\Delta\lambda$ as well as Δr belong to the tesseroid. Furthermore, φ_0 and r_0 are related to the midpoint of the body.

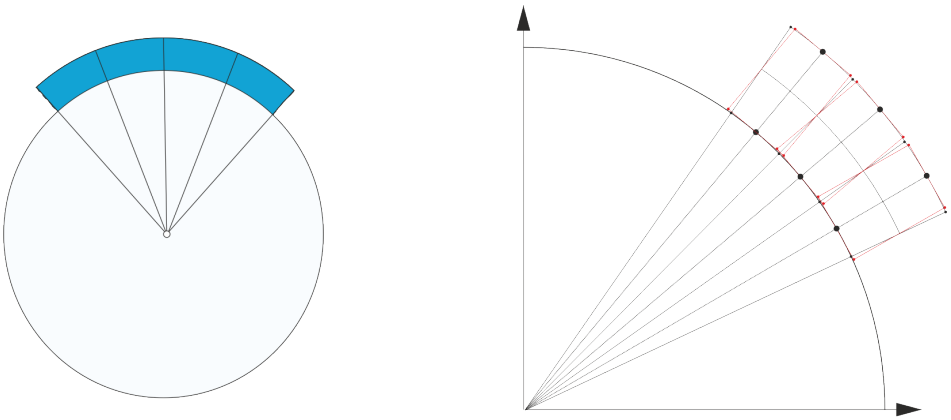

Figure 6.5: Simple tesseroid representation (left) and approximation by prism (right)

Following the notation of *(Wild-Pfeiffer, 2007, p.21)*, the corresponding potential reads

$$V(\lambda,\varphi,r) = \frac{G\rho}{2} \iint_{\sigma} K_V \, d\sigma,$$

$$K_V = \frac{1}{2}\left[r_2 l_2 - r_1 l_1 + 3r\cos\Psi(l_2 - l_1) + r^2(3\cos^2\Psi - 1)\ln\left(\frac{l_2 + r_2 - r\cos\Psi}{l_1 + r_1 - r\cos\Psi}\right)\right] \ , \tag{6.13}$$

where Ψ denotes a spatial distance, r is the radius and r_1 and r_2 are the upper and lower integration bounds. The distances to the upper and lower points are given as

$$l_1 = \sqrt{r^2 + r_1^2 - 2rr_1\cos\Psi} \qquad l_2 = \sqrt{r^2 + r_2^2 - 2rr_2\cos\Psi}$$

According for the chain rule, the three components of the gravity vector as partial derivatives of the corresponding potential read

$$\boldsymbol{g}_x = \left\{ -2r \ln \left(\frac{l_2 + r_2 - r\cos\Psi}{l_1 + r_1 - r\cos\Psi} \right) \frac{x}{r} + \left[r_2 + 3r\cos\Psi + \frac{r^2(3\cos^2\Psi - 1)}{l_1 + r_1 - r\cos\Psi} \right] \frac{x}{l_2} + \left[-r_1 - 3r\cos\Psi - \frac{3\cos^2\Psi - 1}{l_2 + r_2 - r\cos\Psi} \right] \frac{x}{l_1} \right\} \frac{1}{2} \cos\varphi_0 d\lambda d\phi \ ,$$

$$\boldsymbol{g}_y = \left\{ -2r \ln \left(\frac{l_2 + r_2 - r\cos\Psi}{l_1 + r_1 - r\cos\Psi} \right) \frac{y}{r} + \left[r_2 + 3r\cos\Psi + \frac{r^2(3\cos^2\Psi - 1)}{l_1 + r_1 - r\cos\Psi} \right] \frac{y}{l_2} + \left[-r_1 - 3r\cos\Psi - \frac{3\cos^2\Psi - 1}{l_2 + r_2 - r\cos\Psi} \right] \frac{y}{l_1} \right\} \frac{1}{2} \cos\varphi_0 d\lambda d\phi \ ,$$

$$\boldsymbol{g}_z = \left\{ -2r \ln \left(\frac{l_2 + r_2 - r\cos\Psi}{l_1 + r_1 - r\cos\Psi} \right) \frac{z}{r} + \left[r_2 + 3r\cos\Psi + \frac{r^2(3\cos^2\Psi - 1)}{l_1 + r_1 - r\cos\Psi} \right] \frac{z}{l_2} + \left[-r_1 - 3r\cos\Psi - \frac{3\cos^2\Psi - 1}{l_2 + r_2 - r\cos\Psi} \right] \frac{z}{l_1} + \left[3(l_2 - l_1) + 6r\cos\Psi \ln \left(\frac{l_2 + r_2 - r\cos\Psi}{l_1 + r_1 - r\cos\Psi} \right) - \frac{r^2(3\cos^2\Psi - 1)}{l_2 + r_2 - r\cos\Psi} + \frac{r^2(3\cos^2\Psi - 1)}{l_1 + r_1 - r\cos\Psi} \right] \right\} \frac{1}{2} \cos\varphi_0 d\lambda d\phi \ . \quad (6.14)$$

Point Masses

The potential of a prism can be simplified. Due to the fact that with increasing distance the impact of the masses on the gravitational potential diminishes, a Taylor series expansion of the integral kernel with its origin evaluated at the geometrical center of the mass leads to *(Wild-Pfeiffer, 2007, p.28)*

$$V(x, y, z) = G\rho \frac{\Delta x \Delta y \Delta z}{l} \ . \quad (6.15)$$

The distance between the geometrical center of the mass and the computation point is denoted as l and the geometry of the prism is covered by Δx, Δy and Δz. The density is denoted as ρ. The gravitational attraction of a point mass vector is given according to

$$\begin{aligned} \boldsymbol{g}_x &= \frac{\partial V(P)}{\partial x} = G\rho\Delta x\Delta y\Delta z \ \frac{\bar{x}}{l^3} \ , \\ \boldsymbol{g}_y &= \frac{\partial V(P)}{\partial y} = G\rho\Delta x\Delta y\Delta z \ \frac{\bar{y}}{l^3} \ , \\ \boldsymbol{g}_z &= \frac{\partial V(P)}{\partial z} = G\rho\Delta x\Delta y\Delta z \ \frac{\bar{z}}{l^3} \ , \end{aligned} \quad (6.16)$$

where $\bar{x}$, $\bar{y}$ and $\bar{z}$ denote the corresponding coordinate difference between the computation and integration points. Finally, for all shape representations the corresponding gravity vectors are found where the general information is provided by *(Wild-Pfeiffer, 2007)*.

Within the RCR procedure, long- and short wavelength parts of the gravity field signal have to be treated. In order to avoid a spectral overlap of these parts, the circumstance that a long wavelength topographic and also the isostatic part are already considered in the highly accurate GGMs has to be taken into account. In the following, only the topographic part is treated in more detail because the isostatic part can be treated analogously.

The combined topographic part of Eq. (6.5), is visualized in Fig. 6.6 and the corresponding results can be found in Tab. 6.2. It is defined as

$$\delta \boldsymbol{g}^{topo} = \boldsymbol{g}^{topo} - \boldsymbol{g}^{topo}_{SH} \ , \tag{6.17}$$

where $\boldsymbol{g}^{topo}$ denotes the topographic reduction and $\boldsymbol{g}^{topo}_{SH}$ the corresponding representation of the DTM masses in terms of spherical harmonics up to d/o 250. Due to a consistent treatment of the masses, only short wavelengths are remaining, which are now used to smooth the gravity field signal by means of subtracting this effect. Corresponding results can be found in sec. 7.1.

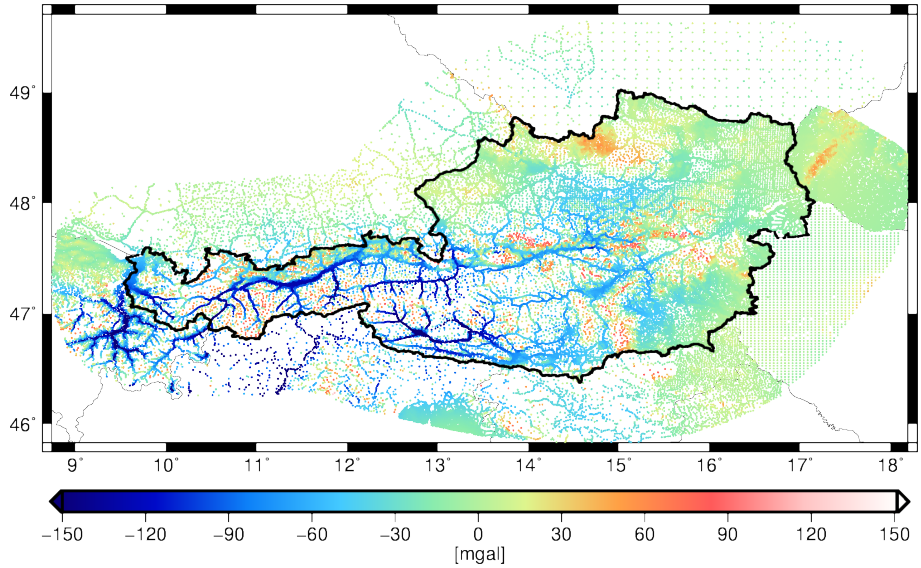

Figure 6.6: Topographic part beyond d/o 250

Table 6.2: Statistics of the short wavelength part of reduction based on 72327 gravity observations

[mgal]	min	max	mean	rms
$\|\delta \boldsymbol{g}^{topo}\|$	-228.92	129.89	-25.49	49.21

Isostatic Model

In general, the isostasy represents the hydrostatic equilibrium of the Earth's crust with a kind of mass deficit in mountainous regions and a mass surplus in flatland. This assumption needs to be modeled. According to *G.B. Airy*, the idea is to model the isostasy like an iceberg floating on the water. The more the mass protrudes from the water, the deeper it sinks, whereas in reality, the topography is floating on the Earth's mantle. The standard Airy-Heiskanen isostasy model (see Fig. 6.7) is by default assumed with a normal crust thickness of T=-30 km and a constant density contrast $\Delta\rho = \rho_m - \rho_c$ between the mantle and the crust of 600 kg/m^3.

The approach for geoid computation, which is being pursued in this thesis, considers the long wavelengths effect of isostasy as already covered by a GGM. This is valid if the spherical harmonic expansion is carried out to a higher d/o, and therefore the model covers the isostatic effect. Thus, only effects based on the series truncation beyond the chosen degree of the GGM have to be considered in the computation.

The density contrast used for this research is based on investigations to find a tailored value for the Austrian region made by *(Kühtreiber, 1998a)* and *(Rieser, 2015)*. They found 350 kg/m^3 to be suitable, where this regional value has been used for the computation of a set of isostatic spherical harmonics up to d/o 500. The corresponding spherical harmonic representation of the isostasy can be found in sec. 3.3.1, where a density contrast $\Delta\rho$ is taken into account instead of the density ρ. This set of coefficients should represent only the short wavelength component of the isostatic signal, which is actually of long wavelengths characteristic. At this point it must be noted that the entire isostatic concept is based on several assumptions and by means of applying this concept in practical geoid computation, a significant level of uncertainty is imported into the estimation process.

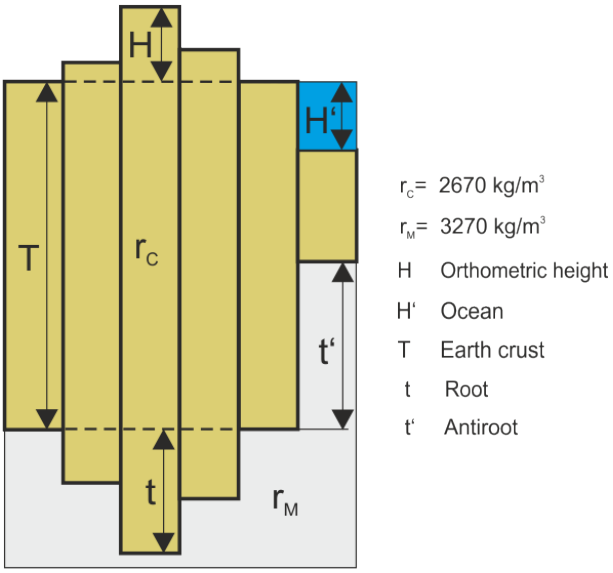

Figure 6.7: Standard Airy-Heiskanen model

The fundamental relationship between the values describing the equilibrium condition is given according to *(Hofmann-Wellenhof and Moritz, 2006)*

$$t\Delta\rho = H\rho_c \ , \tag{6.18}$$

the total thickness of the Earth's crust is assumed to be

$$T + t + H \ , \tag{6.19}$$

where t is the root and H the orthometric height. For the oceans the following relationship is valid

$$t\Delta\rho = H'(\rho_c - \rho_w) \ , \tag{6.20}$$

with $\rho_w = 1027\ kg/m^3$, which represents the water density and H' is representing the ocean depth. The corresponding crustal thickness under the ocean is then given as

$$T - H' - t' \ . \tag{6.21}$$

where t' is the anti-root which belongs to the ocean. Furthermore, all isostatic variables are explained in Fig. 6.7. The influence of the isostasy concept on the entire geoid computation has been investigated and results can be found in sec. 7.4.7. It turns out that this part strongly depends on the chosen d/o of the GGM, which covers the same long wavelengths range of the spectrum and contains in principle the same information. Therefore, a decreasing influence of the isostasy with increasing d/o of the GGM is expected.

In Fig. 6.8 the residual isostatic part is shown. As can directly be observed, a remaining long wavelength structure is not visible, only short wavelength parts remain, where the computation is based on a constant density contrast of $\Delta\rho = 350\ kg/m^3$. The corresponding statistics is provided in Tab. 6.3. The remaining isostatic effect is small and has to be restored in terms of geoid heights within a consistent RCR procedure.

Table 6.3: Statistics of remaining isostatic part of 72327 gravity observations

[mgal]	min	max	mean	rms
$\boldsymbol{g}_{SH}^{iso}$ d/o 251 $\rightarrow$ 500	-7.13	8.88	0.07	1.94

For the sake of completeness, the Pratt-Hayford and the Vening-Meinesz models have to be mentioned. Both models also deal with isostasy but in different ways. The Pratt-Hayford model is based on a constant level of compensation of 100 km, but allows for different density

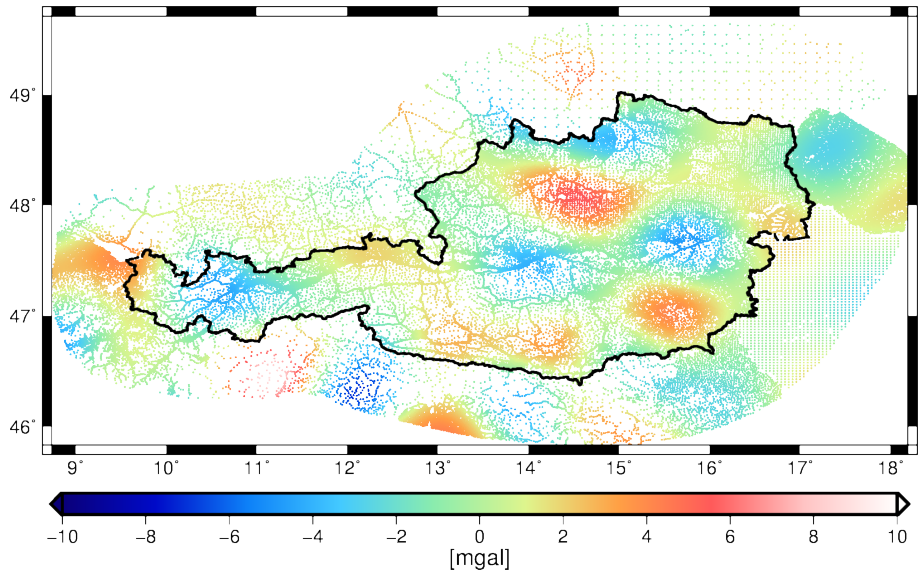

Figure 6.8: Influence of the isostatic part on gravity observations d/o 251 → 500

assumptions for each individual surface mass column, which compensates mass surpluses or deficits in a local region. Due to the varying density values all mass columns have equal mass. This model is suitable especially for flatland.

The Vening-Meinesz approach can be seen as an refinement of Airy-Heiskanen, but with a more regional compensation of the mass loading in the lithosphere. This gives a more realistic geophysical meaning but is very complex in comparison to the Airy-Heiskanen model. A detailed description of the different models can be found in, for example, *(Hofmann-Wellenhof and Moritz, 2006)*, or especially the Vening-Meinesz approach is treated in *(Abd-Elmotaal, 1995)*.

6.2.4 Atmospheric Reduction and Atmospheric Density Model

The atmospheric density decreases with increasing height. Therefore, the ITSG atmospheric density model [see *(Rieser, 2015)* or sec. 3.3.2] provides the framework for the atmospheric corrections, which are considered for the exterior as well as for the interior potential within the RCR approach. As shown by *(Rieser, 2015)*, the combined effect of these two components

$$\delta \boldsymbol{g}^{atm} = \boldsymbol{g}_{SH}^{atm,e} - \boldsymbol{g}_{SH}^{atm,i} \ , \tag{6.22}$$

is rather small and clearly < 1 mgal but needs to be considered for the geoid determination. In order to be consistent in the RCR process, the exterior atmospheric potential effect $\boldsymbol{g}_{SH}^{atm,e}$ is added back to the GGM model because it is already subtracted from this model. The interior potential $\boldsymbol{g}_{SH}^{atm,i}$ is representing the gravitational influence of each mass column located above the measured gravity measured on Earth surface and has to be removed in order to obtain

atmosphere free observations. On the one hand the attracting masses are assumed to be below (at satellites altitude) and on the other hand above the gravity measurements. Hence, it must be distinguished between inner and exterior potentials.

The atmospheric potential effect is of long wavelength behavior and several investigations concerning a DTM enhancement and a proper expansion of the potential in terms of spherical harmonics have been carried out. It turns out that the differences between an European DTM representation (see sec. 4.3.1) and a global DTM coverage provided by the GTOPO model (see sec. 4.3.2) are rather small and can be neglected. To account for the exterior atmospheric potential, which is already included in the GGM, the potential series expansion was chosen accordingly to the series expansion of the GGM. For the interior potential the chosen d/o can exceed the maximum degree of the GGM. Nevertheless, to be consistent the same d/o is chosen.

In Fig. 6.9 the combined effect of the atmosphere, based on the DTM covering central Europe, is shown for the gravity data. The main effect consists of a mean value of 0.63 mgal, which has been subtracted from the illustration in order to expose the remaining variations. As expected, it is the smallest quantity within the entire RCR procedure, representing a range starting from 0.48 mgal in mountainous regions up to 0.70 mgal in flatland. This behavior is inverse in comparison to the topographic structures, because the masses above the gravity measurements are smaller in areas which are located in alpine regions. For the restore step, the geoid heights caused by the atmospheric potentials are shown in sec. 6.4.3.

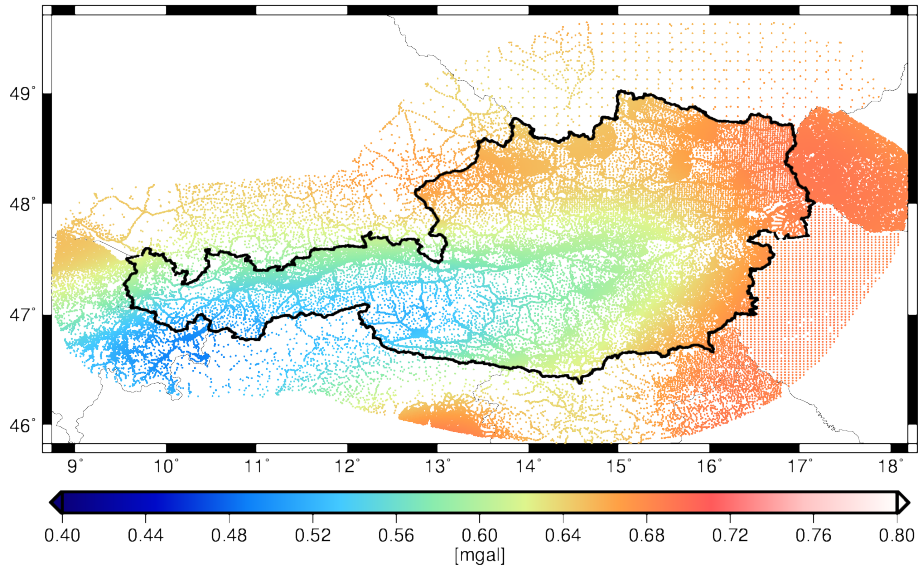

Figure 6.9: Combined atmospheric signal in terms of gravity anomalies

6.3 Compute Step - Estimate Gravity Field Quantities

Within the RCR procedure the compute step is utilized to estimate a set of parameters for different functionals of the gravity field. The residual gravity field signal is used as input for the computation process (see sec. 6.2). The estimation of the unknown parameters is mathematically determined by a least squares approach which is discussed in sec. 5.1. The parametrization is based on Radial Basis Functions (RBF) parameters (see sec. 6.3.1), where the Variance Component Estimation (VCE) method (see sec. 5.2.2) provides the relative weighting of the different observation groups (see sec. 5.2.3). The shape of the RBFs are derived from the formal errors of a GGM up to a certain d/o, and beyond by Kaula's rule of thumb (see sec. 6.3.3). The finally estimated solution vector of RBF scaling coefficients is suitable to represent every gravity field quantity.

6.3.1 Radial Basis Function Parametrization

RBFs are characterized by the spherical distance between two points on the sphere. The basis functions denoted as $\phi(\boldsymbol{r})$ are radial symmetric and can therefore be expressed as a sum of Legendre polynomials. According to *(Eicker, 2008)* and *(Bentel et al, 2013)* it follows

$$\phi(\boldsymbol{r}) = \frac{GM}{R}\sum_{n=2}^{\infty}\left(\frac{R}{r}\right)^{n+1}\sqrt{2n+1}\cdot k_n P_n(\boldsymbol{r}\cdot\boldsymbol{r}_i) = \frac{GM}{R}\sum_{n=2}^{\infty}\left(\frac{R}{r}\right)^{n+1} k_n \sum_{m=-m}^{n} Y_{nm}(\boldsymbol{r})Y_{nm}(\boldsymbol{r}_i)\ , \tag{6.23}$$

where $\boldsymbol{r}$ indicates the evaluation position and $\boldsymbol{r}_i$ the spatial localization of the RBF. The coefficients k_n are responsible for the shape of the basis function. In general, the functionals of the disturbing potential (see sec. 3.5) can be expressed as the sum of a series expansion evaluated at a certain position $\boldsymbol{r}$. It follows

$$T(\boldsymbol{r}) = \sum_{i=1}^{I} a_i\ \phi_i(\boldsymbol{r})\ , \tag{6.24}$$

where this linear combination includes the unknown RBF weights a_i to determine. The disturbing potential is a harmonic function. Hence, the RBFs are also characterized as harmonic *(Eicker, 2008)*. Further mathematical details concerning the harmonic kernel functions can be found in, for example *(Freeden and Törnig, 1981)* or *(Freeden, 1999)*.

An example set of estimated unitless scaling coefficients a_i and their corresponding spatial distribution used in this thesis is shown in Fig. 6.10. This corresponds to the finally chosen RBF locations as described in sec. 6.3.4.

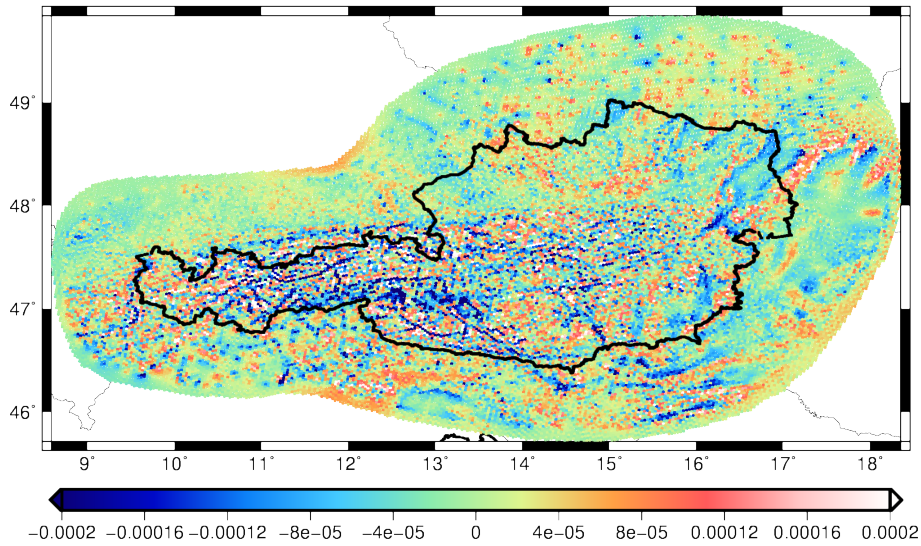

Figure 6.10: Set of estimated unitless RBF scaling coefficients

6.3.2 Radial Basis Function Referred to Functionals of the Gravity Field

Applying the RBF approach for regional geoid modeling, which is originally based on *(Eicker, 2008)*, to the gravity field signal, it may be expressed as a linear combination of the radial symmetric basis functions with the scaling coefficients as given in Eq. (6.24). The corresponding basis function $\phi(\boldsymbol{r})$ for gravity anomalies can in turn be expressed by a sum of Legendre polynomials according to

$$\phi(\boldsymbol{r}) = \frac{GM}{R} \sum_{n=2}^{\infty} \left(\frac{R}{r}\right)^{n+1} k_n \sum_{m=-n}^{n} \left(\frac{n-1}{R}\right) Y_{nm}(\boldsymbol{r}) Y_{nm}(\boldsymbol{r}_i) \ . \tag{6.25}$$

In case of gravity disturbances, the basis function changes to

$$\phi(\boldsymbol{r}) = \frac{GM}{R} \sum_{n=2}^{\infty} \left(\frac{R}{r}\right)^{n+1} k_n \sum_{m=-n}^{n} \left(\frac{n+1}{R}\right) Y_{nm}(\boldsymbol{r}) Y_{nm}(\boldsymbol{r}_i) \ . \tag{6.26}$$

For the gravity vector representation, partial derivatives of the basis functions are required

$$\boldsymbol{g}(\boldsymbol{r}) = \nabla T(\boldsymbol{r}) = \sum_{i=1}^{I} a_i \ \nabla \phi_i(\boldsymbol{r}) \ , \tag{6.27}$$

where the derivatives of the basis functions with respect to Cartesian coordinates can be found by applying the chain rule. According to *(Eicker, 2008)* it follows

$$\nabla\phi = \begin{pmatrix} \frac{\partial\phi}{\partial x} \\ \frac{\partial\phi}{\partial y} \\ \frac{\partial\phi}{\partial z} \end{pmatrix} = \begin{pmatrix} \frac{\partial\phi}{\partial r}\frac{\partial r}{\partial x} + \frac{\partial\phi}{\partial t}\frac{\partial t}{\partial x} \\ \frac{\partial\phi}{\partial r}\frac{\partial r}{\partial y} + \frac{\partial\phi}{\partial t}\frac{\partial t}{\partial y} \\ \frac{\partial\phi}{\partial r}\frac{\partial r}{\partial z} + \frac{\partial\phi}{\partial t}\frac{\partial t}{\partial z} \end{pmatrix} . \tag{6.28}$$

The single derivative with respect to r and t are given for the exterior potential. Hence, the following derivatives can be built

$$\frac{\partial\phi}{\partial r} = \frac{-(n+1)R^{n+1}}{r^{n+2}} k_n P_n(t) , \tag{6.29}$$

$$\frac{\partial\phi}{\partial t} = \left(\frac{R}{r}\right)^{n+1} k_n \frac{d\ P_n(t)}{dt} , \tag{6.30}$$

$$\frac{\partial r}{\partial x} = \frac{x}{r} , \qquad \frac{\partial r}{\partial y} = \frac{y}{r} , \qquad \frac{\partial r}{\partial z} = \frac{z}{z} , \tag{6.31}$$

$$\frac{\partial t}{\partial x} = \frac{x_i}{rR} - \frac{tx}{r^2} , \qquad \frac{\partial t}{\partial y} = \frac{y_i}{rR} - \frac{ty}{r^2} , \qquad \frac{\partial t}{\partial z} = \frac{z_i}{rR} - \frac{tz}{r^2} , \tag{6.32}$$

where $t = \boldsymbol{r} \cdot \boldsymbol{r}_i$, which indicates the affiliation to the coordinates of the two points involved. If any other coordinate system is needed the corresponding transformations can be found in e.g. *(Hofmann-Wellenhof and Moritz, 2006)*.

The RBF solution may be transformed into a set of spherical harmonics which leads to the same result *(Wittwer, 2009)*. The main difference is that spherical harmonics are not localized in space, whereas the RBF have an ideal space localizing character *(Freeden, 1999)*. Furthermore, RBFs are strongly dependent on the spherical distance of the data points and the corresponding spatial location of the basis functions.

Typically, the shape of the basis function has its maximum value at the center and shows an oscillating behavior with increasing distance from the center. If the basis function is not defined as a band-limited function, it never becomes zero. With increasing degree of expansion, the basis function becomes narrower. From a spectral point of view, this means that wider basis functions are more suitable for the representation of the lower frequencies, whereas the high frequencies can be well represented with narrow basis functions *(Wittwer, 2009)*. In order to recover finer structures of the gravity field, a higher degree of expansion is needed. An example connected to two important gravity field quantities is shown in Fig. 6.11. The normalized kernel basis functions for gravity anomalies as well as for the geoid heights, are illustrated therein. For the representation of the gravity field signal in terms of RBFs, the scaling coefficients a_i are the desired quantities to be determined within a least squares adjustment, where i denotes the number of unknown weights.

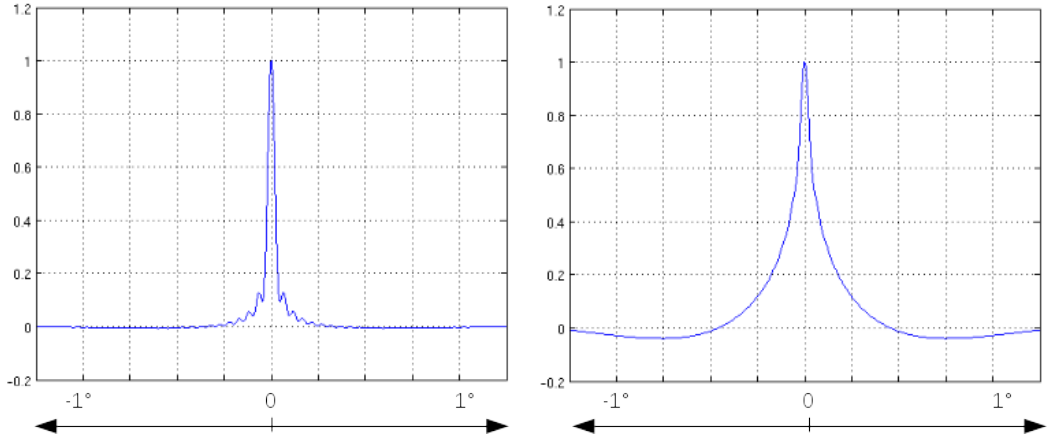

Figure 6.11: Different normalized RBF kernels; gravity anomaly (left) and geoid height (right)

6.3.3 Shape Giving Aspects of Radial Basis Functions

A possible way to define the shape of the basis functions is the so-called spline kernel, where the frequency response of the Earth's gravity field is taken into account [see *(Eicker, 2008)* or *(Naeimi, 2013)*]. In this case the degree variances of a GGM are representing these responses and can be computed from spherical harmonic coefficients according to

$$\sigma_n^2 = \sum_{m=0}^{n} \bar{c}_{nm}^2 + \bar{s}_{nm}^2 \ . \tag{6.33}$$

For this research the approach of *(Eicker, 2008)* is applied for the estimation of the scaling RBF coefficients. Following this method, the RBFs are defined according to Eq. (6.23) and the coefficients k_n are given as

$$k_n = \frac{\sigma_n}{\sqrt{2n+1}} \ . \tag{6.34}$$

The k_n coefficients are important because they control the shape of the basis functions and furthermore it is a degree dependent weighting of the Legendre polynomials.

The error degree variances σ_n^2, are provided by an a-priori known GGM model up to a certain d/o. Considering this information means that the accuracy information of the GGM is taken into account within the computation process and the solution is regularized towards this prior information (see sec. 5.2). Beyond the maximum available d/o of the GGM, Kaula's rule of thumb *(Kaula, 1966)* approximates the degree variances according to

$$\sigma_n \approx \sqrt{(2n+1)\frac{10^{-10}}{n^4}} \ , \tag{6.35}$$

in terms of unitless coefficients. This enables the opportunity to approximate degree variances if the maximum d/o provided by the GGM needs to be exceeded.

Within this thesis error degree variances of the GOCO05s model up to d/o 250 have been considered. Beyond d/o 250 up to d/o 9000 the coefficients are padded by Kaula's rule [Eq. (6.35)]. The GOCO05s itself provides error degree variances up to d/o 280. The choice of this d/o considers the fact that the GGM does not provide the full spectral power in the higher degrees, but provides a high accuracy in the long wavelengths. This combination of the degree- and error degree variances for the RBF shape representing k_n coefficients are shown in terms of geoid heights in Fig. 6.12.

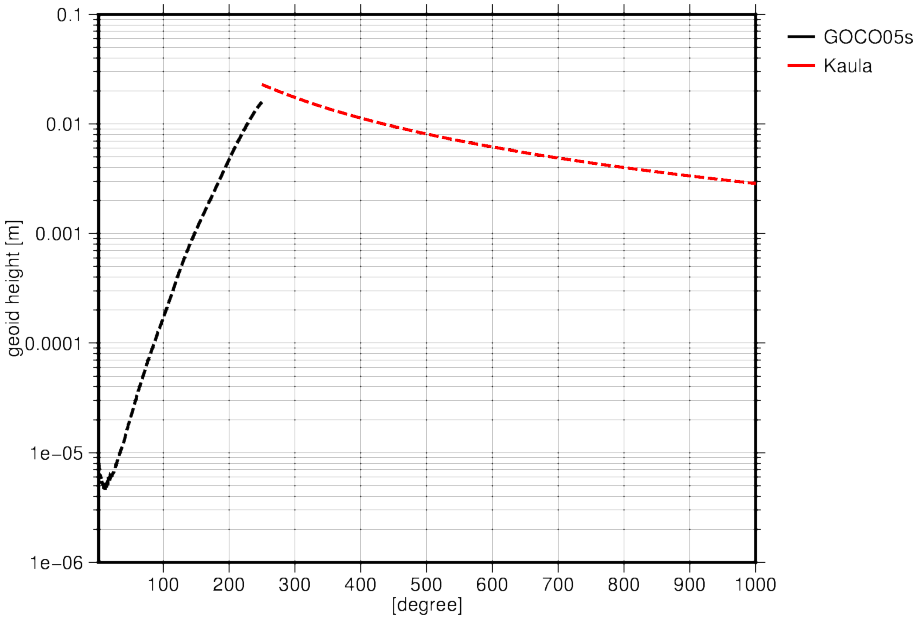

Figure 6.12: Transition between the GOCO05s error degree variances and the full signal of the high frequencies using Kaula's rule starting from d/o 251 → 9000

Kaula's rule is used to compute the power spectrum beyond d/o 250. The approximation of degree variances with Kaula's rule is defined on a global scale. For the purpose of regional gravity field modeling, a slight modification affecting the decay behavior of Kaula's approximated degree variance function has been applied and investigated. This has been done in order to prove if the original Kaula definition is also valid on a regional scale (for Austrian geoid computation) and to investigate if a changed shape of the curve is more appropriate to represent the RBF shape. The degree variances which are responsible for the RBF shape are shown in Fig. 6.13, up to d/o 1000, whereas they are computed up to d/o 9000.

The decay behavior is attributed to a different meaning for the computation. As can be seen in Fig. 6.13, one curve denoted as *Kaula 1* is steeper and the curve denoted as *Kaula 2* runs shallower compared to the original Kaula definition, which is given as dashed red line. This corresponds directly to a more optimistic or more pessimistic assumption of the accuracy of the approximated degree amplitudes in the higher degrees. The achieved results for different RBF shapes can be found in sec. 7.4.5.

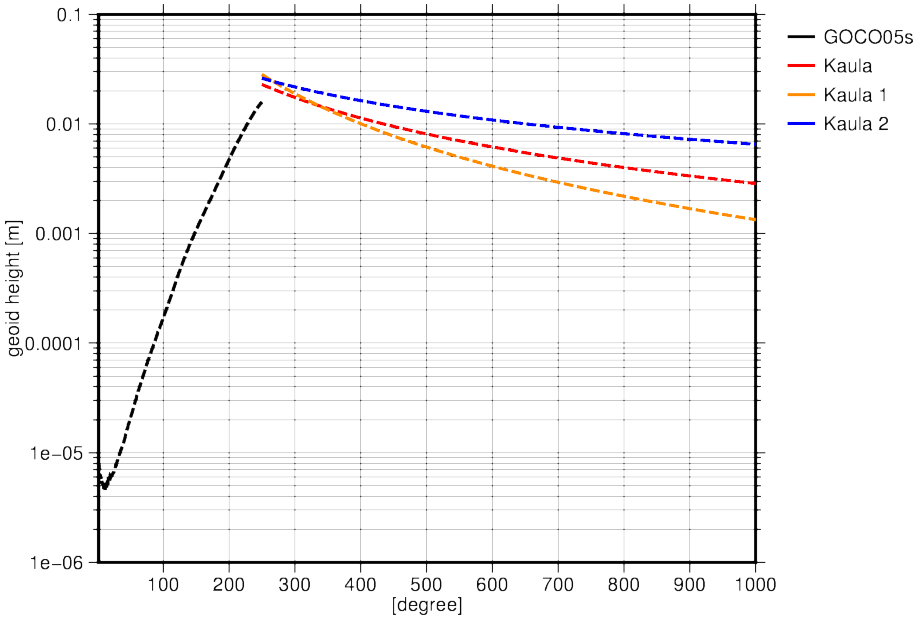

Figure 6.13: Different degree variance curves based on Kaula computation and GOCO05s error degree variances; original Kaula (red), adapted Kaula 1 (orange) and adapted Kaula 2 (blue), starting from d/o 251 → 9000;

6.3.4 Spatial Distribution of Radial Basis Functions

In contrast to spherical harmonics, which are not localized in space, the spatial distribution of the space localizing RBFs is essential for the quality of regional gravity field modeling. For high quality gravity field estimation the localization of the basis function is determined by means of a grid, where the corresponding grid points represent the individual spatial localization on the sphere. There are several existing approaches dealing with the topic of point distributions on the sphere. In *(Eicker, 2008)* an overview about different grid types is provided.

Due to empirical investigations, the choice of the grid, as well as the location of the RBF on the sphere, is irrelevant if the chosen basis functions are close enough to each other. For example, in order to reconstruct the input gravity dataset, which is given with a spatial distance below 2×2 km in some areas, a basis function grid with similar spatial resolution is recommended to avoid bigger residuals. On the one hand a small residual vector $\hat{\boldsymbol{\epsilon}}$ (see Eq. (5.13)) requires a dense RBF grid point distribution but on the other hand the number of unknown RBFs and their corresponding scaling factors to determine are constrained by the characterization of the least squares approach to be overdetermined. This means that the number of observations must exceed the number of unknown parameters and therefore the level of densification is limited. To cover all possible cases which occur within this research, the triangle vertex grid [see e.g. *(Schmidt, 1981)*] is chosen to represent the RBF location. It is suitable for all gravity field observations, especially if the estimated geoid solution is computed on a regular grid, which is a common approach.

Nevertheless, from a global point of view the chosen spatial resolution results in a huge amount of basis functions, homogeneously distributed over the sphere. In order to carry out a gravity field estimation without any computational delay, the basis function locations are tailored to the borders of the used terrestrial input dataset, including a buffer of several kilometers to minimize edge effects. This results in 37891 RBFs, well distributed within the area of interest, as shown in Fig. 6.14. Furthermore, all achieved results of this thesis are based on this triangle vertex grid arrangement.

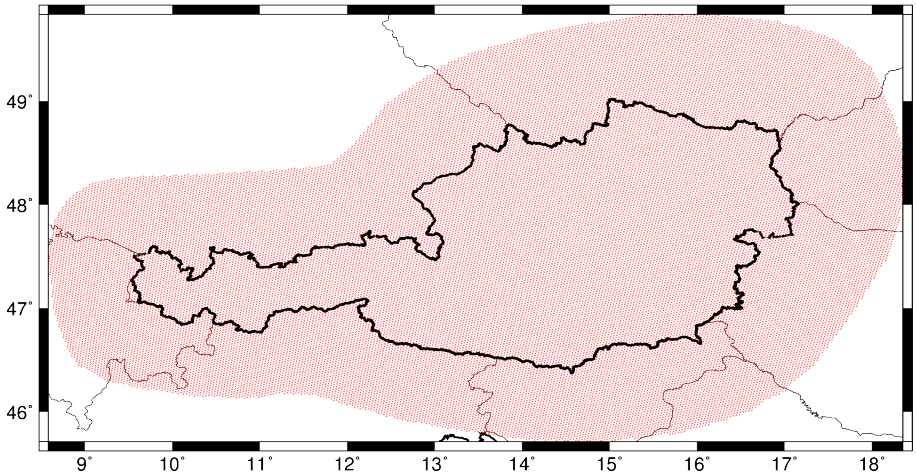

Figure 6.14: Triangle vertex grid of 37891 RBFs in the area of interest which corresponds to a spatial distance of approximately 2×2 km

Definition of the Triangle Vertex Grid

This grid type is characterized by the fact that the grid points are located at vertices. The basis of this grid is also referred to as icosahedron, which essentially consists of 12 vertices and 20 faces. The number of global grid points can be calculated according to *(Eicker, 2008)*

$$I = 10\ (l+1)^2 + 2\ , \tag{6.36}$$

where l indicates the level of densification. For this thesis a level of $l = 2846$ has been chosen, resulting in approximately 81 Mio. points, which corresponds to a global spatial resolution of about 2×2 km and 37891 RBFs. In Fig. 6.15, the triangle vertex grid for $l = 3$ and the individual steps of the grid determination are shown.

First, the triangle edges of the icosahedron are subdivided according to the chosen level of densification. Next, these points are connected to each other by means of arcs of great circles, resulting in intersections within the individual face and the newly established points, located at these intersections. These newly established points become the node points of the densified grid. This is repeated for all faces of the icosahedron, as can be seen in the lower right part of Fig. 6.15. For more details, the reader is referred to *(Eicker, 2008)*.

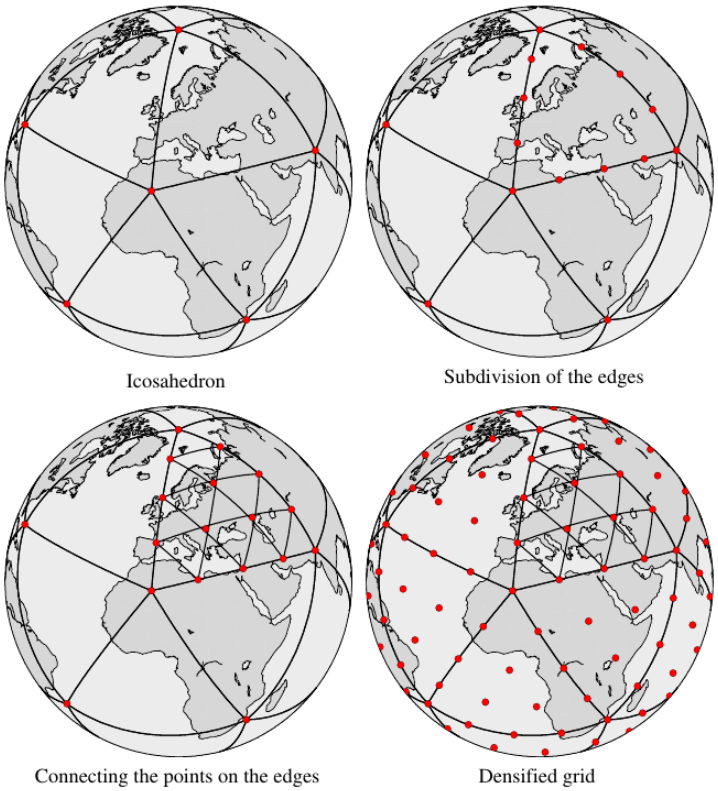

Figure 6.15: Triangle vertex grid of level 3 [courtesy by *(Eicker, 2008)*]

6.4 Restore Step - Compute the Solution

Within the restore step, all previously removed gravity field signals are restored and added to the estimated quantities derived from the compute step. In case of gravimetric geoid determination, the residual geoid is computed based on the reduced gravity data and within the restore step geoid heights are added. The geoid displays more long wavelength behavior, whereas the gravity anomalies can be classified as representative of the entire wavelength bandwidth. Therefore, remove and restore steps cover different wavelength bands which also holds for deflections of the vertical.

The restore step for the short wavelength component is carried out at geoid height N^{GGM} derived from the GOCO05s model up to d/o 250. This follows the spirit of providing a more realistic Taylor point in order to minimize linearization errors. First, all components from the reduction step need to be reversed within the restore step, which is achieved according to

$$N = N^{RBF} + N^{GGM} + \delta N^{topo} + \delta N^{atm} + N^{iso}_{SH} \ . \tag{6.37}$$

N^{RBF} denotes the estimated residual geoid based on a residual disturbing potential, as described in sec. 6.3. The combined topographic effect is denoted as δN^{topo} which accounts

for long wavelength topographic masses which are already covered by the N^{GGM}. This topic is treated in sec. 6.4.2. The combined atmospheric effect δN^{atm} accounts for exterior and interior potentials is discussed in sec. 6.4.3, and the short wavelength part of isostasy, starting from degree $N_n^{GGM}+1$, is denoted as N_{SH}^{iso}. The impact of this effect is discussed in sec. 7.4.7.

6.4.1 Long Wavelength Part

The long wavelength geoid heights for Austria are derived from the GOCO05s model as illustrated in Fig. 6.16. The N^{GGM} geoid is computed up to d/o 250 and shows the expected long wavelength behavior, especially in the Alps region. Moreover, this geoid is used as a reference solution to minimize linearization errors as discussed in e.g. sec. 6.2.2.

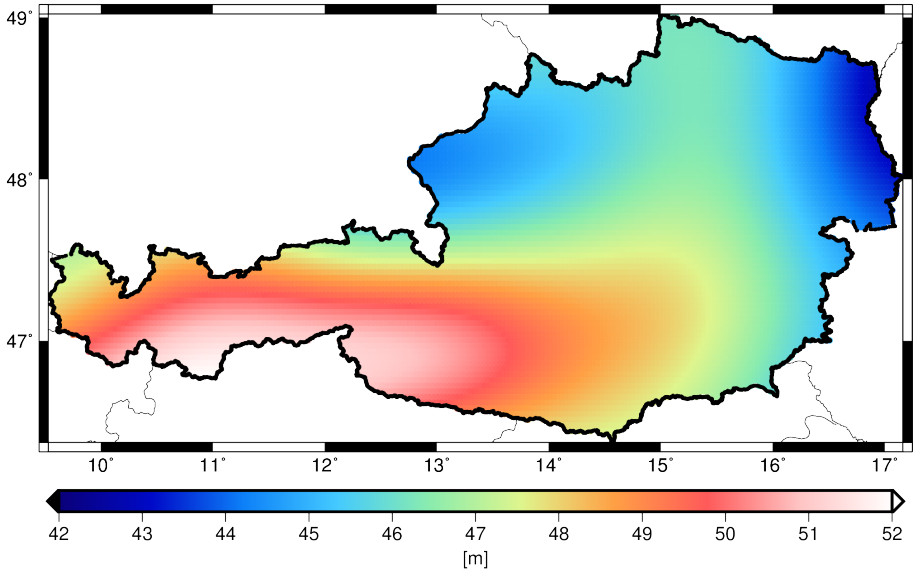

Figure 6.16: Geoid heights N^{GGM} based on the GOCO05s model up to d/o 250, covering the long wavelength component of the gravity field

In Tab. 6.4, the corresponding statistics is presented. As a matter of fact, the obtained geoid heights up to d/o 250 are able to represent a suitable first order approximation of the final geoid but lack from the high frequent, short wavelength components. This global representation of a geoid provides the biggest contribution to the final regional solution, because the magnitude of the missing high frequent components of the residual geoid as well as the topography derived part is of about ± 1.4 m. This in turn is only possible in case of a consistent combination of global gravity field data with the complementary terrestrial datasets and a rigorous spectral separation of the different bandwidth as discussed in sec. 6.2.

Table 6.4: Statistics of the long wavelength geoid up to d/o 250

[m]	min	max	mean
N^{GGM}	42.87	51.97	47.25

6.4.2 Topographic/Isostatic Part

The topographic part represents predominately the short wavelength component of the gravity field. In case of the geoid it is the same computation procedure as for the remove step. The rigorous spectral separation also has to be considered in order to avoid a double consideration of the topographic masses. The evaluation height is referred to the N^{GGM} geoid and therefore topographic masses are located above (see also sec. 7.4.1). However, equations for the exterior potential are valid as presented in sec. 6.2.3 for the topography derived geoid heights. The corresponding spherical harmonic representation up to d/o 250 is described in sec. 3.3.1. Hence, the combined topographic effect is defined as

$$\delta N^{topo} = N^{topo} - N^{topo}_{SH} \ , \tag{6.38}$$

where N^{topo} denotes the geoid height representation of the entire topographic masses within central Europe. In order to be consistent with the remove step and to avoid a spectral overlap in the RCR procedure, the mainly long wavelength components of the topography, denoted as N^{topo}_{SH}, are removed from the entire topographic potential. Therefore, only the desired short wavelength part of the topography beyond d/o 250 is remaining. This is shown in Fig. 6.17, and the corresponding statistics is presented in Tab. 6.5.

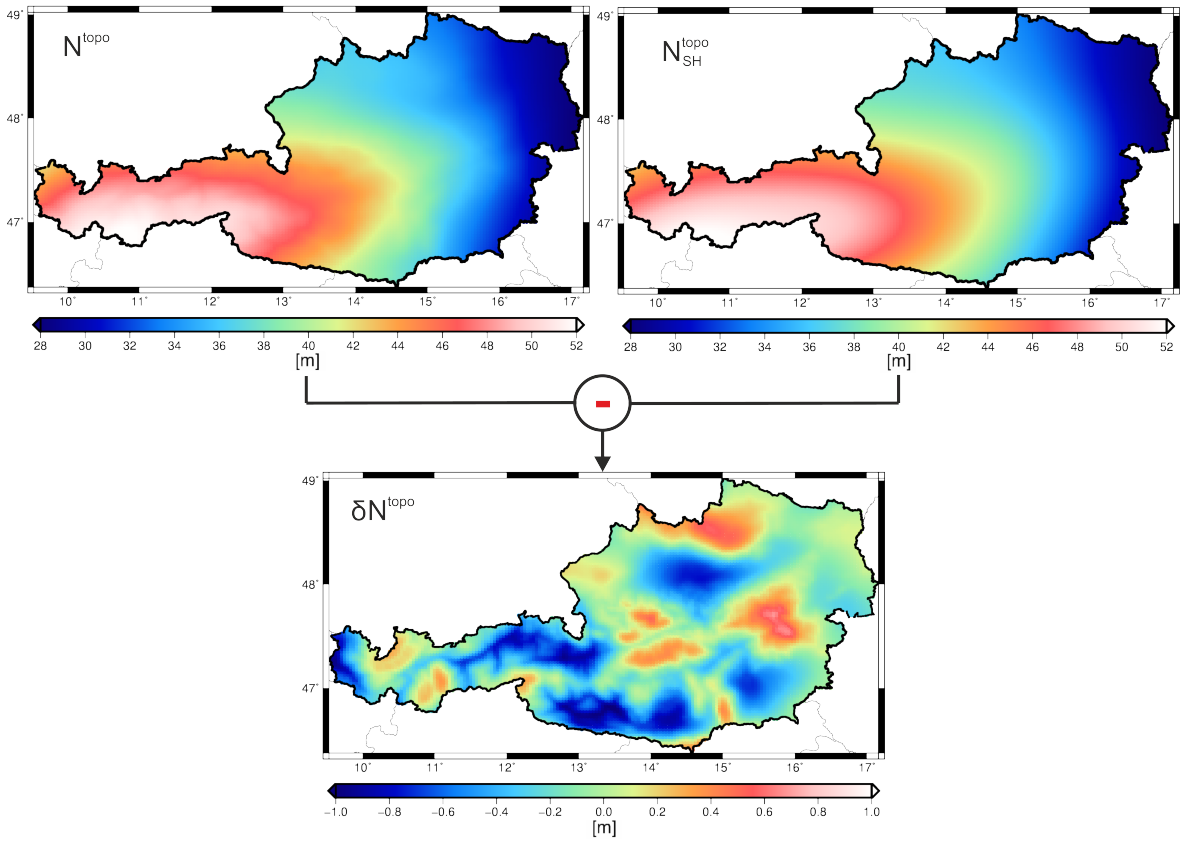

Figure 6.17: Remaining short wavelength topographic part in terms of geoid heights

Table 6.5: Statistics of short wavelength topographic part beyond d/o 250 in terms of geoid heights

[m]	min	max	mean	rms
δN^{topo}	-1.03	0.75	-0.15	0.37

With regard to the residual short wavelength isostatic part starting from d/o 251 $\rightarrow$ 500, the same behavior as for the gravity data, discussed in the remove step (see sec. 6.2.3) can be observed. This effect is again well covered by a GGM and no long wavelength structures are occurring as it is shown in Fig. 6.18. As illustrated, the geoid heights reflect the typical spherical harmonic structures with a spatial resolution of about 40-80 km, which corresponds to the maximum d/o of the isostatic series expansion. The corresponding statistics is presented in Tab. 6.6. The impact on the geoid validation is treated in sec. 7.4.7, at this point it is only mentioned that the residual isostatic part is compensated in the RCR procedure and can therefore been neglected.

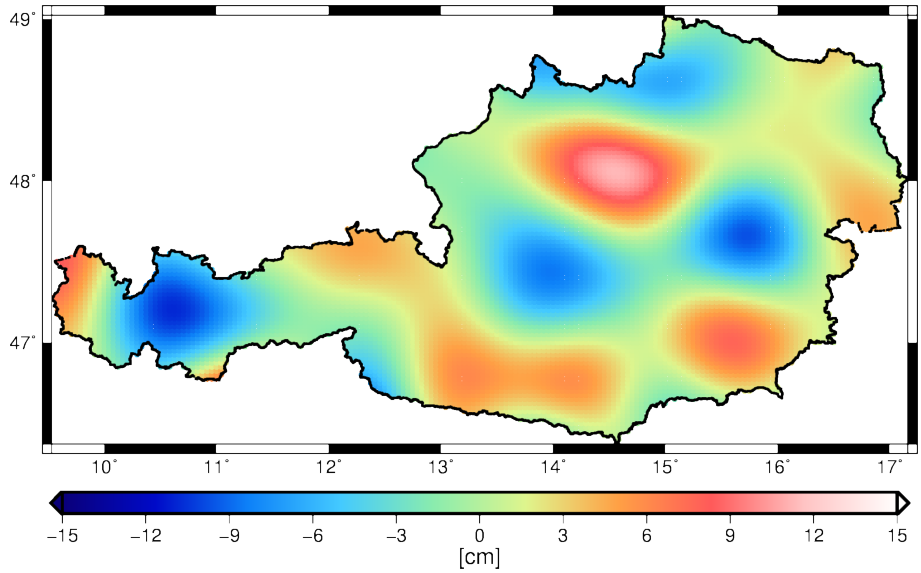

Figure 6.18: Remaining short wavelength part of isostasy in terms of geoid heights d/o 251 $\rightarrow$ 500

Table 6.6: Statistics of remaining short wavelength isostatic part in terms of geoid heights

[cm]	min	max	mean	rms
N_{SH}^{iso} d/o 251 $\rightarrow$ 500	-10.28	11.76	0.20	3.96

6.4.3 Atmospheric Part

The smallest contribution for the remove and also for the restore step is connected to the atmospheric potential. In terms of geoid heights, the combined atmospheric effect provides the inverse situation as for the remove step. It is defined as

$$\delta N^{atm} = N_{SH}^{atm,i} - N_{SH}^{atm,e} \ . \tag{6.39}$$

As can be seen in Fig. 6.19, these effects degrade approximately to a constant mean value of 0.35 cm with marginal variations in the range of one millimeter, which are connected to the topographic situation in Austria. The only impact on the final geoid solution is a slightly different bias, which does not contribute to an increased geoid accuracy compared to GPS/leveling observations. Due to consistency reasons within the RCR procedure it must be distinguished between interior and exterior potentials as discussed in sec. 6.2.4.

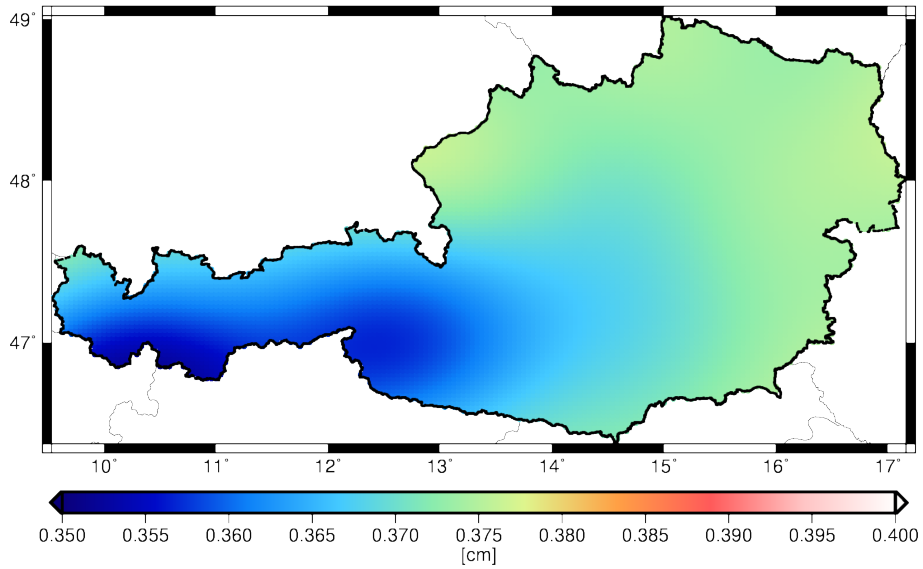

Figure 6.19: Geoid heights based on the combined atmospheric effect

Table 6.7: Statistics of geoid heights based on the combined atmospheric effect

[cm]	min	max	mean
δN^{atm}	0.35	0.37	0.36

7 Calculation and Results

In this chapter all relevant results of the thesis are summarized. The theoretical basis and a detailed description about the data used is provided in previous chapters. First, the reduced datasets for geoid computation are shown, which are the basis for all further output. Afterwards, the different estimated geoid solutions and the corresponding geoid validation are presented. Later, different investigations and methodological developments are discussed. Finally, a map for deflections of the vertical based on consistent reduced gravity is estimated and validated.

7.1 Reduced Datasets for Gravity Field Estimation

7.1.1 Reduced Gravity Data

The used gravity dataset consists of 72327 individual observations which are reduced by global, local and atmospheric parts. Furthermore, a double consideration of the topographic masses is avoided by means of a rigorous spectral separation between long- and short wavelength components (see e.g. sec. 6.2.3). The reduced gravity data can be obtain by means of

$$\Delta g_{red} = g - \| \underbrace{\nabla V^{GGM}}_{GOCO05s} + \underbrace{\boldsymbol{g}^{topo} - \boldsymbol{g}^{topo}_{SH}}_{Topography} + \underbrace{\boldsymbol{g}^{atm,e}_{SH} - \boldsymbol{g}^{atm,i}_{SH}}_{Atmosphere} + \boldsymbol{g}^{cen} \| \ . \tag{7.1}$$

The reduction is carried out according to the full vector approach, which is described in more detail in sec. 6.2.1. The isostatic component is neglected as discussed in sec. 7.4.7. For this investigation the 2D surface density information is taken into account. Comparisons with other density assumptions can be found in sec. 7.4.2.

Table 7.1: Statistics of subsequently reduced 72327 gravity observations

[mgal]	min	max	mean	rms
GGM (GOCO05s)	-231.13	143.89	-26.34	51.42
Topography	-49.48	37.35	-0.85	11.40
Atmosphere	-48.95	37.99	-0.22	11.38

In Tab. 7.1 the statistics of gravity reduced subsequently by a Global Gravity field Model (GGM), topography and atmospheric effects is shown. In an initial step, the long wavelength

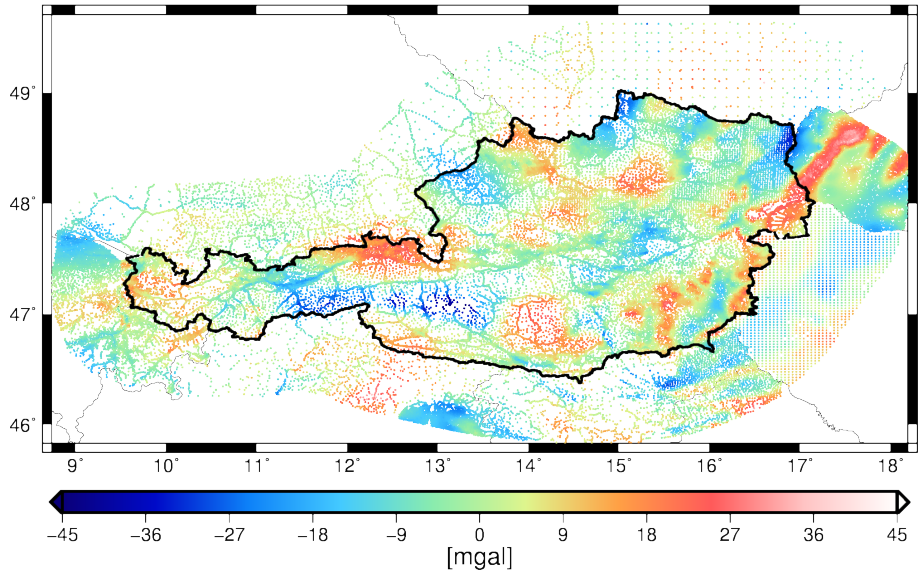

Figure 7.1: Reduced gravity dataset Δg_{red}

from the GOCO05s, up to d/o 250 and the centrifugal acceleration $\boldsymbol{g}^{cen}$ are subtracted from the measured data, leaving predominately short wavelengths remaining. This is also discussed in sec. 6.2.2. Afterwards, the topographic part, as illustrated in Fig. 6.6, is subtracted. Finally, the small atmospheric components are applied, which lead to the remaining variation of the reduced gravity data Δg_{red} of 11.38 mgal.

The smoothed dataset is shown in Fig. 7.1, and can mainly be attributed to gravity field signal. Remaining modeling deficiencies, especially in the area of the Tauern Window or in the Tyrolean Inn valley are connected to density variations in these regions [see *(Meurers and Ruess, 2007)*]. An important indication for the consistency of the entire dataset is the transnational continuous behavior of the reduced gravity. Although the dataset has grown historically and consists of several different data sources, as described in sec. 4.2.1, no unexpected behavior such as jumps along the Austrian borders can be observed. Furthermore, the chosen extended border for the gravity data surrounding Austria (approximately 100 km) has been determined empirically. A further extension beyond this does not contribute significantly to a geoid solution and leads only to additional computational efforts. Examining only the reduced Austrian data subset, which consists of 49354 observations, the minimum and maximum values as well as the data variety in terms of rms slightly decreases in comparison to the entire dataset. The corresponding statistics can be found in Tab. 7.2.

Table 7.2: Statistics of Austrian gravity data subset

[mgal]	min	max	mean	rms
Δg_{red}	-48.25	33.43	-0.01	11.02

7.1.2 Reduced Deflections of the Vertical

For the computation of the long- and short wavelength parts of the deflections of the vertical, the full vector approach is applied analogously to Eq. (7.1), but only the first two components of the computed gravity vector are finally considered and subtracted from the measured ξ and η values (see sec. 3.5.3). If this vector is evaluated in a local left-handed coordinate system [see e.g. *(Hofmann-Wellenhof and Moritz, 2006)*], the computed deflections can be directly subtracted from the astronomic measurements and the reduced values are obtained. The corresponding series expansion as functionals of the disturbing potential, are presented in sec. 3.5.3. The deflections are the second gravity field quantity which is considered as an input in this research. The dataset is therefore used twice. First, for a pure astrogeodetic geoid solution and secondly within a combined geoid solution in combination with gravity data. The stand-alone solution especially provides an unexpected quality of the astrogeodetic geoid although of sparse observations (see sec. 7.2.2). Therefore, the information content of this observation type indicates to be higher in comparison to gravity data but it suffers from sparse data distribution (see sec. 7.4.6). Finally, measured deflections of the vertical are used for the validation of the estimated ξ and η maps, as described in sec. 7.5. The reduced deflections of the vertical are shown in the following two illustrations, where the ξ_{red} component is shown in Fig. 7.2 and the η_{red} component in Fig. 7.3, respectively. In Tab. 7.3 the statistics is presented.

Table 7.3: Statistics of 735 reduced deflections of the vertical

[sec]	min	max	mean	rms
ξ_{red}	-6.97	6.68	0.28	1.93
η_{red}	-4.98	5.40	0.26	1.62

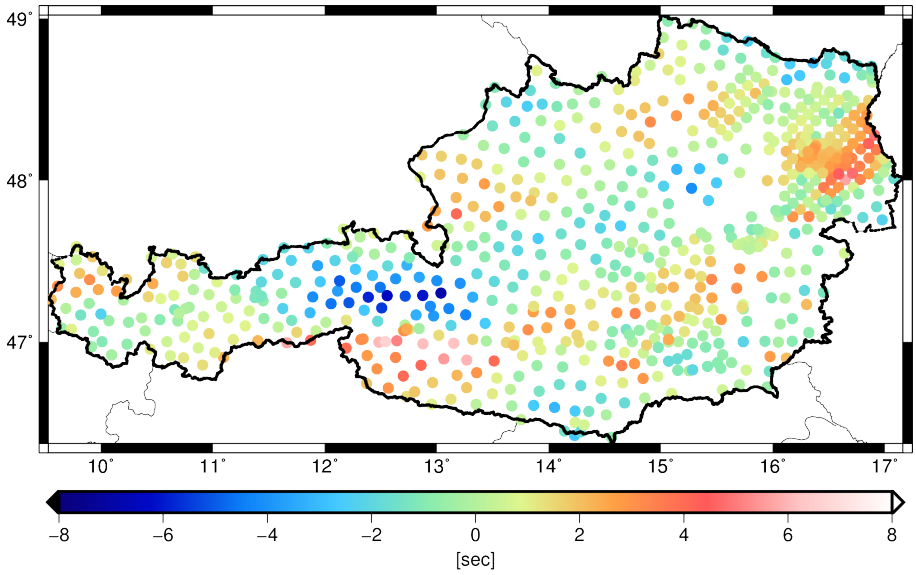

Figure 7.2: Reduced North-South ξ_{red} component

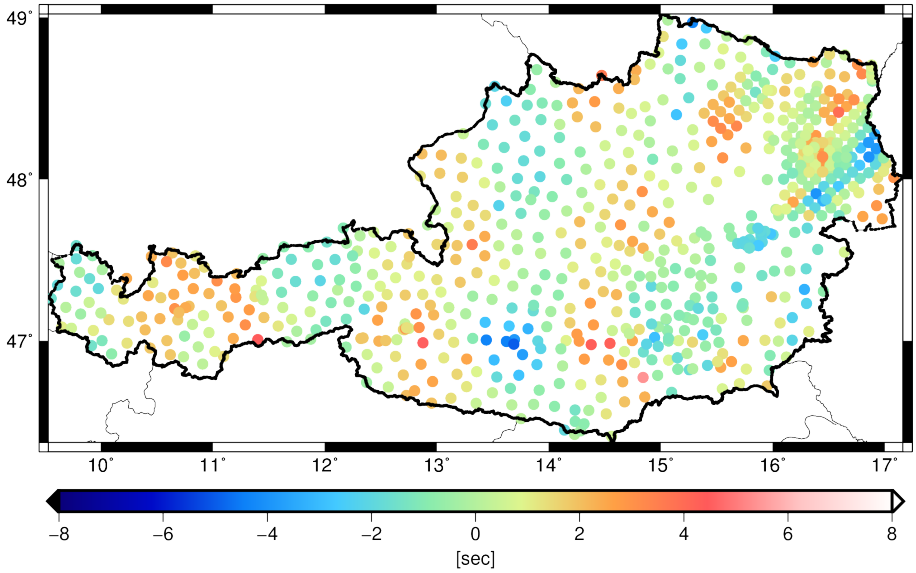

Figure 7.3: Reduced East-West η_{red} component

One rule of thumb is that masses, or mass anomalies, with North-South orientation show up in the η direction, whereas masses with East-West orientation show up in the ξ component. Mass anomalies with different orientation show up in both components.

The reduction has been carried out according to sec. 6.2, whereas long- and short wavelength reductions are considered with a consistent treatment of the topographic masses, as described in sec. 6.2.3. Furthermore, the 2D surface density model is taken into account. What can be seen in both figures is that the reason for the gravity field signal are the same as for the gravity data. One example can be made of the Tauern Window region *(Meurers and Ruess, 2007)*, which is of East-West direction. It is clearly visible in the ξ component, which in turn represents the North-South direction of the deflections. Here, the predominantly part of the signal can be explained with density variations, which reach down far below the Earth's surface.

7.2 Estimated Residual Geoid Heights

In previous sec. 7.1, the reduced gravity field quantities used for the geoid estimation are presented in detail. In this section the computed residual geoid heights are shown, but the full restore step has not yet been carried out. Depending on the used input data, the solution is attributed to a gravimetric, an astrogeodetic or a combined geoid.

7.2.1 Gravimetric Solution

The gravimetric geoid solution has been computed based on the entire reduced gravity data of 72327 observations and the 2D surface density information as described in sec. 4.4. The residual geoid is denoted as N_{grav}^{RBF}, and this is related to the 37891 estimated Radial Basis Functions (RBF) scaling coefficients, as discussed in sec. 6.3. The final output is shown Fig. 7.4 and the corresponding statistics can be found in Tab. 7.4, where the mean value is 3 mm. The relative weighting between the observation groups has been performed by Variance Component Estimation (VCE) method, with ten individual observation groups as discussed in sec. 5.2.3. The occurring residual geoid structure is, as expected, correlated with the gravity anomalies (compare with Fig. 7.1). This represents, apart from the topographic part, one supplement to the GGM based N^{GGM} geoid, which is shown in sec. 6.4.1. Furthermore, the corresponding standard deviations derived from the least squares approach (see sec. 5.1) provide the formal accuracy.

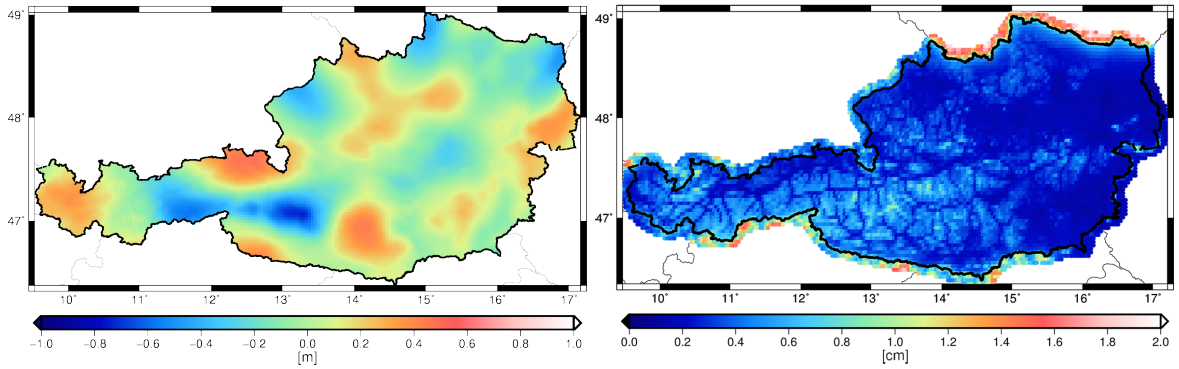

(a) Estimated gravitational geoid

(b) Standard deviations

Figure 7.4: (a) Estimated gravimetric residual geoid heights; (b) Corresponding standard deviations

Table 7.4: Statistics of gravimetric residual geoid on approximately 3×3 km grid

[m]	min	max	mean	rms
N_{grav}^{RBF}	-0.74	0.49	0.00	0.21

The standard deviations mainly reflect missing gravity observations and data gaps. Within Austria the model appears to have an average standard deviation of $\sigma < 0.5$ cm. Only in the alpine regions, with sparse gravity observations, the sigma values can reach a maximum of 1.2 cm. In contrast to Fig. 7.4a, where only the Austrian territory is illustrated, the corresponding sigmas are shown slightly beyond Austrian borders, which is indicated in Fig. 7.4b. Reviewing only these border regions, the observation situation is reflected again and the standard deviation reaches its overall maximum, which is up to 2 cm. This holds true for regions with only a few gravity observations, like the borders to the Czech Republic. The computed formal errors are quite optimistic because they do not cover the whole error budget e.g. DTM errors are not considered. To provide a more realistic interpretation of the geoid quality, the

formal errors need to be calibrated. The validation with independent GPS/leveling observations as well as with the official Austrian geoid, which is presented in sec. 7.3, show rms values < 3 cm. The relationship between different error contributors is assumed as

$$\sigma^2_{val.} = \sigma^2_N + \sigma^2_{GPS/lev.} \ , \tag{7.2}$$

where $\sigma_{val.}$ represents the validation result and $\sigma_{GPS/lev.}$ denotes the GPS/leveling quality. By simple rearrangement of Eq. (7.2), the geoid standard deviation may expressed as

$$\sigma_N = \sqrt{\sigma^2_{val.} - \sigma^2_{GPS/lev.}} \ . \tag{7.3}$$

In case $\sigma_{val.} = 3$ cm and $\sigma_{GPS/lev.}$ is assumed to be 2 cm, a geoidal standard deviation of 2.3 cm is computed which represents a more realistic assumption of the geoid quality. This approach can be applied to the astrogeodetic and combined geoid solution as well. Further investigations on the quality of Austrian GPS/leveling measurements have been made by *(Rülke et al, 2013)*, resulting in a more pessimistic assumption of 3.8 cm, but only 17 out of 192 GPS/leveling observations are considered in this investigation.

7.2.2 Astrogeodetic Solution

The astrogeodetic solution is based on 735 reduced ξ and η components, as presented in sec. 7.1.2. Within the VCE they are treated as one observation group. Applying regularization finally leads to two observation groups, where the a-posteriori σ of the deflections results in 0.54" (see sec. 5.2.3). At this point, it must be noted that the number of observations corresponds to a relation of 1:100 compared to the gravity dataset. Nevertheless, the results achieved, based on these few observations are remarkable, which is discuss in more detail in sec. 7.3.3. In Fig. 7.5 the computed residual geoid and the corresponding standard deviations are shown. Due to sparse observations the formal standard deviations are significantly higher compared to the gravimetric geoid solution.

Table 7.5: Statistics of astrogeodetic residual geoid on approximately 3×3 km grid

[m]	min	max	mean	rms
N^{RBF}_{astro}	-0.74	0.46	0.00	0.21

Differences between the gravimetric and astrogeodetic geoid solution are shown in Fig. 7.6a. Prominent features can be identified in the Styrian region and for the entire area differences up to ± 14 cm occur, although there is a considerable amount of observations available in this region. Further investigations on this have been carried out. Therefore, the deflections are treated individually as two different observation groups with an estimated variance component each, which leads to a relative down weighting of one group against the other. The regularized

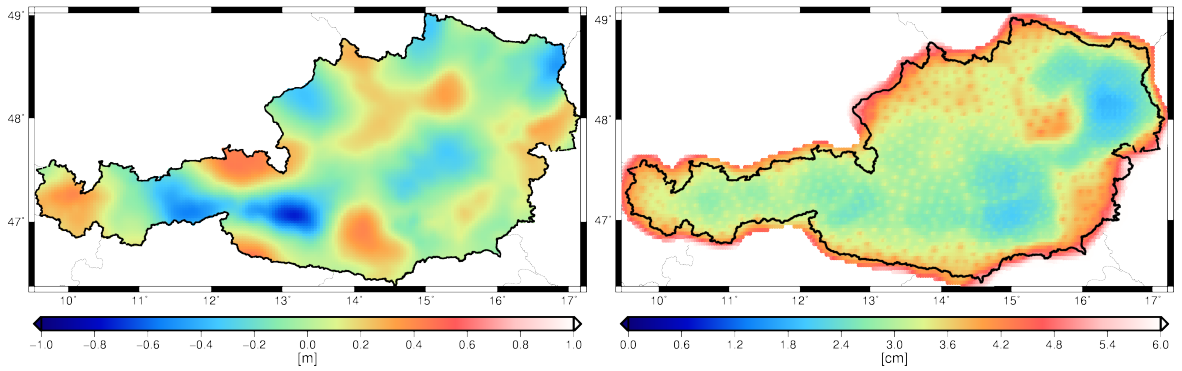

(a) Estimated astrogeodetic geoid (b) Standard deviations

Figure 7.5: (a) Estimated astrogeodetic residual geoid heights; (b) Corresponding standard deviations

solution of the a-posteriori σ for the ξ component is 0.39" and the corresponding η component is 0.49", which indicates that the North-South component is determined slightly better. The reason for this is attributed to historical time determination as discussed in sec. 4.2.2. The two individual variance components for the deflections are different compared to the estimate within a combined geoid solution due to the relative weighting. Nevertheless, the prominent features in comparison to the gravimetric geoid do not vanish because only slight geoid height differences in the range of about $\pm$ 1 cm between the two astrogeodetic solutions are observable which is shown in Fig. 7.6b.

In general, the astrogeodetic solution indicates superior information content of the deflections in comparison to the gravity data, which is further investigated in sec. 7.4.6. Unfortunately, the number of deflections and their distribution is too sparse to be truly competitive to the gravitational geoid solution, as reveals during the geoid validation (see sec. 7.3). Also within the combined solution, the contribution of these few observations almost disappears, as will be shown in sec. 7.2.3. It has to be noted, that the different solutions are directly comparable and no fitting to GPS/leveling observations is applied.

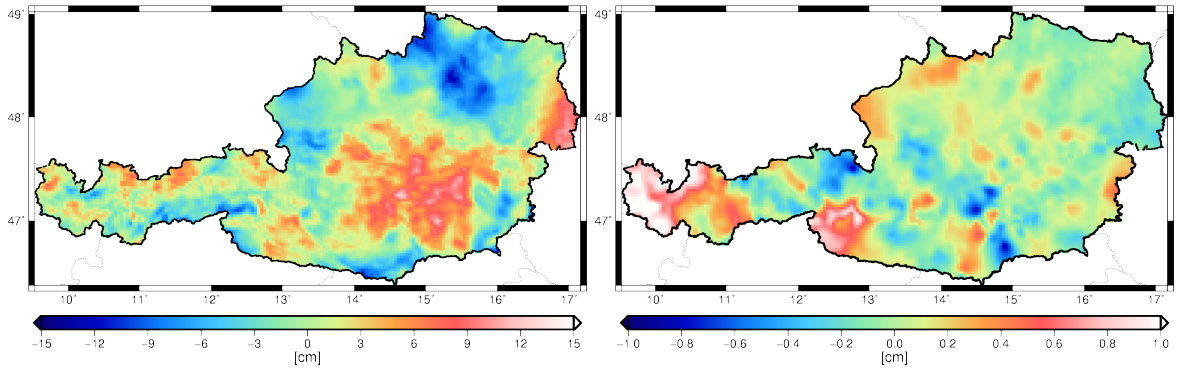

(a) Gravimetric minus astrogeodetic geoid (b) Differences in astrogeodetic solutions

Figure 7.6: (a) Geoid differences between gravimetric and astrogeodetic geoid; (b) Differences between two astrogeodetic solutions based on different observations groups

7.2.3 Combined Solution

The combined geoid solution is characterized by the fact that two purely physical gravity field quantities, the gravity anomalies and deflections of the vertical, are processed together in order to compute a geoid. The relative weighting between the different observation groups is computed by means of VCE. The same observation group scheme as for the pure gravimetric solution (see sec. 7.2.1) has been applied, with one additional group for the deflections of the vertical. As mentioned in sec. 7.2.2, the amount of available gravity measurements is considerably higher. Therefore, the combined geoid solution is mainly driven by these data and the contributions from the deflections are rather small. The achieved geoid solution (see Fig. 7.7a), as well as the corresponding formal standard deviations (see Fig. 7.7b), are very similar to the pure gravimetric geoid.

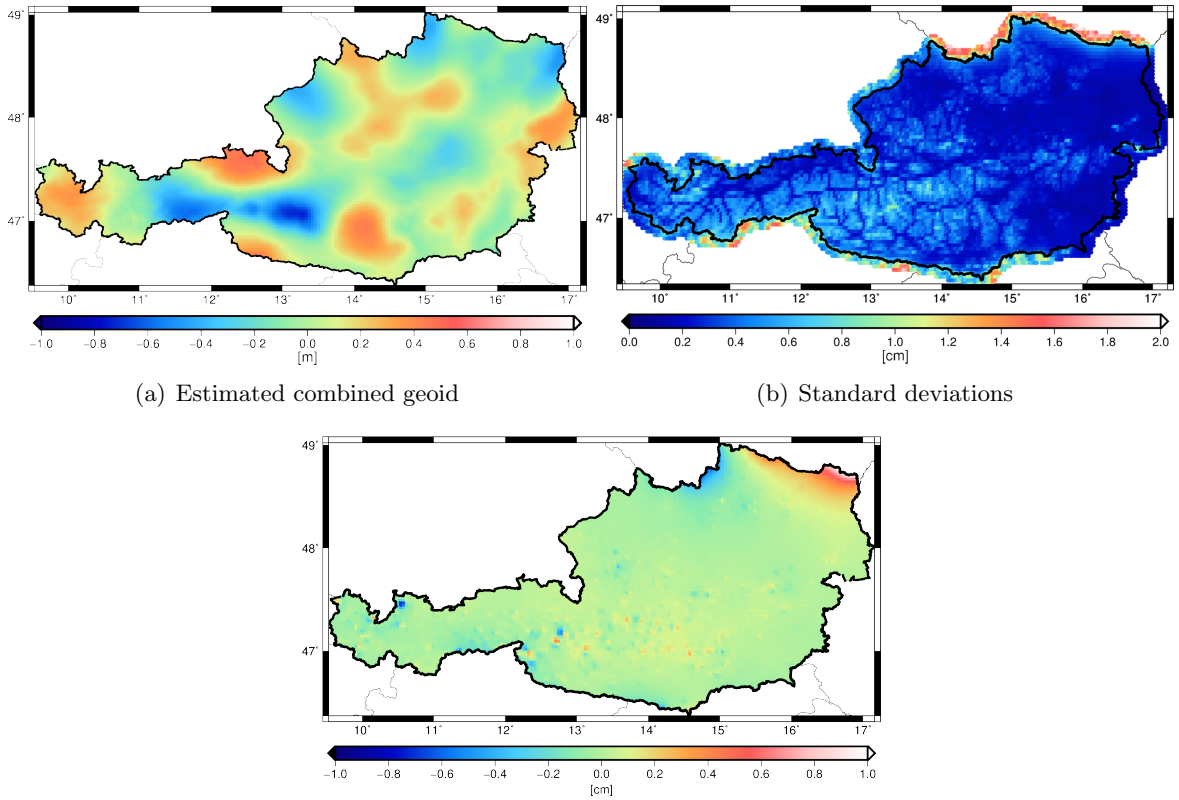

(a) Estimated combined geoid

(b) Standard deviations

(c) Difference of gravimetric and combined geoid

Figure 7.7: (a) Estimated combined residual geoid heights; (b) Corresponding standard deviations; (c) Differences between gravimetric and combined geoid solution indicating the influence of the additional deflection data

Table 7.6: Statistics of combined residual geoid on approximately 3×3 km grid

[m]	min	max	mean	rms
N^{RBF}_{combi}	-0.74	0.50	0.00	0.21

The differences between the gravimetric and the combined geoid solution represent the impact of the deflections of the vertical. As can be seen in Fig. 7.7c, the contribution to a combined geoid solution is small and limited to regions where the gravity observations are sparse. This can be seen again along the borders to the Czech Republic. Within Austria, scattered contributions can be observed but only with a magnitude of ± 1 cm and mainly located in mountainous regions. The sparse amount of deflections of the vertical within a combined solution leads also to non-significant changes compared to GPS/leveling data. Nevertheless, the information content of the deflections itself is higher compared to gravity measurements. Investigations have shown that at least three times more gravity data are needed to guarantee the same geoid quality level as discussed in sec. 7.4.6.

To give a qualified statement about the impact of the deflections, the geoid validation with independent GPS/leveling observations provides the first indicator, which is presented in sec. 7.3.4. The contribution of each individual gravity field quantity to a combined geoid solution gives a second indicator.

Contributions to a Combined Solution

The contributions of the individual normal equation systems to the estimated solution vector is discussed in more detail. The estimated solution vector $\hat{\boldsymbol{x}}$ consists of 37891 space localizing RBF scaling coefficients, as discussed in sec. 6.3 and the individual contributions of the normal equations [see Eq. (5.25)] in terms of percentage are shown in Fig. 7.8. The combined normal equation system consists of only three individual parts and the contribution can be derived from

$$(c_i)_k = \left(\boldsymbol{N}_i \boldsymbol{N}_{total}^{-1}\right)_k \ , \tag{7.4}$$

with

$$\boldsymbol{N}_{total} = \boldsymbol{N}_{\Delta g} + \boldsymbol{N}_{\xi,\eta} + \boldsymbol{N}_{GGM} \ , \tag{7.5}$$

providing the combined normal equation system. To show the contribution from the gravity data in a more comprehensible way, the ten individual gravity observation groups are united in a first step.

The gravity field quantity contribution, shown in Fig. 7.8a, belongs to gravity data. As can be seen, the estimated solution vector is dominated by gravity data in dependence of the corresponding spatial location of the data. In general, the following rule is valid for the three illustrations: the brighter the area, the higher the contribution of the gravity field quantity. This means, that in areas with dense gravity data the contribution can be up to 98 %. The inverse situation is in principle given in areas with sparse gravity observations. Within these

areas the solution is dominated by regularization as shown in Fig. 7.8b, where in this case the a-priori information is provided by the GOCO05s model, as indicated by $\boldsymbol{N}_{GGM}$ in Eq. (7.5). This in turn means that the main contribution to a combined geoid solution is coming from either gravity or from the regularization part.

In order to identify the contribution coming from deflections of the vertical, the colorbar has changed to 0-3 %. Deflections of the vertical are only available within Austria, hence their contribution to outside regions is almost zero, which is obvious and shown in Fig. 7.8c. The highest impact can be observed amongst the Austrian borders, again in areas where the gravity measurements are sparse. Here a small contribution may be identified. This again holds for the border with the Czech Republic and corresponds to the result shown in Fig. 7.7c, which can be characterized as the contribution in terms of geoid heights derived from deflections of the vertical in a combined solution.

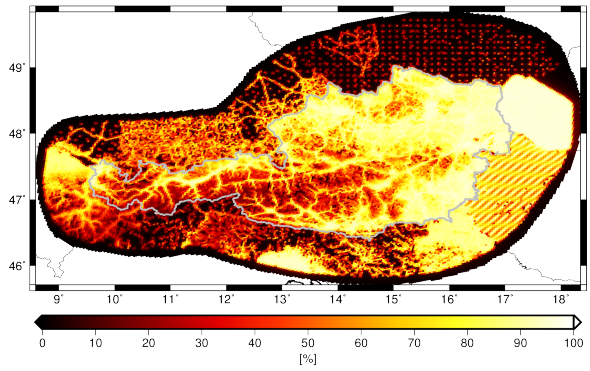

(a) Contribution of gravity data

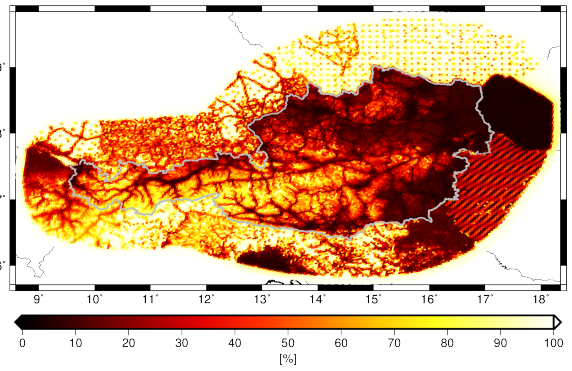

(b) Contribution of regularization

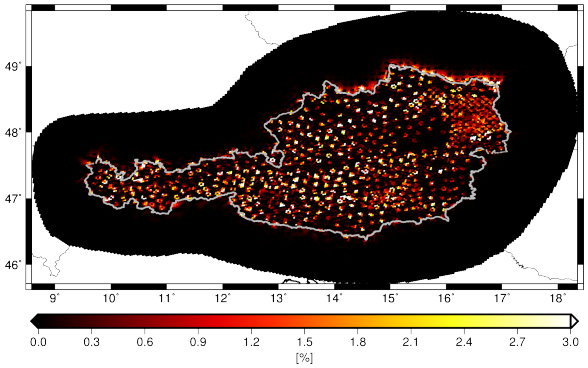

(c) Contribution of deflections of the vertical

Figure 7.8: (a) Contribution from gravity data [0-100%]; (b) Contribution from regularization [0-100%]; (c) Contribution from deflections of the vertical [0-3%]

7.3 Validation Issues

The validation of different geoid solutions, which are presented in the previous section, is based on fully restored geoid heights by comparison to independent GPS/leveling observations, as well as to the official Austrian geoid. Furthermore, geopotential numbers are also available for validation purposes.

7.3.1 Validation of Input Data

In order to verify the model used and to examine probable outliers in the different datasets, the residual vectors $\hat{\boldsymbol{\epsilon}}$, [Eq. (5.13)], are computed for the gravity data and for the deflections of the vertical. The corresponding results are shown in Fig. 7.9.

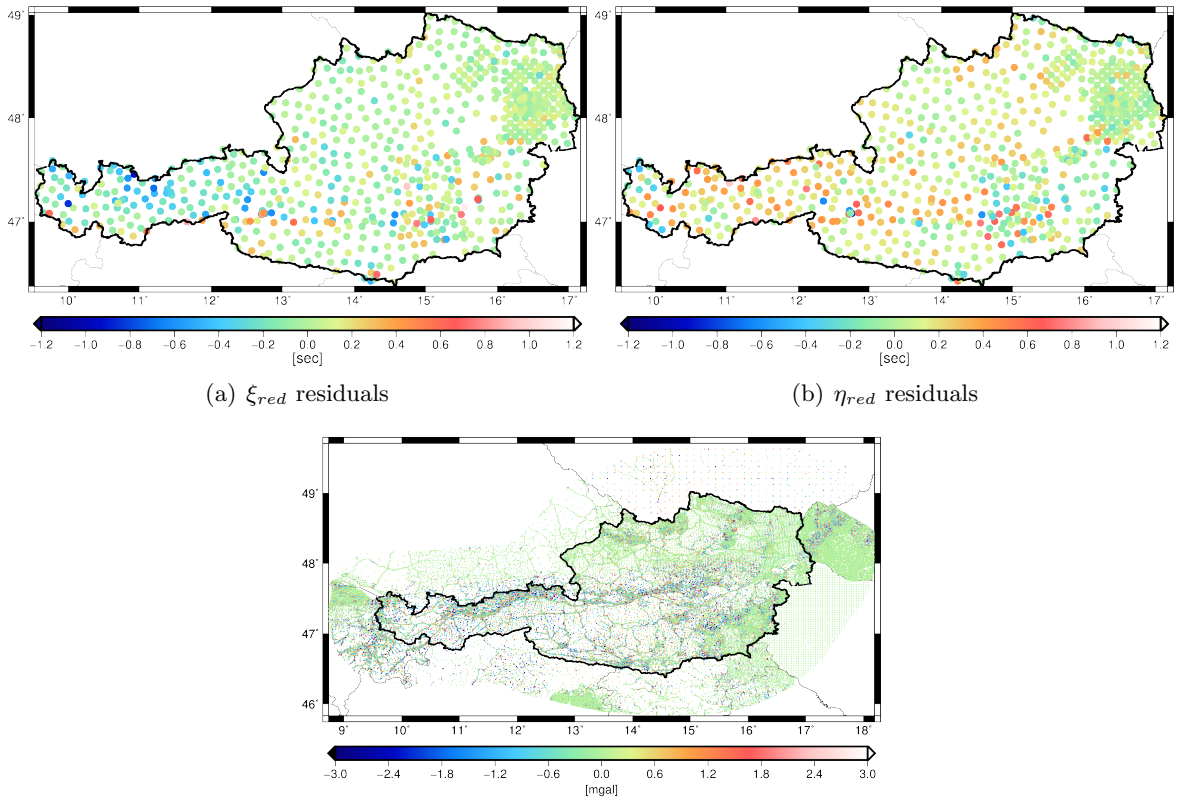

(a) ξ_{red} residuals

(b) η_{red} residuals

(c) Δg_{red} residuals

Figure 7.9: (a) 735 ξ_{red} component residuals; (b) 735 η_{red} component residuals; (c) 72327 Δg_{red} reduced gravity residuals

For the deflections of the vertical the same RBF parametrization as for the gravity data has been chosen. It must be noted that the post-fit residuals are computed either based on reduced gravity or on reduced deflections and no relative VCE weighting has been applied. For the gravity data the achieved rms is 0.87 mgal and for the deflections of the vertical 0.21" and 0.23" for ξ and η, respectively. This slightly differs from the VCE a-posteriori sigmas because

of the redundancies (see sec. 5.2.2). Furthermore, the deflections of the vertical are treated together as one observation group within a combined geoid solution (see sec. 5.2.3).

Looking closer at the deflection residuals which are shown in Fig. 7.9a and Fig. 7.9b respectively, significant differences especially in mountainous regions, as well as the Styrian region, where the biggest differences to a pure gravimetric solution are observed, can be identified. This indicates a slight error either in the observations or in the model used, which may cause these prominent features (see also sec. 7.2.2). Due to the fact that it is not possible to identify clear outliers in the deflection data and additionally take into account the circumstance of sparse observation data, all measured deflections are ultimately considered in the computation, although some of them are slightly above the 3σ level.

In case of gravity, the data distribution is very inhomogeneous. This makes it difficult for the evaluation of the occurring residuals because the chosen RBF distribution can not be that tight (see sec. 6.3.4). In some areas this may lead to an underrepresented gravity field signal and the occurring residuals are probably affected by this. This is the reason why all gravity data are taken into account and no outliers are removed from the dataset, although some data are clearly above the 3σ level. The statistics can be found in Tab. 7.7.

Table 7.7: Statistics of 735 deflections of the vertical and 72327 reduced gravity post-fit residuals

[sec]	min	max	mean	rms
$\hat{\boldsymbol{\epsilon}}_{\xi_{red}}$	-1.09	1.11	-0.01	0.21
$\hat{\boldsymbol{\epsilon}}_{\eta_{red}}$	-0.91	0.95	0.09	0.22
[mgal]	min	max	mean	rms
$\hat{\boldsymbol{\epsilon}}_{\Delta g_{red}}$	-7.01	6.95	0.01	0.87

7.3.2 Gravimetric Solution

The validation of the achieved gravimetric geoid is conducted in several ways. First, the solution is compared with independent GPS/leveling observations, which are assumed to be accurate within a range of a few centimeters (see sec. 4.2.3). Another comparison can be done with the official Austrian geoid solution, which is described in sec. 4.1.1, and finally a comparison with geopotential numbers is also possible. In order to carry out the different validations in a correct manner, all short and long wavelength components, as well as the atmospheric part which are discussed in sec. 6.4, have been added to the residual gravimetric geoid solution (see sec. 7.2.1) to achieve the fully restored geoid. This can be obtained by

$$N = \underbrace{N^{RBF}}_{Compute} + \underbrace{N^{GGM}}_{GOCO05s} + \underbrace{N^{topo} - N^{topo}_{SH}}_{Topography} + \underbrace{N^{atm,i}_{SH} - N^{atm,e}_{SH}}_{Atmosphere} . \tag{7.6}$$

In Eq. (7.6) the isostatic component is assumed to be covered by the long wavelength GGM representation (see sec. 7.4.7). The achieved geoid N is computed on a regular grid and the heights are within a range from 42.45 m up to 51.97 m with a corresponding mean value of 47.09 m. This is shown in Fig. 7.10a.

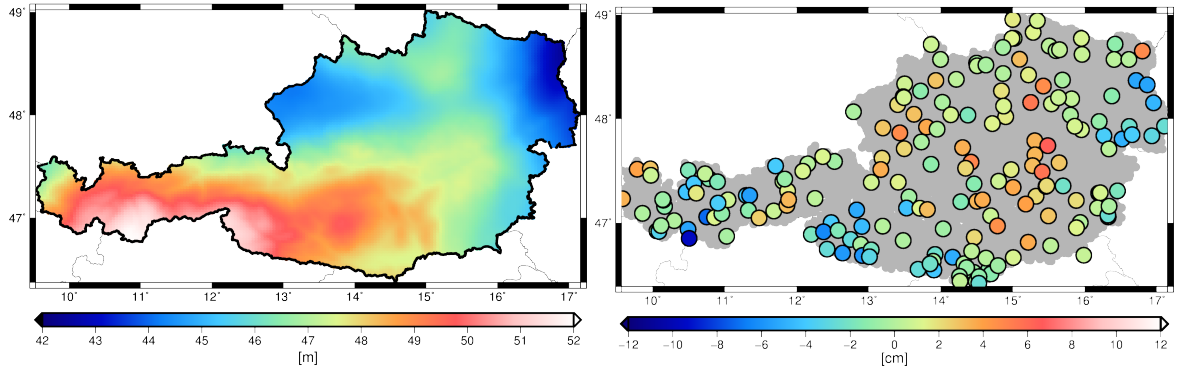

(a) Final computed gravimetric geoid

(b) Corresponding validation with GPS/leveling

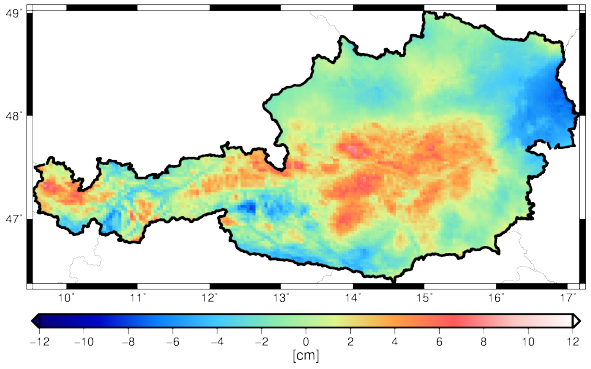

(c) Validation with official Austrian geoid

Figure 7.10: (a) Final restored gravimetric geoid; (b) Corresponding validation where a constant bias of -41.62 cm is removed; (c) Validation with official Austrian geoid solution where a constant bias of -41.20 cm is removed

The quality of the solution can be directly validated, if a constant mean value or bias is subtracted from the difference of the two solutions. There are several possible reasons for this bias. As stated by *(Rieser, 2015)*, one possible reason is an offset between the gravimetric geoid and the realization of the vertical leveling datum. Another potential reason is that an ellipsoid, which fits the gravimetric geoid best, might differ from the ellipsoid which is used for the calculation of the ellipsoidal GPS heights. Furthermore, the geoid is computed with respect to the GOCO05s which is given in a tide-free system, whereas the exact definition of GPS/leveling observations is connected to the EVRS/UELN98, defined as a zero-tide system for the orthometric part and to the GRS80/ETRS89 system for the ellipsoidal GPS height (see sec. 2.4) which gives a significant contribution to the bias. However, after the constant bias is removed from the data, a high-quality gravimetric geoid solution with a rms value < 3 cm has been established. The statistics including the bias values are presented in Tab. 7.8. In this rms range it can not be stated whether the error is in the computed geoid solution or still

in the validation points, because the BEV specifies their accuracy within a few centimeters. Consequently, one of the main goals of this thesis, to compute a gravimetric solution without applying constraints, which is competitive to the official Austrian geoid 2007 is achieved.

Table 7.8: Statistics of gravimetric geoid validation with 192 GPS/leveling observations and with the gridded official Austrian geoid N_{2007}

[cm]	min	max	bias	rms
$\Delta GPS/lev.$	-9.62	6.46	-41.62	2.75
ΔN_{2007}	-8.19	8.38	-41.20	2.80

Prominent features in the geoid differences show up in Fig. 7.10c. Investigations on the systematic effect located in the central part of Austria are carried out by means of a comparison to the EGM2008 geoid *(Pavlis et al, 2008)*. The differences are shown in Fig. 7.11, but a systematic effect is still visible in both solutions although the rms of the comparison to the national geoid is 4.36 cm and the present solution reveals a rms value of 3.90 cm. In contrast, it turns out that the national geoid fits well to 192 GPS/leveling observations due to the applied constraints and provides a better rms value (see sec. 4.2.3).

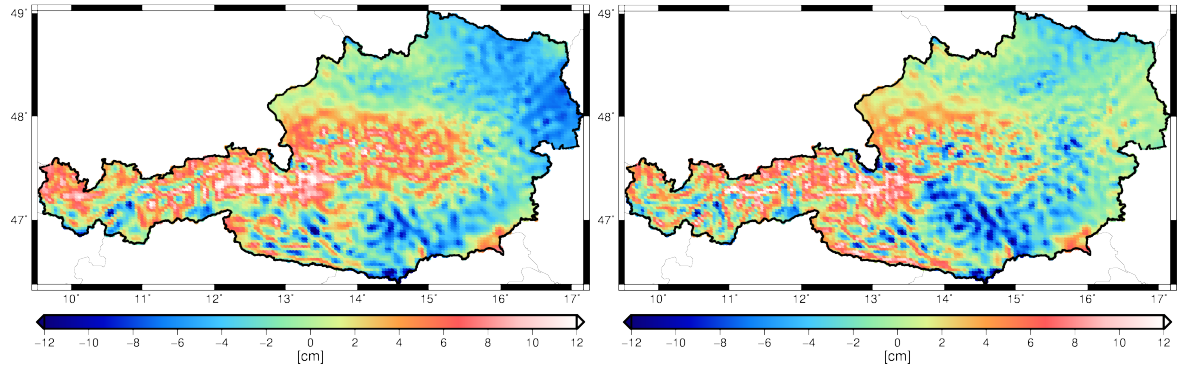

(a) Geoid height differences to official solution

(b) Geoid height differences to present solution

Figure 7.11: (a) Geoid height differences of the national geoid in comparison to EGM2008 derived geoid heights; (b) Geoid height differences of the present geoid solution in comparison to EGM2008 derived geoid heights

The short wavelength part of the topography contributes to these features as well as the use of 2D surface density information (see sec. 7.4.2) or the choice of the RBF shape as presented in sec. 7.4.5. Moreover, height errors in the data may also explain parts of this effect (see sec. 4.2.1). Finally, the reason could not be attributed to one singe effect and a reliable statement whether the systematic belongs either to the official Austrian geoid or to the present solution could not be provided in this research, which also holds for the combined geoid solution (see sec. 7.3.4). Occurring short wavelengths geoid differences e.g. in the Inn valley are attributed to a consistent treatment of the topographic masses within the restore step as described in sec. 6.4.2.

Another independent validation of the computed gravimetric geoid solution (see Fig. 7.10a) can be conducted on the potential level. The geopotential numbers are estimated from the gravimetric dataset and are compared to the values available for the GPS/leveling observations. The validation result is shown in Fig. 7.12, where the geopotential numbers are independent of the GPS derived ellipsoidal heights. Therefore, the similar occurring difference structure (compare Fig. 7.10b and Fig. 7.12) is an indicator that the ellipsoidal height, which is part of GPS/leveling observations, provides only a small contribution to the overall noise budget. It also shows that the major part of the occurring geoid differences is supposed to be connected to the orthometric heights. The corresponding statistics can be found in Tab. 7.9. This type of validation is only shown for the gravimetric solution but the characteristic is the same for the astrogeodetic, as well as the combined geoid solution.

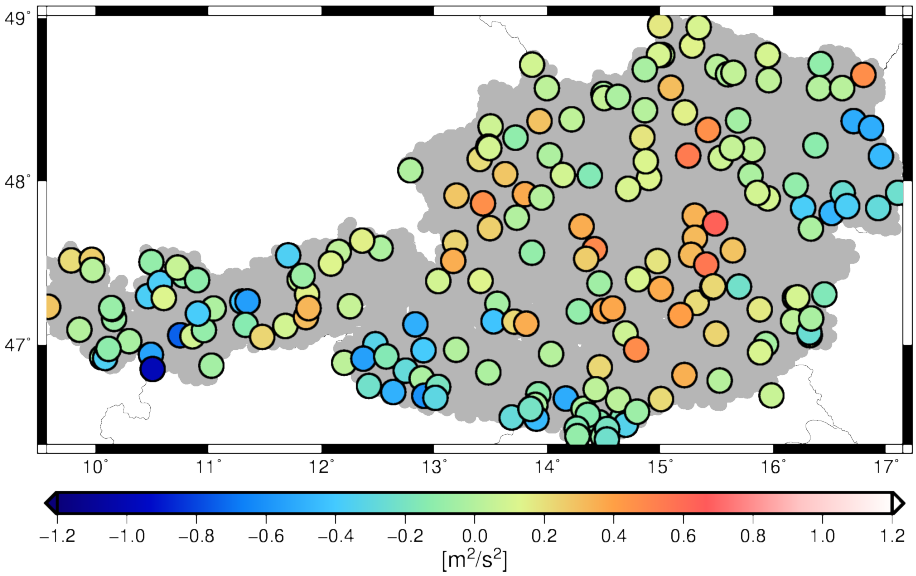

Figure 7.12: Validation with geopotential numbers

Table 7.9: Statistics of validation with 192 geopotential numbers

$[m^2/s^2]$	min	max	bias	rms
ΔC	-0.99	0.66	-4.09	0.27

7.3.3 Astrogeodetic Solution

The estimated astrogeodetic geoid is validated with GPS/leveling observations, as well as with the official Austrian geoid. As expected, it is not as accurate as the gravimetric solution, which can be attributed to the sparse observation situation is discussed in sec. 7.2.2. Nevertheless, the geoid validation shows rms values < 5 cm for both validation cases, which are shown in Fig. 7.13b and Fig. 7.13c. This is an indicator for the superior information content of deflections of the vertical in comparison to gravity data, which is discussed in more detail in sec. 7.4.6.

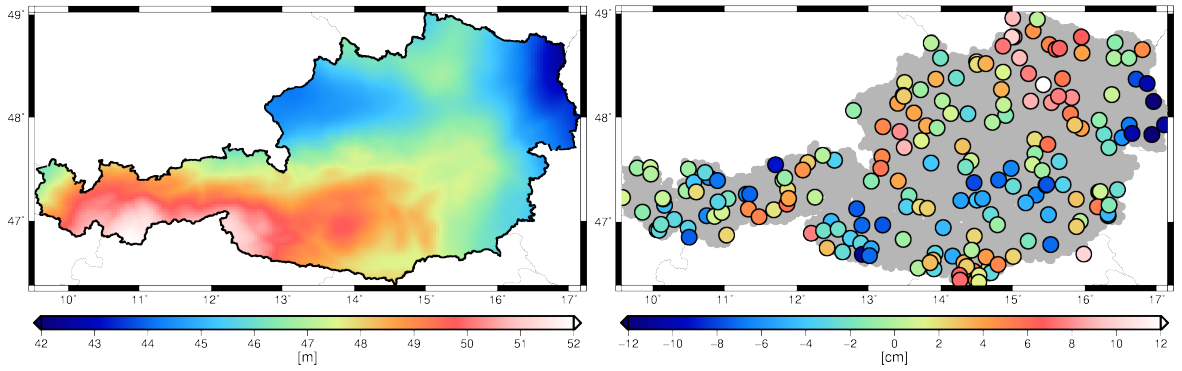

(a) Final computed astrogeodetic geoid

(b) Corresponding validation with GPS/leveling

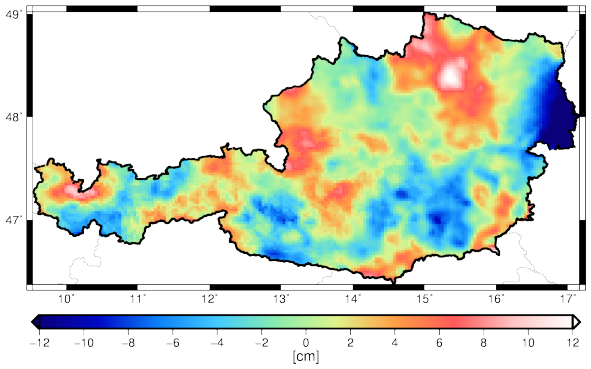

(c) Validation with official Austrian geoid

Figure 7.13: (a) Final restored astrogeodetic geoid; (b) Corresponding validation where a constant bias of -40.84 cm is removed; (c) Validation with official Austrian geoid solution where a constant bias of -41.31 cm is removed

Table 7.10: Statistics of astrogeodetic geoid validation with 192 GPS/leveling observations and with the official Austrian geoid N_{2007}

[cm]	min	max	bias	rms
$\Delta GPS/lev.$	-13.85	13.32	-40.84	4.92
ΔN_{2007}	-16.51	18.96	-41.31	4.22

7.3.4 Combined Solution

The validation of the combined solution shows in principle the same difference behavior as the pure gravimetric solution (compare Fig. 7.10 and Fig. 7.14). This is due to the fact, that deflections play a minor role within a combined geoid solution as already discussed in sec. 7.2.3. The validation with GPS/leveling measurements and with the national Austrian geoid displays a slightly increased rms value of about 1 mm, in comparison to the gravimetric solution. Consequently, the deflections do not significantly contribute to a geoid improvement and the quality of the gravimetric and combined solutions is regarded as equivalent. Furthermore, the prominent features in Fig. 7.14c are still visible (see sec. 7.3.2 for explanation).

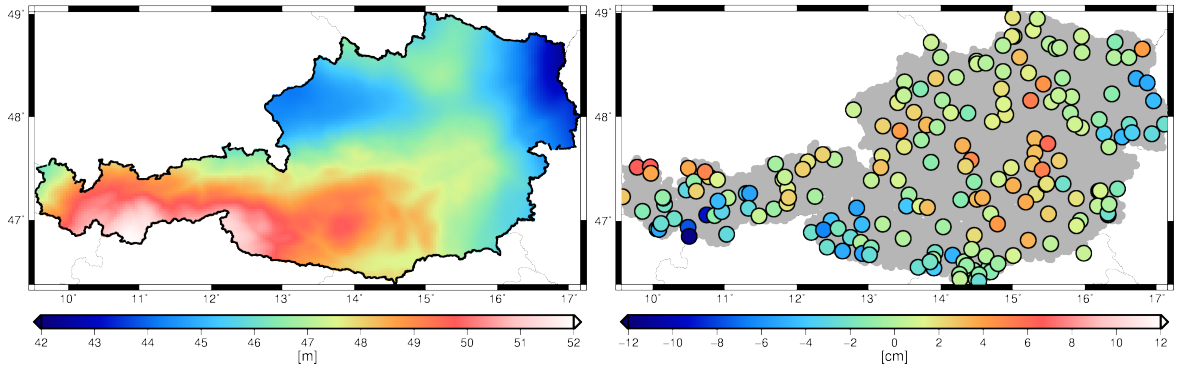

(a) Final computed combined geoid

(b) Corresponding validation with GPS/leveling

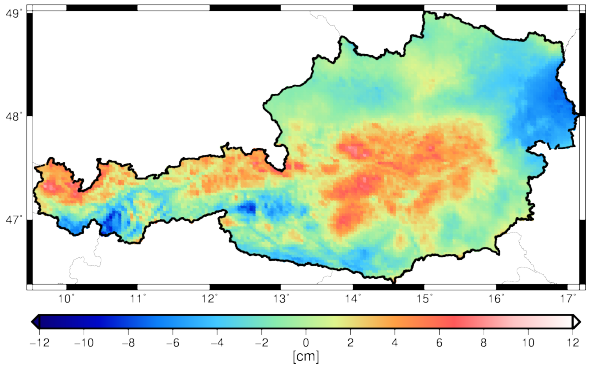

(c) Validation with official Austrian geoid

Figure 7.14: (a) Final restored combined geoid; (b) Corresponding validation where a constant bias of -41.59 cm is removed; (c) Validation with official Austrian geoid solution where a constant bias of -41.18 cm is removed

Table 7.11: Statistics of combined geoid validation with 192 GPS/leveling observations and with the official Austrian geoid N_{2007}

[cm]	min	max	bias	rms
$\Delta GPS/lev.$	-9.65	7.08	-41.59	2.89
ΔN_{2007}	-9.18	8.81	-41.18	2.92

7.4 Selected Investigations

7.4.1 Effect of Linearization

Introducing a more realistic Taylor point affects the computed potential as well as the geometrical representation and may be attributed to a methodological improvement in Austrian geoid computation. In a classical approach, the ellipsoid is introduced as Taylor point for the linearization, which also holds true for the Austrian geoid 2007. One attempt to introduce a more realistic Taylor point by means of a global geoid representation is completed in this research. In an initial step, this means serious computational efforts because all gravity field quantities and every gridded Digital Terrain Model (DTM) point needs to be assigned with geoid heights, based on a GGM. Due to consistency reasons the GOCO05s up to d/o 250 is chosen for the approximated geoid representation. As a consequence, the original definition of a gravity anomaly changes because it is related to an approximated geoid instead of the ellipsoid (see sec. 3.5.1). This new definition is slightly different compared to the classical approach, but benefits from up to date global satellite data.

The masses above the geoid need to be removed mathematically, which is connected to a geometrical representation of the Earth's topography by means of a DTM. Therefore, in a classical approach the topographic potential is computed starting from the ellipsoid up to orthometric height. A new approach used within this thesis introduces an approximated geoid as Taylor point for linearization and the potential is computed up to orthometric height plus geoid height. Therefore, a different definition of the mass column is given. However, the occurring gravity differences between these two approaches are on the μgal level and can therefore neglected but are in compliance with the theory of physical geodesy.

An additional benefit of a-priori geoid heights is that approximated ellipsoidal heights are available for every computation point (see sec. 6.2.2). This is important for the development of the topography into spherical harmonics, as discussed in sec. 3.3.1. Furthermore, the restore step in the new approach is also carried out on the geoid height level.

Normal Gravity and Global Gravity Field Representation

For the national Austrian geoid solution, the reduction of the measured gravity is carried out with respect to the ellipsoid and the corresponding normal gravity γ, with its GRS80 *(Moritz, 1980b)* representation as shown in sec. 3.4.1. Therefore, the long wavelength part can be computed according to

$$\Delta g_{red} = g - \gamma - \Delta g^{GGM} \ . \tag{7.7}$$

This research attempts to minimize linearization errors. Therefore, a more realistic Taylor point representation by means of GOCO05s derived approximated geoid heights is introduced, replacing the classical ellipsoid. As a consequence, the gravity representation is also exchanged and now refers to the GOCO05s model as representation of the gravity potential, which consists of the gravitational potential and the centrifugal potential. Both potential effects are summarized and the long wavelength derived gravity reduction can be expressed as

$$\Delta g_{red} = g - \|\nabla V^{GGM} + \boldsymbol{g}^{cen}\| \ , \tag{7.8}$$

where the corresponding result of the long wavelength reduction step is shown in sec. 6.2.2. The differences of the reduced gravity computed from Eq. (7.7) and Eq. (7.8) are shown in Fig. 7.15. In comparison to the accuracy of the gravity measurements the occurring differences are significant. Furthermore, slight geoid improvements can be observed if this approach is further extended to all constituents as defined in Eq. (7.1). In this case, the full vector approach is applied.

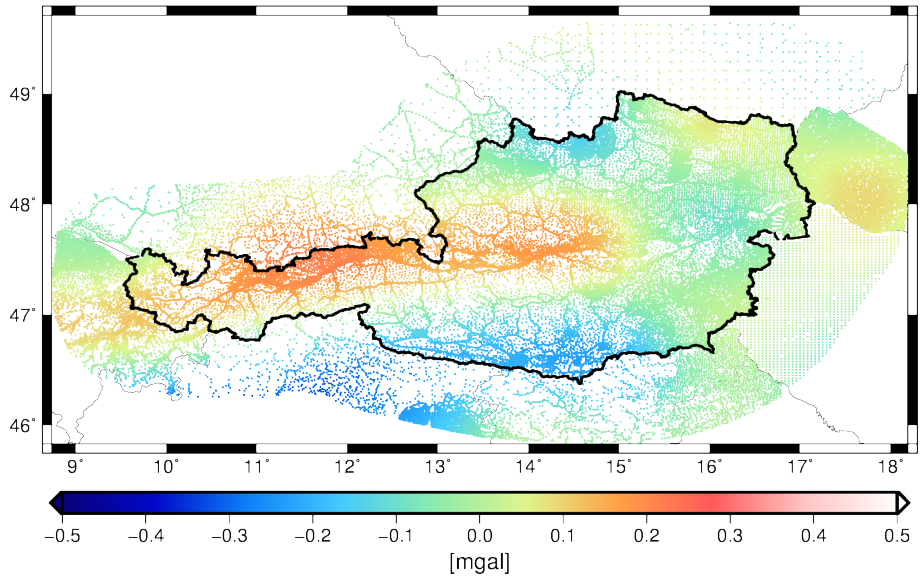

Figure 7.15: Gravity differences between the normal gravity and the GGM gravity

Table 7.12: Statistics of the gravity differences between the normal and the GGM gravity

[mgal]	min	max	mean	rms
$\Delta\Delta g_{red}$	-0.33	0.21	0.01	0.10

Impact of Full Vector Approach for Topographic Effects

This section is investigating the effect caused by using the so-called full vector approach (see sec. 6.2.1) which has priority in this thesis, in comparison to the classical linearization approach which takes only the radial derivation of the potential into account. Furthermore, it has to be noted that both approaches are related to the same approximated GGM geoid height and the difference between these two approaches is connected to the evaluation of the disturbing potential T. The linearized, scalar approach can be written as

$$\Delta g_{red} = g - \|\nabla V^{GGM} + \boldsymbol{g}^{cen}\| + \delta g^{topo} - \delta g^{atm} \quad \text{with} \quad \delta g^{topo} = \frac{\partial T^{topo}}{\partial r} \,. \tag{7.9}$$

In contrast, the full vector approach is given according to Eq. (7.1), where the entire computation is based on vector evaluation which also holds true for the topography according to $\boldsymbol{g}^{topo} = \nabla T^{topo}$. The occurring gravity difference is of about $\pm$ 0.41 mgal as shown in Fig. 7.16.

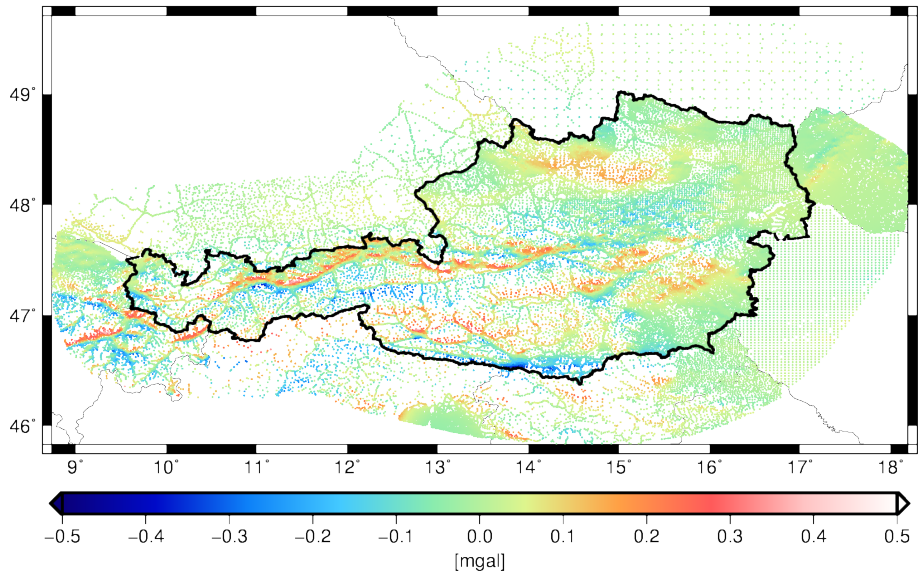

Figure 7.16: Gravity differences between the full gravity vector and linearized approach for topographic effects

Table 7.13: Statistics of the gravity differences of full gravity vector and linearized approach for topographic effects

[mgal]	min	max	mean	rms
$\Delta\Delta g_{red}$	-0.39	0.41	0.01	0.07

Taking this effect into account leads to a more consistent geoid computation and minimized linearization errors, which further contributes to an improved geoid quality, which will be discussed in the following subsection.

Accumulated Effect of Methodological Developments

The effect of a new Taylor point and a different gravity representation as well as the use of the full vector approach lead to slightly different reduced gravity values. These differences are attributed to methodological developments and are shown in Fig. 7.17. The statistics can be found in Tab. 7.14.

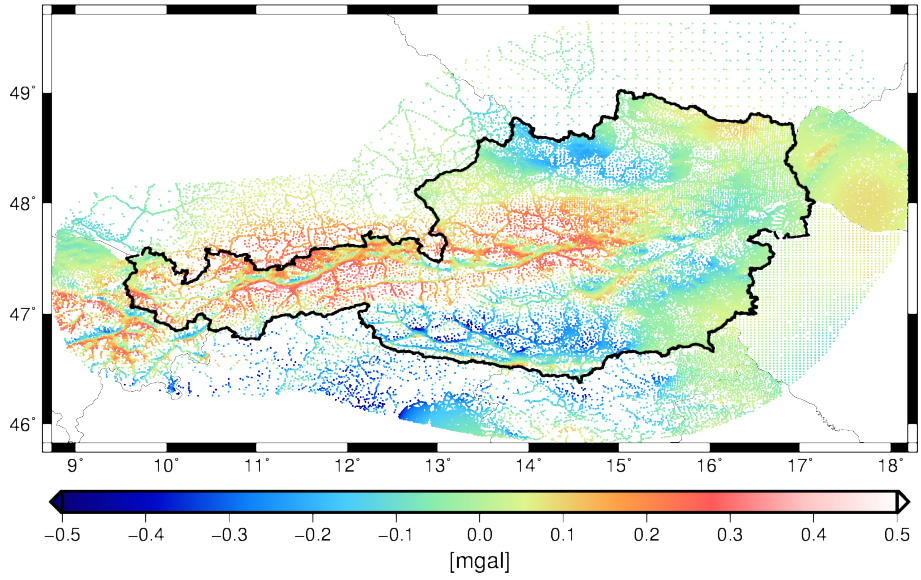

Figure 7.17: Gravity differences of accumulated effects

Table 7.14: Statistics of the gravity differences of accumulated effects

[mgal]	min	max	mean	rms
$\Delta\Delta g_{red}$	-0.54	0.53	0.01	0.12

The reduced gravity differences are propagating throughout the entire geoid computation which is shown in Fig. 7.18. The corresponding statistics is presented in Tab. 7.15.

Table 7.15: Statistics of occurring geoid height differences caused by accumulated effects

[cm]	min	max	mean	rms
ΔN	-0.78	0.86	0.04	0.38

In order to state about the influence and the benefits of the considered effects, a validation with independent GPS/leveling observations is carried out after the short and long wavelength parts have been restored. If all effects are considered and additionally the 2D surface density information is taken into account, finally a rms value of 2.75 cm can be achieved for the geoid validation (see also sec. 7.3.2), whereas the classical approach with constant density assumption leads to a variation of 3.07 cm. A geoid quality improvement of about 4 mm in comparison to the classical approach is achieved, which corresponds to an approximately

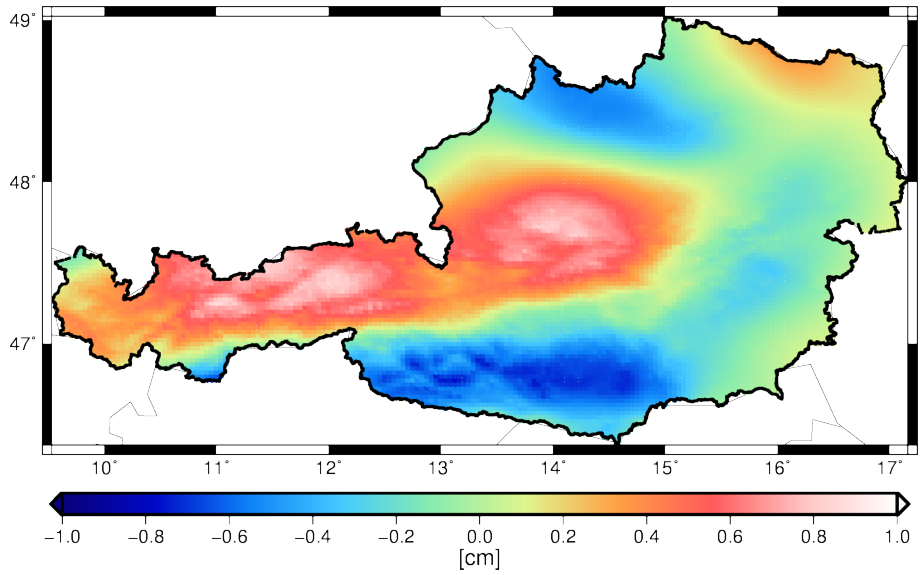

Figure 7.18: Geoid height differences of accumulated effects

11% decreased rms value. Therefore, it could be demonstrated that even small effects may contribute to an improved geoid solution.

7.4.2 Effect of Different Density Information

The focus of this investigation is on the effect caused by different density information and their contributions to an improved gravity field estimation. As discussed in sec. 4.4, several types of density assumptions are available. For the geoid solutions which are shown in previous sections of this thesis, the 2D surface density assumption is considered. This investigation will reveal the benefit of this model. Nevertheless, proof is now required regarding which of these assumptions is suitable for the Austrian geoid determination, in order to make a recommendation for future projects. In particular, the following models are investigated:

- Constant standard crustal density
- Hybrid density model
- 2D surface density model

In previous Austrian geoid computation, a constant standard crustal density assumption of ρ=2670 kg/m^3 has been used. The hybrid density model, here denoted as ρ_{hyb} is an attempt to combine the 2D surface density information with seismic measurements for the purpose of geoid computation. Due to the fact that these datasets do not cover the entire central European region, the missing sections are filled with standard crustal density.

For the remove step, the reduced gravity dataset based on the constant standard density assumption has been chosen as reference. The structures and occurring features of the reduced gravity data look similar as already shown in Fig. 7.1. Therefore, in Fig. 7.19a and Fig. 7.19b

only gravity differences to the reference standard density assumption are presented. These differences can reach ± 22 mgal.

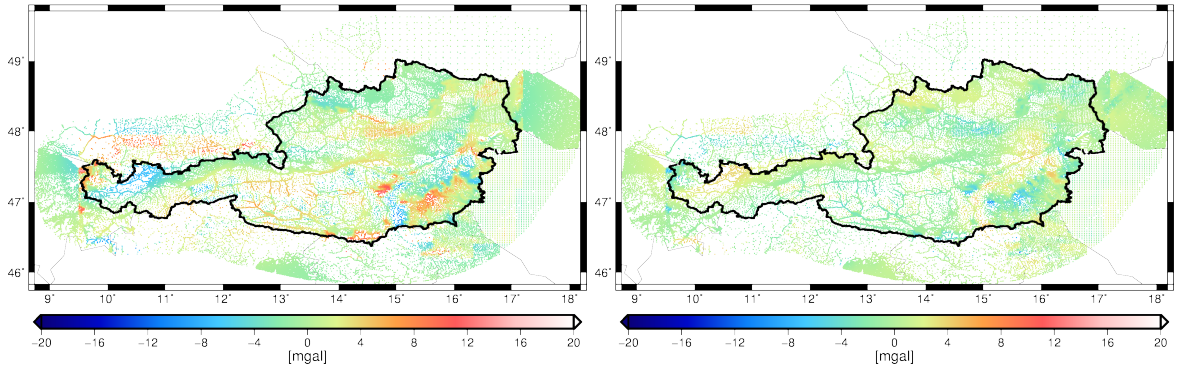

(a) Gravity differences standard vs. surface density (b) Gravity differences standard vs. hybrid density

Figure 7.19: (a) Gravity differences of standard and 2D surface density; (b) Gravity differences of standard and hybrid density

In this research it results that the use of the 2D surface density model, denoted as ρ_{2D}, is beneficial because it provides an additional smoothing to the gravity data. The statistics can be found in Tab. 7.16 and discloses the positive effect of the surface density information on the entire geoid computation process. This information leads to a decreased rms value for the reduced gravity dataset, as well as for the geoid validation with independent GPS/leveling observations which is attributable to a more realistic density assumption of the topography, although the model is only based on geological Earth surface observations which are most likely not valid for deep structures.

Table 7.16: Statistics of reduced gravity and corresponding geoid validation with GPS/leveling observations

[mgal]	min	max	mean	rms
Δg_{red} (ρ)	-48.20	39.91	-0.47	11.72
Δg_{red} (ρ_{hyb})	-47.57	39.31	-0.39	11.54
Δg_{red} (ρ_{2D})	-48.95	37.99	-0.22	11.38
[cm]	min	max	bias	rms
$\Delta GPS/lev.$ (ρ)	-11.68	7.43	-41.65	3.34
$\Delta GPS/lev.$ (ρ_{hyb})	-11.82	7.21	-41.59	3.01
$\Delta GPS/lev.$ (ρ_{2D})	-9.62	6.46	-41.62	2.75

Compared to the two other models, the performance of the standard crustal density model turns out as suboptimal for the purpose of Austrian geoid modeling. Due to the Alps and mountainous regions, as well as different rock types, a model which allows for more variability as the hybrid model seems to be more appropriate. The performance of the hybrid model is in between the surface and the standard crustal density assumption, but in general the 2D surface density assumption performs best compared to GPS/leveling measurements.

7.4.3 Effect of Different DTM Resolutions

In this investigation the impact of different DTM resolutions on the remove and restore step based on a gravimetric geoid solution is discussed. In particular, the following three resolutions are investigated:

- BEV00: 1.40625”×2.34375”
- BEV01: 2.8125”×4.6875”
- BEV02: 5.625”×9.375”

The BEV00 model represents the original resolution, other resolutions denoted as BEV01 and BEV02 are derived from it (see sec. 4.3). In general, the computation steps within the RCR procedure remain the same as described in sec. 7.1.1 and sec. 7.3.2, only the DTM resolution changes. For further DTM background information the reader is referred to sec. 4.3.1.

This investigation shows in an impressive way how the DTM resolution is affecting the reduced gravity data. In Fig. 7.20a the differences between the reduced gravity based on BEV02 and BEV01 resolutions are shown. As can be seen, the differences are strongly correlated with the topographic situation in Austria. This also holds for the differences between BEV01 and BEV00 which are also achieved during the remove step as shown in Fig. 7.20b. The statistics is presented in Tab. 7.17. Consequently, it is still information coming from a denser DTM resolution, which indicates that the highest available DTM resolution is insufficient because the results differ.

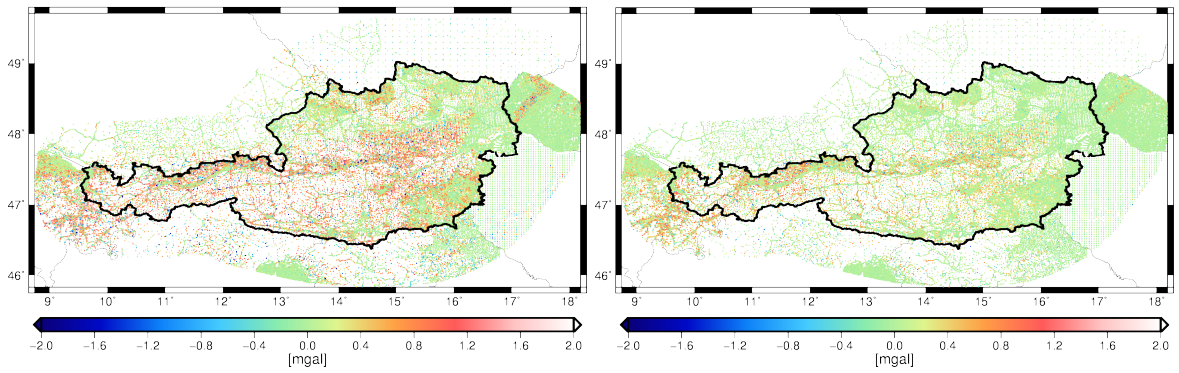

(a) Differences in reduced gravity

(b) Differences in reduced gravity

Figure 7.20: (a) Differences in reduced gravity data caused by DTM resolutions BEV02-BEV01; (b) Differences in reduced gravity data caused by DTM resolutions BEV01-BEV00

Table 7.17: Statistics of reduced gravity differences caused by different DTM resolutions

[mgal]	min	max	mean	rms
$\Delta\Delta g_{red}$ BEV02-BEV01	-3.10	3.37	0.24	0.60
$\Delta\Delta g_{red}$ BEV01-BEV00	-1.80	1.97	0.10	0.27

For the restore step it turns out that the geoid, derived from the topographic part of Eq. (7.6), is independent of the chosen DTM resolution. Therefore, the effect of the remove step is not fully compensated during the restore step and the remaining short wavelength topographic part beyond d/o 250 denoted as δN^{topo} is almost unchanged although different DTM resolutions are considered (see also sec. 6.4). Within the restore step the occurring geoid height changes are on the sub millimeter level and can been neglected as shown in Fig. 7.21.

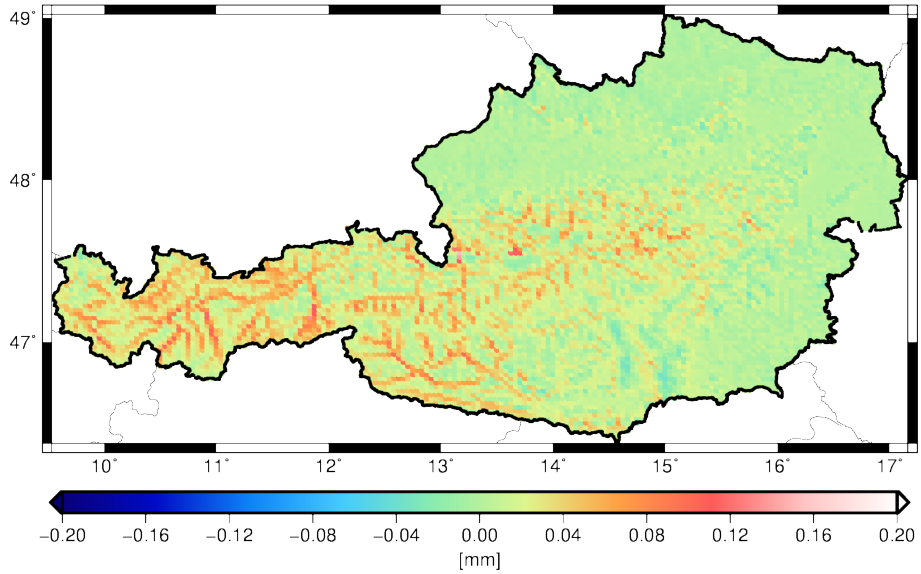

Figure 7.21: Geoid height differences within the restore step computed by subtracting the topographic part based on BEV00 resolution with the part derived from the BEV02 resolution

Hence, the only reason why the resulting geoid heights are slightly varying are attributable to reduced gravity differences achieved from different DTM resolutions within the remove step. These differences are directly propagating in the geoid solution. The corresponding geoid height changes for the BEV02-BEV01 resolutions are shown in Fig. 7.22a. The differences located near the Austrian borders are caused by the sparse gravity observation situation in this regions. This in turn increases the variability of the geoid height in those special areas which holds true especially for the boarder to the Czech Republic. Furthermore, the occurring geoid height differences between the BEV01 and the high resolution BEV00 are small but still present as shown in Fig. 7.22b. The corresponding statistics is presented in Tab. 7.18.

Table 7.18: Statistics of geoid height differences caused by different DTM resolutions

[cm]	min	max	mean	rms
ΔN BEV02-BEV01	-4.27	3.29	0.82	1.45
ΔN BEV01-BEV00	-1.56	1.78	0.35	0.62

This investigation indicates that a higher DTM resolution provides additional information to the gravity field computation process. In contrast, taking into account the BEV00 resolution, the absolute geoid validation with GPS/leveling observations do not show a significant geoid

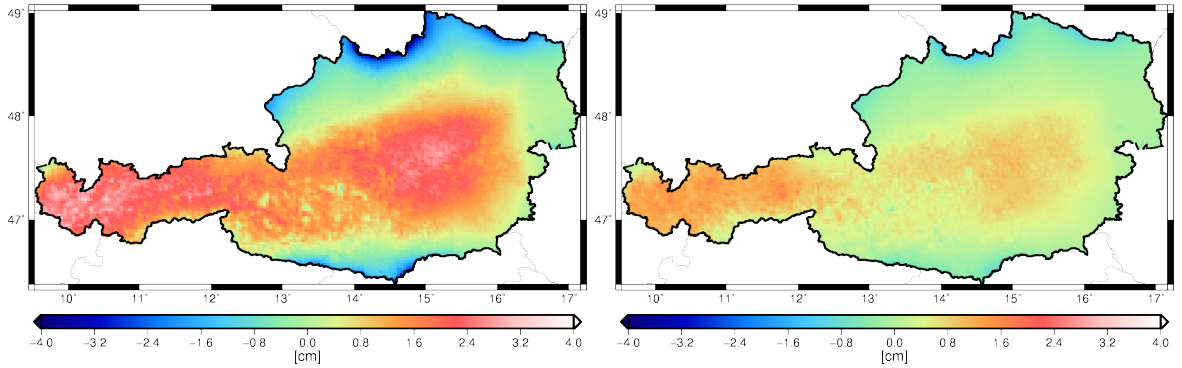

(a) Differences in geoid height BEV02-BEV01 (b) Differences in geoid height BEV01-BEV00

Figure 7.22: (a) Differences in geoid heights based on DTM resolution (BEV02-BEV01); (b) Differences in geoid heights based on DTM resolution (BEV01-BEV00)

improvement. Finally, it turns out that the highest possible DTM resolution does not automatically provide the best geoid solution in comparison to GPS/leveling observations and this indicates that the accuracy of the DTM is likely insufficient. Considering the BEV02 and BEV01, which are generalized from the BEV00, the corresponding DTM height errors are also generalized. Finally, this leads to the same geoid quality. Furthermore, the use of the BEV00 includes more than 650 Mio. DTM points and leads to computational efforts.

7.4.4 Effect of Distant Topographic Masses

For Austrian geoid computation a DTM model which covers the central European region as described in sec. 4.3 is usually considered. The masses and the corresponding topography beyond are neglected. In order to quantify the effect of these truncated terrain model, a global DTM coverage, by means of the GTOPO model (see sec. 4.3.2), has been taken into account. Furthermore, this model is combined with the Austrian DTM so that occurring differences may be interpreted as additional signal coming from the remote masses. Initially, the computation and the RCR procedure are carried out once with and once without these additional masses. They are considered as point masses in the computation due to their large distance from the gravity stations and also a constant standard rock density of $\rho = 2670\ kg/m^3$ is assumed due to the lack of more suitable information.

The occurring differences in the reduced gravity data as well as in the computed final geoid are shown in Fig. 7.23. It has to be pointed out that during the RCR procedure all topographic masses are treated according to sec. 6.2.3 and sec. 6.4.2 in order to avoid a spectral overlap. This is valid for the near as well as for the distant masses based on the GTOPO model. Therefore, analogously to the central European region a set of topographic potential coefficients is also computed for the distant GTOPO covered zones. The difference plot of the reduced gravity data in Fig. 7.23a, shows the remaining components beyond d/o 250 caused by the GTOPO model.

The additional masses are restored after the residual geoid is computed and therefore the impact, which can be clearly identified in the reduced gravity data, is almost compensated and vanishes in the fully restored geoid. Only a rather small effect in the range of few millimeters remains in comparison to the result achieved by only taking into account the central European region. This effect is shown in Fig. 7.23b and does not lead to a significant improvement of the geoid computation. The statistics can be found in Tab. 7.19.

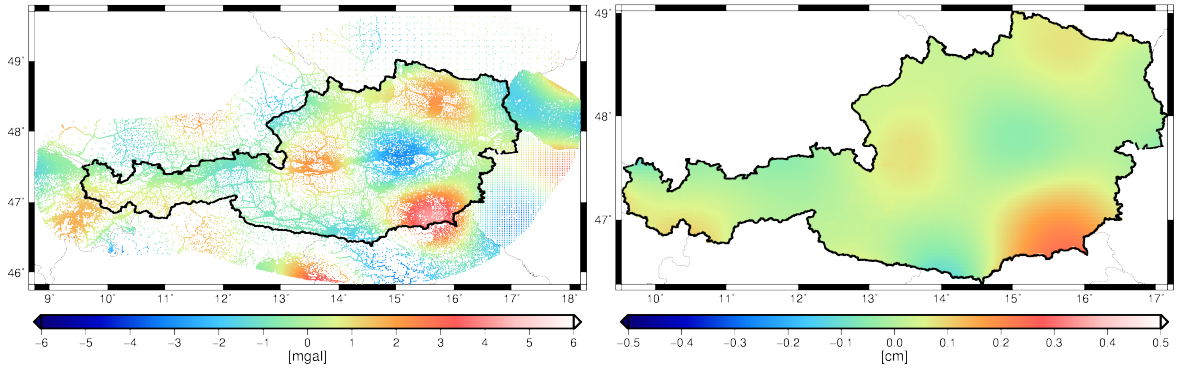

(a) Gravity differences caused by distant zones (b) Remaining geoid differences after full restore step

Figure 7.23: (a) Differences in reduced gravity caused by additional masses; (b) Corresponding remaining geoid height changes after full restore step

Table 7.19: Statistics of differences in reduced gravity data due to the consideration of a global DTM and remaining effect in geoid heights after full restore step

[mgal]	min	max	mean	rms
$\Delta\Delta g_{red}$	-3.58	4.20	0.00	1.23
[cm]	min	max	mean	rms
ΔN	-0.11	0.24	-0.03	0.05

7.4.5 Effect of Different RBF Shapes

This investigation deals with the question whether the chosen RBF shape, which is implicitly defined by means of degree variances as well as error degree variances of a GGM, is appropriate for the purpose of regional geoid modeling. As discussed in sec. 6.3.3, the idea behind this approach is originally based on *(Eicker, 2008)* who first introduced signal degree variance errors, for RBF shape giving purposes. Such global models are limited in terms of d/o, therefore beyond the maximum chosen d/o Kaula's rule of thumb (see Eq. (6.35)) is used to approximate higher signal degree variances. In this thesis a spatial distance of approximately 2×2 km between the RBFs is needed, which corresponds at least to a degree of 9000 (see sec. 6.3.4). In general, Kaula's rule of thumb is valid on a global scale, but the area of interest is restricted to the central European region. Therefore, it is worthwhile to investigate different RBF shape assumptions in the higher degrees, which have been presented in Fig. 6.13.

As shown in sec. 6.3.3, an alternative approach leads to two different assumptions of the RBF shapes which are denoted as Kaula 2 and Kaula 1. The latter approximates the EGM2008 signal degree variances *(Pavlis et al, 2008)* or *(Pavlis et al, 2012)* up to d/o 2160. Beyond d/o 2160 a steady progress of the curve is assumed. The second assumption, which is denoted as Kaula 2, represents a more flattened progress from d/o 250 up to d/o 9000. These investigation only effects the estimation of the residual geoid but to enable the possibility for absolute geoid validation, the full restore step has been carried out.

Nevertheless, the achieved geoid results and comparisons lead to similar output, mainly independent of the shape as shown in Fig. 7.24. In comparison to the official Austrian geoid solution, prominent features in the central part of Austria are still visible (see sec. 7.3.2) but the Kaula 1 assumption is not as pronounced as Kaula 2. Nevertheless, the results are similar to the standard Kaula approach, which is confirmed to be used for all other geoid computation (see sec. 7.2).

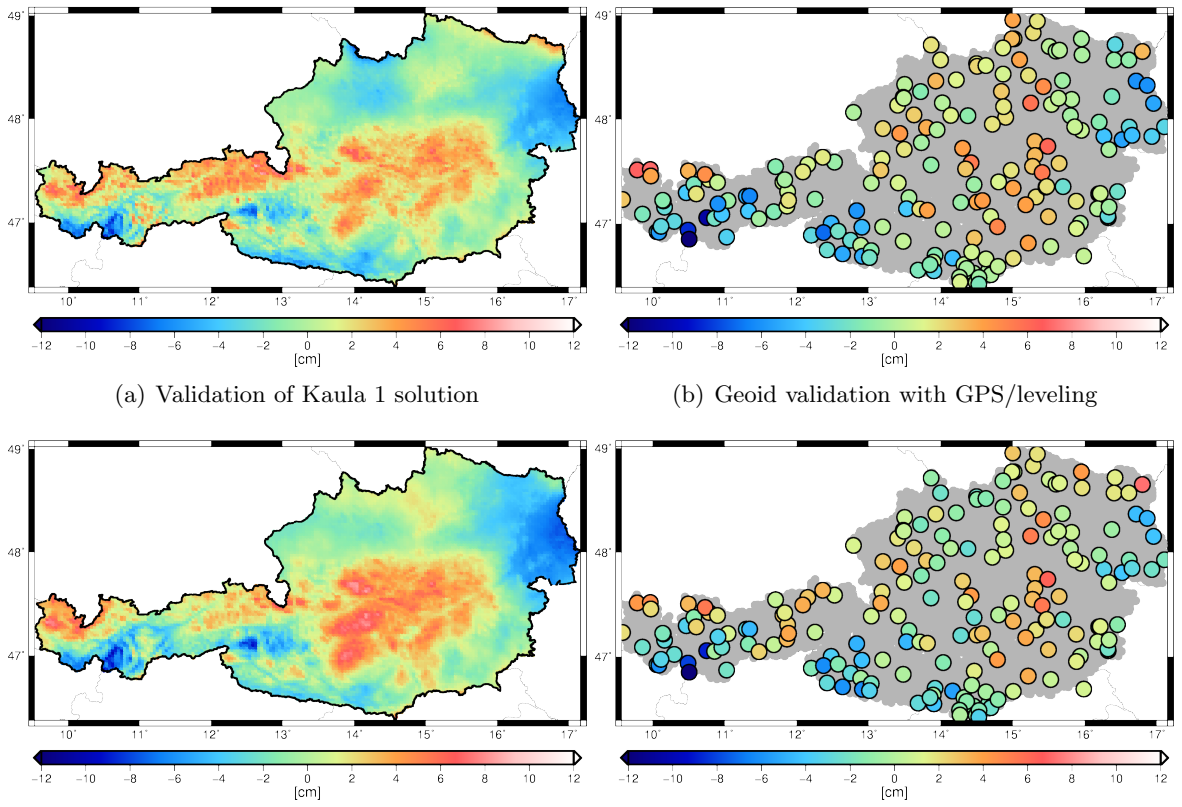

(a) Validation of Kaula 1 solution

(b) Geoid validation with GPS/leveling

(c) Validation of Kaula 2 solution

(d) Geoid validation with GPS/leveling

Figure 7.24: (a) & (c) Validation of Kaula 1 and Kaula 2 in comparison to the official Austrian geoid; (b) & (d) Corresponding geoid validation with GPS/leveling observations

Furthermore, absolute geoid validation with independent GPS/leveling measurements show similar results. Consequently, the standard definition of Kaula's rule of thumb is also suitable to represent degree variances and the corresponding RBF shape on a regional scale. Variations

Table 7.20: Statistics of geoid validation with GPS/leveling observations and with the official Austrian geoid N_{2007}

[cm]	min	max	bias	rms
$\Delta GPS/lev.$ (Kaula 1)	-12.33	7.22	-41.59	2.96
$\Delta GPS/lev.$ (Kaula 2)	-12.58	7.06	-41.48	3.15
ΔN_{2007} (Kaula 1)	-9.20	9.15	-41.13	2.72
ΔN_{2007} (Kaula 2)	-9.91	8.57	-41.08	3.08

of the RBF shape in the higher degrees do not lead to significantly different results. The statistics is presented in Tab. 7.20.

7.4.6 Effect of Amount of Incorporated Gravity Field Quantities

This section provides an insight on the effects caused by the amount of gravity data used and the resulting gravimetric geoid in comparison to deflections of the vertical and the astrogeodetic geoid solution. The entire investigation is driven by the question whether the information content of these two gravity field quantities is comparable for the purpose of geoid computation or if one quantity is preferable to the other. To answer this question, which came up in sec. 7.3.3, the amount and spatial distribution is chosen similarly for both quantities. This represents an important requirement for this investigation.

In fact there are 735 deflections of the vertical with North-South and East-West orientation available. For each deflection component the number of gravity data is similar with randomly chosen 1446 observations as shown in Fig. 7.25a. This provides almost a one by one ratio, which is important to enable the opportunity to compare two gravity field quantities on the geoid level. Furthermore, about 3.5 times more gravity observations (5294 observations) are used for a second investigation, taking into account an unbalanced ratio, which clearly favors the gravity data as shown in Fig. 7.25c. This number has been chosen empirically in order to view the improvements in comparison to the GPS/leveling data. In general, the computation parameters and all used models are chosen equivalent to the astrogeodetic solution, which is presented in sec. 7.2.2, so that occurring differences are only attributable to the number of observations which are taken into account.

As supposed in sec. 7.3.3, the superior information content of deflections of the vertical, in comparison to gravity data, is now proven. The statistics is presented in Tab. 7.21 and reveals that the gravity subset which consists 1446 observations leads to a final geoid variability of 5.81 cm, whereas for the astrogeodetic geoid solution the rms value is 4.92 cm (see again sec. 7.3.3). This indicates that if the amount and spatial distribution of gravity data, as well as deflections of the vertical are similar, the latter performs better in comparison to the absolute validation with independent GPS/leveling observations.

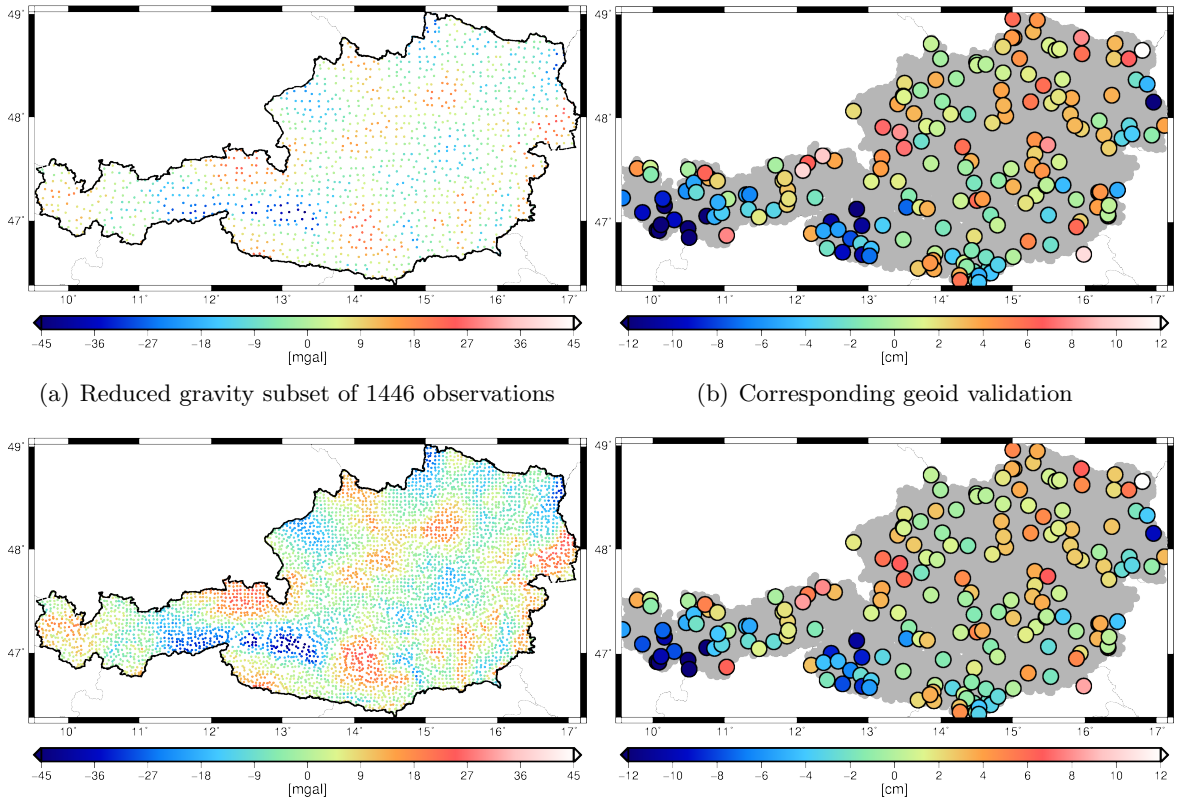

(a) Reduced gravity subset of 1446 observations

(b) Corresponding geoid validation

(c) Reduced gravity subset of 5294 observations

(d) Corresponding geoid validation

Figure 7.25: (a) Reduced gravity subset Δg_{red} which corresponds to the amount of deflections; (b) & (d) Corresponding geoid validation with GPS/leveling observations; (c) Reduced gravity subset Δg_{red}, which ensures a similar geoid quality in comparison to the astrogeodetic solution

As a result, at least three times more gravity data need to be considered in order to ensure the same geoid quality, which is visualized in Fig. 7.25d. The structures and features of the reduced gravity data in Fig. 7.25c now become more apparent in comparison to the final reduced gravity dataset within Austria, which is shown in Fig. 7.1. Finally, the validation of these input dataset including 5294 observations leads to a decreased variability of 4.43 cm, which is comparable to the quality of the astrogeodetic geoid solution.

For further Austrian geoid projects it is recommended to collect and include any newly measured deflections of the vertical for the purpose of gravity field determination. Currently only sparse deflections of the vertical are available, but as shown in this investigation their information content is higher in comparison to gravity data and less observations are needed to achieve results on the same quality level.

Table 7.21: Statistics of the reduced gravity subsets and corresponding geoid validation

[mgal]	min	max	mean	rms
Δg_{red} (1446 observations)	-45.98	31.61	-0.51	11.80
Δg_{red} (5294 observations)	-50.06	31.89	-0.56	11.59
[cm]	min	max	bias	rms
$\Delta GPS/lev.$ (1446 observations)	-20.13	17.14	-44.58	5.81
$\Delta GPS/lev.$ (5294 observations)	-16.50	14.05	-42.26	4.43

7.4.7 Effect of Isostasy

In this investigation it could be demonstrated that the isostatic component is well covered by a global GGM and that residual isostatic parts beyond the maximum d/o of the GGM do not contribute to a significant geoid improvement and are almost compensated during the RCR procedure. To prove this statement, the impact on remove and restore steps are investigated. For the topographic part a constant standard crustal density assumption of $\rho = 2670\ kg/m^3$ and a corresponding constant density contrast of $\Delta\rho = 350\ kg/m^3$ is considered. It has to be noted that for this single investigation the atmospheric part is neglected because this effect may be assumed as not important for the investigation of the isostasy.

In Tab. 7.22 the final impact of the residual isostatic part for the remove step is shown. Considering the isostasy leads to slightly increased minimum and maximum values and the variability, expressed as rms value, is also increased. This indicates that the isostatic component is indeed well covered and represented by means of a GGM, if the chosen maximum d/o of the series expansion is sufficient. Furthermore, the isostatic compensation is based on several assumptions with regard to density contrast or compensation depth which can not be proven in reality. For the purpose of gravity field estimation on a regional scale, the replacement of isostasy by means of a GGM can be viewed very positively in every respect, because it contributes to remove assumptions during the computation process, which in turn improves the entire gravity field computation.

Table 7.22: Statistics of 72327 reduced gravity observations, once with and once without isostasy from d/o 251 $\rightarrow$ 500

[mgal]	min	max	mean	rms
Δg_{red}	-48.49	39.45	-1.11	11.69
Δg_{red} with iso.	-50.67	42.58	-1.19	11.74

For the purpose of geoid validation, the residual isostasy is also considered within the restore step. Slight differences in the final geoid heights occur and the corresponding validation is shown in Tab. 7.23. However, neglecting the remaining isostatic effect beyond d/o 250 leads to better results in comparison to GPS/leveling observations. One may conclude that by

applying the additional effect of short wavelength isostasy an overcompensating behavior is introduced, which slightly degrades the geoid solution.

Table 7.23: Statistics of geoid validation with GPS/leveling observations; Once with and once without isostasy considered from d/o 251 → 500

[cm]	min	max	mean	rms
$\Delta GPS/lev.$	-11.68	7.43	-41.65	3.34
$\Delta GPS/lev.$ with iso.	-12.91	8.11	-41.66	3.60

7.5 Estimated Maps of Deflections of the Vertical

Based on the reduced gravity dataset which is described in detail in sec. 7.1.1, maps representing deflections of the vertical are estimated. are estimated. This means that the computation is again based on the full vector approach and also the 2D surface density information as well as the GOCO05s are considered whereas the computation method is described in sec. 3.5.3. The deflections of the vertical are predicted on the Earth's surface, which in turn requires height information provided by a dense DTM (BEV02). The general aim of this approach is to provide a gridded map of deflections of the vertical, which can be used for interpolation of new deflection values without being dependent on a new computation. Therefore, a dense grid of deflections (< 200 m) is needed in advance, in order to keep the interpolation errors small. These maps which finally consist of about 2.5 Mio. individual deflections are shown in Fig. 7.26 and Fig. 7.27, respectively.

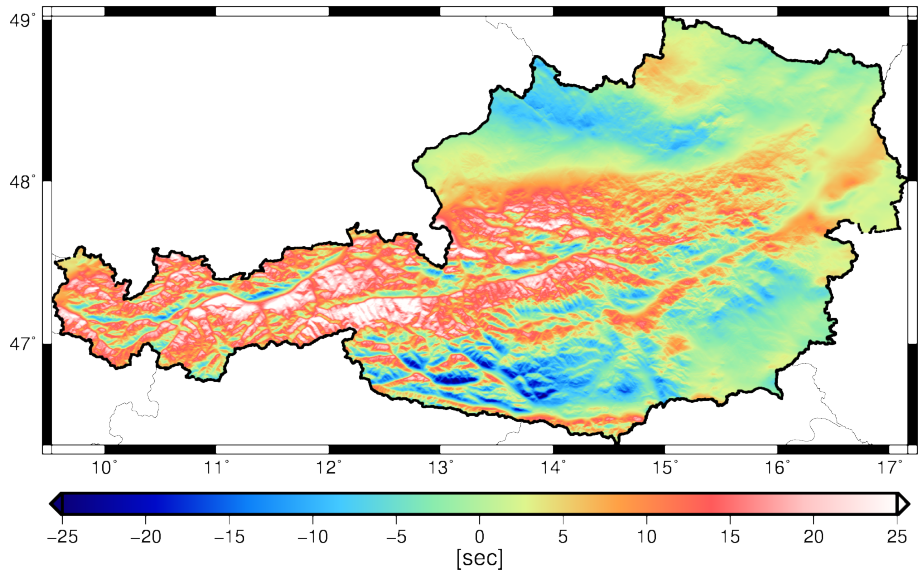

Figure 7.26: Map of North-South direction

One of the characteristics of deflections is that they are more sensitive to horizontal than to vertical mass anomalies. This is the reason why valleys and corresponding masses with

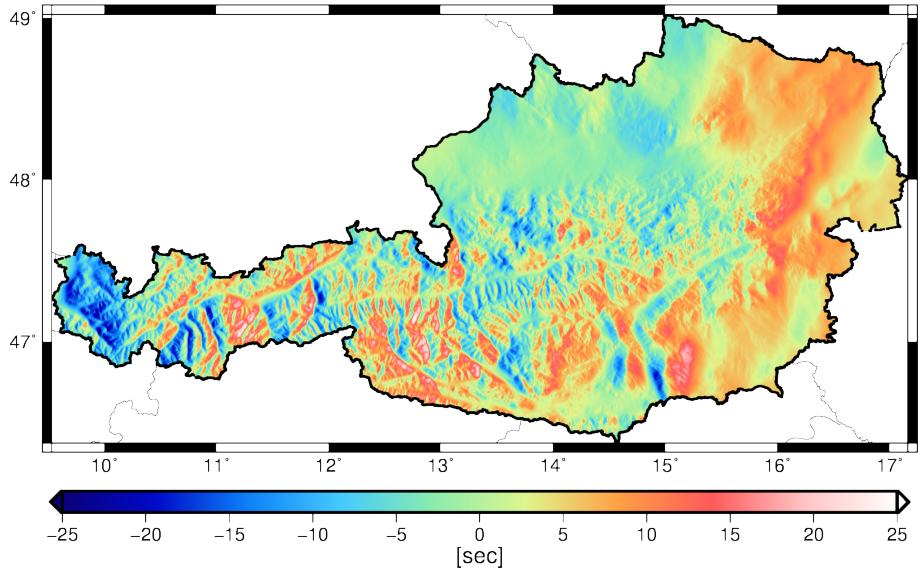

Figure 7.27: Map of East-West direction

East-West orientation clearly show up in the ξ component, and valleys with North-South orientation in the η component. This can be clearly seen in the two maps. Masses with other spatial orientation appear in both components. The validation of these maps is conducted by means of a comparison of estimated and real measured deflections. This in turn is also an additional validation of the full vector approach and the entire reduced gravity data set, because only gravity data are taken into account for the estimation. The validation results show a remaining variation of 0.50" for the ξ component and 0.61" for the η component, which indicates a high quality for the estimated maps (see Tab. 7.24). A significant characteristic of the validation result is a remaining mean value or bias, especially in the η component. One reason for this is related to time measurements, which are especially required for the determination of the East-West orientated deflection component (see sec. 4.2.2). Most of these 735 measurements are taken before the GPS system time was available and therefore the time stamps were not as accurate as nowadays, which can cause such a bias. In comparison with up to date zenith camera measurements, provided for the Semmering tunnel project, the validation shows a much more homogeneous behavior and rms values < 0.5" but only a few observations are available.

Table 7.24: Statistics of the gridded map values and corresponding validation with 735 measured deflections of the vertical

[sec]	min	max	mean	rms
ξ	-26.09	38.65	3.67	8.73
η	-26.57	25.72	1.51	6.48
$\Delta\xi$	-2.05	1.93	0.10	0.50
$\Delta\eta$	-1.71	1.82	0.35	0.61

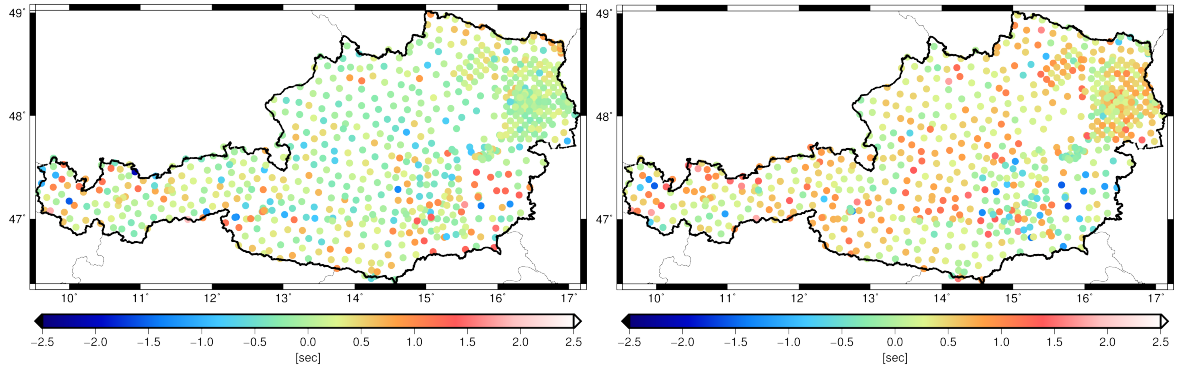

(a) Validation of ξ component

(b) Validation of η component

Figure 7.28: Validation of the estimated maps of deflections

8 Summary and Recommendations

One of the main goals of this thesis, to compute an unconstrained gravimetric geoid solution on the same accuracy level as the official Austrian geoid, has been achieved. Furthermore, several problems resulting in inconsistencies between a gravimetric geoid and GPS/leveling observations could be overcome and a fit to GPS/leveling observations by means of a non-physical correction surface is no longer required. Therefore, several improvements concerning the combination of global satellite and terrestrial data within the Remove-Compute-Restore (RCR) procedure and a minimized number of assumptions in the computation are required. The major part of the methodological progress is attributed to a rigorous spectral separation of different wavelength components of the gravity field signals in the RCR procedure. The long wavelengths up to d/o 250 are only represented by a Global Gravity field Model (GGM). Beyond this level a high resolution Digital Terrain Model (DTM) is used to represent mainly the short wavelengths. Furthermore, it could be demonstrated that due to this approach the isostatic component, which is based on several assumptions, could be avoided in the computation because its long wavelength characteristic is already covered by a GGM up to d/o 250. The atmospheric potential is represented by the ITSG density model. This accounts for the fact that gravity data are located within the attracting masses because the atmosphere is considered to be above the terrestrial observations. Another improvement is attributed to the transition from the ellipsoid reference surface to a geoid representation, which is valid on a global scale and provides a more realistic Taylor point for linearization purposes. The corresponding normal gravity field has also been exchanged by means of a GGM gravity representation.

The computation of the **gravimetric geoid solution** is based on 72327 gravity measurements. For the remove step, the full vector approach is applied. Hence, the absolute magnitude of the gravity acceleration is computed for each gravity vector and is subtracted from every single gravity station in order to obtain gravity anomalies. The long wavelength component is represented by the latest GOCO model, the GOCO05s up to d/o 250, whereas the short wavelengths are predominately based on a dense DTM representation. With the inclusion of 2D surface density information which replaces the standard crustal density assumption an additional step towards an improved geoid quality has been completed to realize the idea of orthometric heights, derived from the Global Navigation Satellite System (GNSS), which is expected to replace classical geodetic spirit leveling in future. In order to consider gravity a-priori accuracy information, the dataset is divided into several observation groups. Within Austria three groups, based on different measurement systems are established. The remaining gravity data outside Austria is split according to Austria's neighbouring countries, which lead to seven additional groups and finally a total of ten observation groups. Taking into account

the regularization, one additional group for the regularization parameters, which are set up for all unknown parameters, is required. The used least squares approach with Radial Basis Function (RBF) parametrization is utilized for the first time for the purpose of Austrian geoid computation. The Variance Component Estimation (VCE) method provides the relative weighting among ten observation groups and the regularization parameters. Concerning the spatial distribution of the RBFs, which represent the gravity field signal, a triangle vertex representation with a spatial resolution of about 2×2 km is sufficient to cover all possible cases of gravity field estimation within this research. In order to provide the opportunity to validate the different achieved gravity field solutions, all remove steps are reversed and long- short, as well as atmospheric components, have been restored. The validation of the gravimetric geoid solution shows a remarkable quality for validation with the official Austrian geoid, which is provided on a grid, as well as the for the validation with geopotential numbers. The comparison to 192 independent GPS/leveling measurements and the national Austrian geoid solution finally reveals a rms value < 3 cm. Due to the fact that the general absolute accuracy of these measurements is unknown, it can be stated that the computed solution is at least on the same accuracy level. Furthermore, prominent features located in the central part of Austria in comparison to the national geoid occur, but it was not possible to give a reliable statement whether these features belong either to the official Austrian geoid or to the present geoid solution.

For the computation of the **astrogeodetic geoid solution**, 735 deflections of the vertical are considered. The computation configuration is in principle the same as for the gravimetric geoid. The difference being that the computed deflections are taken from the first two components of the gravity vector, representing the deviation from the local plumb line. The computation is based on only one observation group and the regularization is in general stronger, due to less observations. Although there are only a few observations available, in comparison to the gravity dataset, the astrogeodetic geoid solution displays an unexpected quality level in comparison to GPS/leveling measurements as well as with the official Austrian geoid. Both comparisons finally provide a rms value < 5 cm, which indicates superior information content of deflections of the vertical in comparison to gravity data.

The **combined geoid solution** consists of 72327 gravity measurements, and 735 deflections of the vertical. Once more, the computation setup is chosen according to the pure gravimetric geoid, with the difference that the deflections are introduced as an additional observation group. Due to the huge amount of gravity data, the solution is dominated by this gravity field quantity. The contribution of 735 deflections of the vertical to a combined geoid solution is rather small. Also the validation with GPS/leveling observations, as well with the official Austrian geoid solution shows in principal the same results as the pure gravimetric solution. Further investigations show that both solutions are equivalent in terms of geoid height, except for the regions bordering the Czech Republic and some alpine regions in Austria, where only sparse gravity observations are available. Nevertheless, this is not significant for the absolute geoid validation. Therefore, the quality of both solutions are also assumed to be equivalent and the rms is < 3 cm.

The results of **several investigations** and important findings related to the geoid computation have also been part of this research. First, methodological developments including the implementation of the full vector approach in combination with the inclusion of the GOCO05s as a reference field, in order to reduce linearization errors and to use a more realistic Taylor point are discussed. It could be shown, that the cumulative effects result in a slightly smoother input gravity dataset and also the resulting rms value for the absolute geoid validation with GPS/leveling observations slightly improves in the range of about 4 mm compared to the classical approach. This corresponds to a 11% decreased rms value. Furthermore, this approach is also important to provide approximated ellipsoidal heights for the spherical harmonic expansion of the DTM. Summarized, this approach provides a methodological improvement, which is recommended to be taken into account for future Austrian gravity field projects.

The next investigation is dealing with the use of **different types of density information**. Therefore, three different assumptions have been compared. The inclusion of the 2D standard crustal density, which is based on geological observations and therefore strongly correlated to rocks and geological composition within Austria, provides in the best geoid solution when compared to all validation possibilities. To include such information in the computation process is beneficial twofold. First, the reduced gravity dataset is smoothed additionally. Secondly, the final geoid outcome also shows a significant improvement in comparison to the standard crustal density assumption, which results in a decreased rms value. Therefore, if this type of density information is available it is recommended to incorporate it.

The effect of **different DTM resolutions** is also investigated. It is shown that in a subsequent densification of the DTM, starting from the coarse BEV02 resolution towards the BEV00, which provides the highest available spatial resolution a change in the reduced gravity data occurs. This indicates that still information is provided from a higher resolution and therefore a denser DTM is needed. The change of reduced gravity caused by different DTM resolutions is directly propagating into a residual geoid change of a few centimeters. In contrast, the remaining topographic short wavelengths geoid heights computed within the restore step are independent of the chosen DTM resolution, which is also shown in this investigation. Consequently, a part of the signal is removed due to the fine DTM resolution, but not restored afterwards. This is one explanation why the gravity smoothing is slightly improved with increasing DTM resolution, but this does not affect the absolute validation of the geoid in a significant way. The achieved geoid validation rms values for BEV00, BEV01 and BEV02 remain more or less the same, which was not expected. The BEV02 and BEV01 are generalized, from the dense BEV00 resolution, and therefore also the DTM height errors are generalized. This is one explanation why the absolute geoid validation considering the highest available DTM resolution does not automatically provide the best geoid result. Furthermore, the use of the BEV00 resolution leads to intense computational efforts.

The next investigation deals with the effect caused by **distant topographic masses** outside the central European region, represented by means of a global DTM coverage. These distant masses are almost compensated during the RCR procedure and the remaining effect is only on

the 2 mm level in terms of geoid heights. Furthermore, an improvement of the geoid quality by comparing it with independent GPS/leveling observation is not observed. Therefore, these masses can be neglected and the extended regions do not provide a significant contribution to a regional geoid quality improvement.

The general result from **different RBF shape approaches** used for the higher degrees variances beyond d/o 250, which control the RBF shape, is confirmed as the standard Kaula's rule of thumb. A slight different continuation of the RBF shape leads only to sub-centimeter geoid height changes and the prominent features in comparison to the official Austrian geoid do not vanish. In addition, the absolute geoid validation shows similar rms vales in comparison to the standard Kaula method. Therefore, it was proven that for the shape giving aspect of the RBF, Kaula's rule of thumb, which is originally defined on a global scale, is also suitable for a more regional representation, as it is the case for the Austrian geoid computation.

The next of the selected investigations deals with a **different amount of input data** and proves that deflections of the vertical are of superior information content, compared to gravity data. As could be demonstrated, at least three time more gravity data are required to ensure the same geoid quality, based on absolute geoid validation with independent GPS/leveling observations. This statement is valid if the spatial data distribution and the computation setup remains unchanged between the gravimetric and the astrogeodetic geoid solutions. If the ratio between these two observations is equal, the astrogeodetic geoid solution provides a better quality.

It also could be shown that the **effect of isostasy** is well covered by a GGM representation if the corresponding maximum d/o is chosen sufficiently. This is due to the fact that in principle both effects cover predominately the same long wavelength range of the spectrum. Therefore, a significant level of uncertainty is avoided within the RCR procedure because the isostatic concept is based on several assumptions.

Furthermore, **dense maps of deflections of the vertical** are estimated. The computation is based on the 72327 reduced gravity measurements which provide the basis for the estimated solution vector of RBF scaling coefficients. The deflections can be computed on every arbitrary point and as an input only geodetic coordinates in combination with an orthometric heights are needed. The BEV02 resolution is therefore directly ready to provide the basis for a dense map of either the ξ or η component of deflections of the vertical, without excessively computational efforts. These dense spatial distribution enables the opportunity to simply interpolate new deflections of the vertical. The validation of the estimated maps with 735 measured deflections of the vertical show rms values < 0.61" for both components. A comparison to more up to date zenith camera measurements shows a higher level of agreement, but only a few observations are available. Such an approach can not replace present zenith camera measurements, but provides an alternative method for the prediction of deflections, if only a lower level of accuracy is required.

A **general problem** which is related to the used validation points and models is also discussed. The major geoid validation has been performed with GPS/leveling observations, but the Federal Office of Metrology and Surveying (BEV) does not provide reliable accuracy information of these measurements. They are only assumed to be accurate on a few centimeter level. Furthermore, due to a complete re-evaluation of the GPS/leveling observations in the year 2010, the official Austrian geoid 2007 *(Pail et al, 2008)* is inconsistent to these measurements. Moreover, for the density information used in this thesis no quality information is available.

Finally, in the present Austrian geoid initiative (GARFIELD) two **different methods of gravity field estimation** are compared. Within this thesis a least squares approach with RBF parametrization is applied whereas the classical approach of Least Squares Collocation (LSC) has been utilized by *(Rieser, 2015)*. Both methods provide the opportunity to compute high quality geoid solutions. The corresponding PhD theses represent the state of the art of Austrian gravity field modeling.

Abbreviations

ASAP	Austrian Space Applications Programme
BEV	Federal Office of Metrology and Surveying
BKG	Federal Agency for Cartography and Geodesy
CHAMP	CHAllenging Minisatellite Payload
d/o	degree and order
DTM	Digital Terrain Model
FFG	Austrian Research Promotion Agency
FFT	Fast Fourier Transformation
FWF	Austrian Sciences Fund
GARFIELD	Geoid for Austria - Regional gravity FIELD improved
GNSS	Global Navigation Satellite System
GOCE	Gravity field and steady-state Ocean Circulation Explorer
GOCO	Gravity Observation COmbination
GRACE	Gravity Recovery and Climate Experiment
GRS	Geodetic Reference System
GPS	Global Positioning System
GGM	Global Gravity field Model
IAG	International Association of Geodesy
ITSG	Working Group of Theoretical Geodesy and Satellite Geodesy
INAS	Working Group of Navigation
INM	Institute of Numerical Mathematics
ICGEM	International Center for Global Earth Models
LSC	Least Squares Collocation
LCR	LaCoste Romberg
MGI	Militär Geographisches Institut
NASA	National Aeronautics and Space Administration
NRCAN	National Resources Canada
ÖSGN	Austrian Gravity Network
RBF	Radial Basis Function
RCR	Remove-Compute-Restore
rms	root mean square
SLR	Satellite Laser Ranging
SRTM	Space Shuttle Topography Mission

UELN	United European Leveling Network
USSA76	United States Standard Atmosphere Model
USGS	United States Geological Survey
VCE	Variance Component Estimation
WGS	World Geodetic System

List of Figures

1.1 Combination of heterogeneous data within the RCR technique 3
1.2 Example of GROOPS software interface 5

2.1 Level surfaces and plumb lines 7
2.2 General definition of the ellipsoidal height h, the orthometric height H and the geoid height N 8
2.3 Special characteristics of the Austrian height system 12
2.4 National reference levels 14
2.5 Vertical height changes over the last 70 years 15
2.6 Differences between the Austrian height system and the neighbouring counties 15
2.7 Applied height differences ΔH to the gravity stations within Austria based on the BEV transformation grid 16

3.1 Common definition of gravity anomalies 30
3.2 Alternative definition of gravity anomalies 31
3.3 Common definition of the gravity disturbance 32

4.1 GEOnAUT data: gravity measurements (black), deflections of the vertical (blue) and GPS/leveling observations (red) 36
4.2 Official Austrian geoid solution based on the GEOnAUT project 37
4.3 Correction surface given on a 3×3 km grid 38
4.4 GEOID+ dataset: gravity measurements (black), deflections of the vertical (blue) and GPS/leveling observations (red) 40
4.5 GARFIELD data: gravity measurements (black), deflections of the vertical (blue) and GPS/leveling observations (red) 41
4.6 Absolute and relative gravimeter 43
4.7 Gravity accelerations 43
4.8 Differences between gravity station height and the nearest DTM point 45
4.9 Measured 735 North-South ξ components 46
4.10 Measured 735 East-West η components 47
4.11 Digital zenith camera systems for the direct measurement of deflections 48
4.12 Measurement principle of GPS/leveling 49
4.13 192 measured geoid heights provided by the BEV 49
4.14 Changes of the GPS/leveling observations during the period of 2009-2010 initialized by the GEOID+ project 50
4.15 High resolution DTM within central Europe 51

4.16 Global DTM coverage provided by the GTOPO model 53
4.17 2D Austrian density model based on geological observations 54
4.18 Geological map of Austria 55
4.19 Top layer (0 km) of seismic 3D density information 56
4.20 Hybrid density model 57

5.1 The entire gravity dataset is divided into ten different observation groups . . . 65

6.1 Degree variances of several global gravity field models 70
6.2 Remaining short wavelength part of gravity anomalies after long wavelength reduction up to d/o 250 71
6.3 Different approximation approaches of the topography depending on the distance between the gravity station and the DTM point 74
6.4 Geometric situation for a single prism with density ρ 75
6.5 Simple tesseroid representation and approximation by prism 76
6.6 Topographic part beyond d/o 250 78
6.7 Standard Airy-Heiskanen model 79
6.8 Influence of the isostatic part on gravity observations d/o 251 $\rightarrow$ 500 81
6.9 Combined atmospheric signal in terms of gravity anomalies 82
6.10 Set of estimated unitless RBF scaling coefficients 84
6.11 Different normalized RBF kernels; gravity anomaly (left) and geoid height (right) 86
6.12 Transition between the GOCO05s error degree variances and the full signal of the high frequencies using Kaula's rule starting from d/o 251 $\rightarrow$ 9000 87
6.13 Different selected degree variance curves 88
6.14 Triangle vertex grid of 37891 RBFs in the area of interest 89
6.15 Triangle vertex grid of level 3 90
6.16 Geoid heights N^{GGM} based on the GOCO05s model up to d/o 250, covering the long wavelength component of the gravity field 91
6.17 Remaining short wavelength topographic part in terms of geoid heights 92
6.18 Remaining short wavelength part of isostasy in terms of geoid heights 93
6.19 Geoid heights based on the combined atmospheric effect 94

7.1 Reduced gravity dataset Δg_{red} 96
7.2 Reduced North-South ξ_{red} component 97
7.3 Reduced East-West η_{red} component 98
7.4 Estimated gravimetric residual geoid heights and standard deviations 99
7.5 Estimated astrogeodetic residual geoid heights and standard deviations 101
7.6 Differences between gravimetric and astrogeodetic geoid solutions 101
7.7 Estimated combined residual geoid heights and standard deviations 102
7.8 Contributions to a combined geoid solution 104
7.9 Validation of input datasets 105
7.10 Validation of gravimetric geoid solution 107
7.11 Comparisons to EGM2008 derived geoid heights 108

7.12 Validation with geopotential numbers 109
7.13 Validation of astrogeodetic geoid solution 110
7.14 Validation of combined geoid solution 111
7.15 Gravity differences between the normal gravity and the GGM gravity 113
7.16 Gravity differences between the full gravity vector and linearized approach for topographic effects 114
7.17 Gravity differences of accumulated effects 115
7.18 Geoid height differences of accumulated effects 116
7.19 Effect of different density information on gravity 117
7.20 Effect of DTM resolution on gravity 118
7.21 Geoid height differences within restore step for different DTM resolutions . . . 119
7.22 Effect of DTM resolution on the geoid 120
7.23 Effect of distant zone topographic masses on gravity and geoid 121
7.24 Effect of different RBF shapes 122
7.25 Effect of different amounts of input data on gravity and geoid 124
7.26 Map of North-South direction 126
7.27 Map of East-West direction 127
7.28 Validation of the estimated maps of deflections 128

List of Tables

2.1 Parameters of the WGS-84 ellipsoid 11
2.2 Characterization of different height systems 13

4.1 Quality of Austrian gravity data 44
4.2 Statistics of 735 measured deflections of the vertical 47
4.3 Statistics of 192 measured geoid heights 50
4.4 Different DTM resolutions 52
4.5 Statistics of all used density models 57

5.1 Estimated σ compared to the official Austrian geoid solution 64
5.2 Estimated variance factors of the individual observation groups by means of VCE 66

6.1 Statistics of long wavelength reduction of 72327 gravity observations 71
6.2 Statistics of short wavelength part of reduction based on gravity observations . 78
6.3 Statistics of remaining isostatic part of 72327 gravity observations 80
6.4 Statistics of the long wavelength geoid up to d/o 250 91
6.5 Remaining short wavelength topographic part in terms of geoid heights 93
6.6 Statistics of remaining short wavelength isostatic part in terms of geoid heights 93
6.7 Statistics of geoid heights based on the combined atmospheric effect 94

7.1 Statistics of subsequently reduced 72327 gravity observations 95
7.2 Statistics of Austrian gravity data subset 96
7.3 Statistics of 735 reduced deflections of the vertical 97
7.4 Statistics of gravimetric residual geoid on approximately 3×3 km grid 99
7.5 Statistics of astrogeodetic residual geoid on approximately 3×3 km grid 100
7.6 Statistics of combined residual geoid on approximately 3×3 km grid 102
7.7 Statistics of post-fit residuals 106
7.8 Statistics of gravimetric geoid validation with 192 GPS/leveling observations and with the Austrian geoid 108
7.9 Statistics of validation with 192 geopotential numbers 109
7.10 Statistics of astrogeodetic geoid validation with 192 GPS/leveling observations and with the Austrian geoid 110
7.11 Statistics of combined geoid validation with 192 GPS/leveling observations and with the Austrian geoid 111
7.12 Statistics of the gravity differences between the normal and the GGM gravity . 113
7.13 Statistics of the gravity differences of full gravity vector and linearized approach for topographic effects 114

7.14 Statistics of the gravity differences of accumulated effects 115
7.15 Statistics of occurring geoid height differences caused by accumulated effects . 115
7.16 Statistics of gravity and geoid validation with GPS/leveling observations 117
7.17 Statistics of reduced gravity differences caused by different DTM resolutions . . 118
7.18 Statistics of geoid height differences caused by different DTM resolutions 119
7.19 Statistics of differences in reduced gravity data due to the consideration of a global DTM and remaining effect in geoid heights after full restore step 121
7.20 Statistics of geoid validation with the Austrian geoid and with GPS/leveling observations 123
7.21 Statistics of the reduced gravity subsets and the corresponding geoid validation 125
7.22 Statistics of 72327 reduced gravity observations, once with and once without isostasy from d/o 251 $\rightarrow$ 500 125
7.23 Statistics of geoid validation with GPS/leveling observations; Once with and once without isostasy considered from d/o 251 $\rightarrow$ 500 126
7.24 Statistics of the gridded map values and corresponding validation with 735 measured deflections of the vertical 127

Bibliography

Abd-Elmotaal H (1995) Attraction of topographic masses. Journal of Geodesy vol 4(69) p. 304–307, url: http://dx.doi.org/10.1007/BF00806743

Alberts B (2009) Regional gravity field modeling using airborne gravimetry data. PhD thesis, Technical University Delft, Delft, The Netherlands, url: http://www.citg.tudelft.nl

Becker JJ, Sandwell DT, Smith WHF, Braud J, Binder B, Depner J, Fabre D, Factor J, Ingalls S, Kim SH, Ladner R, Marks K, Nelson S, Pharaoh A, Sharman G, Trimmer R, VonRosenburg J, Wallace G, Weatherall P (2009) Global Bathymetry and Elevation Data at 30 Arc Seconds Resolution: SRTM30 PLUS. Journal of Marine Geodesy vol 32(4) p. 355–371, url: http://dx.doi.org/10.1080/01490410903297766

Behm M, Lippitsch R, Kissling E, Brückl E, Grad M, Sumanovac F (2008) A new Moho map for the entire Alpine region. Presented at EGU, General Assembly 2008, Geophysical Research Abstracts, EGU2008-A-10151, Vienna, Austria

Bentel K, Schmidt M, Gerlach C (2013) Different radial basis functions and their applicability for regional gravity field representation on the sphere. GEM - International Journal on Geomathematics vol 4 p. 67–96, url: http://dx.doi.org/10.1007/s13137-012-0046-1

BEV (2007) Schweredatenaustausch - Schnittstellenbeschreibung url: http://www.bev.gv.at/pls/portal/docs/PAGE/BEV_PORTAL_CONTENT_ALLGEMEIN/0200_PRODUKTE/PDF/BEV_S_GV_SCHWEREDATENAUSTAUSCH_V1_0.pdf, online, accessed 19-June-2016

Bjerhammer A (1969) On the boundary value problem of physical geodesy. Tellus vol 21(4) p. 451–516, url: http://dx.doi.org/10.1111/j.2153-3490.1969.tb00460.x

Bretterbauer K, Gerstbach G (1983) Die astro-geodätische Arbeiten der TU-Wien, Das Geoid in Österreich - Geodätische Arbeiten Österreichs für die internationale Erdmessung, vol 3. Wien, Österreich

Briese C, Höggerl N, Imrek E, Otter J, Ruess D (2011) Transformation von GNSS-Höhen in österreichische Gebrauchshöhen mittels einer Transformationsfläche (Höhen-Grid). Österreichische Zeitschrift für Vermessung und Geoinformation (VGI) vol 4 p. 267–281, Wien, Österreich

Bruns H (1878) Die Figur der Erde. Publikationen des Preussischen Geodätischen Instituts, Berlin, Deutschland

Bürki B, Müller A, Kahle H (2004) DIADEM: The New Digital Astronomical Deflection Measuring System for High Precision Measurements of Deflections of the Vertical at ETH Zurich. Electronic Proceeding, Proceedings of the the IAG GGSM2004 Meeting, p. n/a–n/a, Porto, Portugal

Christensen NI, Mooney WD (1995) Seismic velocity structure and composition of the continental crust: A global view. Journal of Geophysical Research: Solid Earth vol 100(6) p. 9761–9788, url: http://dx.doi.org/10.1029/95JB00259

Denker H (1988) Hochauflösende regionale Schwerefeldbestimmung mit gravimetrischen und topographischen Daten. PhD thesis, Wiss. Arb. der Fachr. Vermessungswesen der Univ. Hannover Nr. 156, Hannover, Germany

Denker H, Torge W (1998) The European Gravimetric Quasigeoid EGG97 - An IAG Supported Continental Enterprise. In: Forsberg R, Feissel M, Dietrich R (eds) Geodesy on the Move, International Association of Geodesy Symposia, vol 119, Springer Berlin Heidelberg, p. 249–254, url: http://dx.doi.org/10.1007/978-3-642-72245-5_36

Drinkwater M, Floberghagen R, Haagmans R, Muzi D, Popescu A (2003) GOCE: ESAs First Earth Explorer Core Mission. In: Beutler G, Drinkwater M, Rummel R, Von Steiger R (eds) Earth Gravity Field from Space - From Sensors to Earth Sciences, Space Sciences Series of ISSI, vol 17, Springer Netherlands, p. 419–432, url: http://dx.doi.org/10.1007/978-94-017-1333-7_36

Eicker A (2008) Gravity Field Refinements by Radial Basis Functions from In-situ Satellite Data. PhD thesis, Rheinischen Friedrich-Wilhelms-Universität, Bonn, Germany, url: http://hss.ulb.uni-bonn.de/2008/1375/1375.pdf

Eicker A, Mayer-Gürr T, Ilk KH, Kurtenbach E (2010) Regionally refined gravity field models from in-situ satellite data. In: Flechtner F, Gruber T, Güntner A, Mandea M, Rothacher M, Schöne T, Wickert J (eds) System Earth via Geodetic-Geophysical Space Techniques, Springer Berlin Heidelberg, p. 255–264, url: http://dx.doi.org/10.1007/978-3-642-10228-8_20

Erker E (1987) The Austrian Geoid - Local Geoid Determination using Modified Conservative Algorithm, Gravity Field in Austria - Geodätische Arbeiten Österreichs für die Internationale Erdmessung, vol 4. Wien, Österreich

Forsberg R (1984) A study of terrain reductions, density anomalies and geophysical inversion methods in gravity field modelling. OSU Report 355, Ohio State University, Department of Geodetic Science and Surveying, Columbus, USA

Forsberg R, Tscherning C (1997) Geodetic Boundary Value Problems in View of the One Centimeter Geoid. In: Sanso F, Rummel R (eds) Lecture Notes in Earth Sciences, Springer Berlin Heidelberg, p. 239–272, url: http://dx.doi.org/10.1007/BFb0011707

Förste C, Flechtner F, Schmidt R, Stubenvoll R, Meyer U, König R, Barthelmes F, Neumayer H, Biancale R (2006) A mean global gravity field model from the combination of satellite mission and altimetry/gravimetry surface data. Presented at EGU, General Assembly 2006, Geophysical Research Abstracts, Vol 8, EGU2006-03462, Vienna, Austria

Förste C, Schmidt R, Stubenvoll R, Flechtner F, Meyer U, König R, Neumayer H, Biancale R, Lemoine JM, Bruinsma S, Loyer S, Barthelmes F, Esselborn S (2008) The geoforschungszentrum potsdam/groupe de recherche de geodesie spatiale satellite-only and combined gravity field models: Eigen-gl04s1 and eigen-gl04c. Journal of Geodesy vol 82(6) p. 331–346, url: `http://dx.doi.org/10.1007/s00190-007-0183-8`

Freeden W (1985) Computation of spherical harmonics and approximation by spherical harmonic expansion. OSU Report 362, Ohio State University, Department of Geodetic Science and Surveying, Columbus, USA

Freeden W (1999) Multiscale Modelling of Spaceborne Geodata. BG Teubner, Stuttgart, Leipzig, Germany

Freeden W, Törnig W (1981) On spherical spline interpolation and approximation. Mathematical Methods in the Applied Sciences vol 3(1) p. 551–575, url: `http://dx.doi.org/10.1002/mma.1670030139`

Graf J (1996) Das digitale Geländemodell für Geoidberechnungen und Schwerereduktionen in Österreich. Österreichische Beiträge zur Meteorologie und Geophysik, Proceedings of the 7^{th} International Meeting on Alpine Gravimetry, p. 121–136, Vienna, Austria

Grombein T, Seitz K, Heck B (2013) Optimized formulas for the gravitational field of a tesseroid. Journal of Geodesy vol 87(7) p. 645–660, url: `http://dx.doi.org/10.1007/s00190-013-0636-1`

Gruber T, Köhl A (2008) Validation of the EGM2008 Gravity Field with GPS-Levelling and Oceanographic Analysis. Presented at IAG International Symposium on Gravity, Geoid and Earth Observation 2008, Chania, Greece

Gruber T, Visser P, Ackermann C, Hosse M (2011) Validation of GOCE gravity field models by means of orbit residuals and geoid comparisons. Journal of Geodesy vol 85(11) p. 845–860, url: `http://dx.doi.org/10.1007/s00190-011-0486-7`

Heck B, Seitz K (2003) Solutions of the linearized geodetic boundary value problem for an ellipsoidal boundary to order e^3. Journal of Geodesy vol 77(3) p. 182–192, url: `http://dx.doi.org/10.1007/s00190-002-0309-y`

Heck B, Seitz K (2007) A comparison of the tesseroid, prism and point-mass approaches for mass reductions in gravity field modelling. Journal of Geodesy vol 81(2) p. 121–136, url: `http://dx.doi.org/10.1007/s00190-006-0094-0`

Heiskanen W, Moritz H (1967) Physical Geodesy. W.H. Freeman and Company, San Francisco, USA

Higham N (1987) A survey of condition number estimation for triangular matrices. SIAM Review vol 9(4) p. 575–596, url: http://dx.doi.org/10.1137/1029112

Hirt C, Kuhn M (2014) Band-limited topographic mass distribution generates full-spectrum gravity field: Gravity forward modeling in the spectral and spatial domains revisited. Journal of Geophysical Research: Solid Earth vol 119(4) p. 3646–3661, url: http://dx.doi.org/10.1002/2013JB010900

Hirt C, Marti U, Bürki B, Featherstone WE (2010) Assessment of EGM2008 in Europe using accurate astrogeodetic vertical deflections and omission error estimates from SRTM/DTM2006 residual terrain model data. Journal of Geophysical Research: Solid Earth vol 115(B10), url: http://dx.doi.org/10.1029/2009JB007057

Hobson E (1931) The theory of spherical and ellipsoidal harmonics. University Press, Cambridge, UK

Hofmann-Wellenhof B, Moritz H (2006) Physical Geodesy. Springer, Wien, New York, Graz, Austria

Kaula WM (1966) Theory of Satellite Geodesy. Blaisdell, Waltham, Toronto, London, UK

Kern M, Schwarz K, Sneeuw N (2003) A study on a combination of satellite, airborne and terrestrial gravity data. Journal of Geodesy vol 77(3-4), url: http://dx.doi.org/10.1007/s00190-003-0313-x

Klees R, Kusche J (2002) Regularization of gravity field estimation from satellite gravity gradients. Journal of Geodesy vol 76 p. 359–368, url: http://dx.doi.org/10.1007/s00190-002-0257-6

Klees R, Prutkin I (2010) The combination of GNSS-levelling data and gravimetric quasigeoid heights in the presence of noise. Journal of Geodesy vol 84(12) p. 731–749, url: http://dx.doi.org/10.1007/s00190-010-0406-2

Koch K, Kusche J (2002) Regularization of geopotential determination from satellite data by variance components. Journal of Geodesy vol 76(5) p. 259–268, url: http://dx.doi.org/10.1007/s00190-002-0245-x

Kuhn M (2000) Geoidbestimmung unter Verwendung verschiedener Dichtehypothesen. PhD thesis, University of Karlsruhe, Karlsruhe, Germany, url: https://katalog.ub.uni-leipzig.de/Record/0004317548

Kuhn M, Hirt C (2016) Topographic gravitational potential up to second-order derivatives: an examination of approximation errors caused by rock-equivalent topography (RET). Journal of Geodesy 90(9) p. 883–902, url: http://dx.doi.org/10.1007/s00190-016-0917-6

Kuhn M, Seitz K (2010) Comparison of Newtons integral in the space and frequency domains. Sanso F (ed) A window on the Future of Geodesy-IAG Symposia vol 128(8) p. 386–391, url: http://dx.doi.org/10.1007/3-540-27432-4_66

Kühtreiber N (1998a) Precise geoid determination using a density variation model. Physics and Chemistry of the Earth vol 23(1) p. 59–63, url: http://dx.doi.org/10.1016/S0079-1946(97)00242-5

Kühtreiber N (1998b) The Geoid for the Central Part of the Alps-Adria Area. In: Proceedings of the 2^{nd} International Symposium Geodynamics of the Alps-Adria Area by means of Terrestrial and Satellite Methods, p. 153–162, Dubrovnik, Croatia

Kühtreiber N (2002) High Precision Geoid Determination of Austria Using Heterogeneous Data. In: Proceedings of the 3^{rd} International Gravity and Geoid Commission, p. 144–149, Thessaloniki, Greece

Kühtreiber N, Abd-Elmotaal H (2007) Ideal Combination of Deflection Components and Gravity Anomalies for Precise Geoid Computation. In: Tregoning P, Rizos C (eds) Dynamic Planet, International Association of Geodesy Symposia, vol 130, Springer Berlin Heidelberg, p. 259–265, url: http://dx.doi.org/10.1007/978-3-540-49350-1_39

Kühtreiber N, Pail R, Wasle B, Pock C, Wirnsberger H, Hofmann-Wellenhof B, Of G, Steinbach O, Hoeggerl N, Imrek E, Ruess D, Ullrich C (2011) Improved Austrian geoid solution combining terrestrial and satellite gravity data (GEOID+). Tech. rep., ASAP Phase VI Project - Final Report, Graz, Austria

Litschauer J (1953) Zur Frage der Geoidgestalt in Österreich. Österreichische Zeitschrift für Vermessungswesen vol 80 p. 161–172, Wien, Österreich

Mader K (1951) Das Newtonsche Raumpotential prismatischer Körper und seine Ableitungen bis zur dritten Ordnung. Österreichische Zeitschrift für Vermessungswesen - Österreichische Kommission für internationale Erdmessung, Sonderheft 11 p. 74, Wien, Österreich

Mäkinen J (2008) The treatment of permanent tide in EUREF products. Presented at the Symposium of the IAG Sub-commission for Europe (EUREF), Brussels, Belgium

Marti U, Schlatter A (2002) Höhenreferenzsysteme und -Rahmen. Vermessung, Photogrametrie, Kulturtechnik (VPK) vol 100, url: http://dx.doi.org/10.5169/seals-235866

Mayer-Gürr T, Pock C (2015) Brauchen wir eine neue Definition der Schwereanomalien? Presented at German Geodetic Week 2015, Stuttgart, Germany

Mayer-Gürr T, Rieser D, Hoeck E, Brockmann J, Schuh WD, Krasbutter I, Kusche J, Maier A, Krauss S, Hausleitner W, Baur O, Jaeggi A, Meyer U, Prange L, Pail R, Fecher T, Gruber T (2015) The combined satellite only model GOCO05s. Presented at EGU, General Assembly 2015, Geophysical Research Abstracts, Vol 17, EGU2015-12364, Vienna, Austria

Mayerhofer M (2007) Erstellung eines Geländemodells für Mitteleuropa. Master Thesis, Graz University of Technology

Metzler B (2007) Spherical Cap Regularization - A Spatially Restricted Regularization Method Tailored to the Polar Gap Problem. PhD thesis, Graz University of Technology, Graz, Austria

Meurers B, Ruess D (2007) A new Bouguer gravity map of Austria. Presented at EGU, General Assembly 2007, Geophysical Research Abstracts, Vol 8, 06230, Vienna, Austria

Meurers B, Ruess D, Graf J (2001) A program system for high precise Bouguer gravity determination. In: Proceedings 8^{th} Int. Meeting on Alpine Gravimetry, Österreichische Beiträge zur Meteorologie und Geophysik, p. 217–226, Leoben, Österreich

Montenbruck O, Gill E (2000) Satellite orbits: models, methods, and applications, 1st edn. Springer, Heidelberg New York, Germany

Moritz H (1962) Interpolation and prediction of gravity and their accuracy. Tech. rep., Institute of Geodesy, Photogrammetry and Cartography, Ohio State University, Columbus, USA

Moritz H (1980a) Advanced Physical Geodesy, second edition edn. Herbert Wichmann Verlag, Karlsruhe, Germany

Moritz H (1980b) Geodetic reference system 1980. Bulletin Geodesique vol 54 p. 395–405

Naeimi M (2013) Inversion of Satellite Gravity Data Using Spherical Radial Basis Functions. PhD thesis, University of Hannover, Hannover, Germany, url: `http://www.dgk.badw.de/fileadmin/docs/c-711.pdf`

Nagy D (1966) The prism method for terrain corrections using digital computers. Pure and applied Geophysics vol 63(1) p. 31–39, url: `http://dx.doi.org/10.1007/BF00875156`

NOAA, NASA, USAF (1976) U.S. Standard Atmosphere 1976. Tech. rep., Government Printing Office, Washington, USA

Pail R, Kühtreiber N, Wiesenhofer B, Hofmann-Wellenhof B, Of G, Steinbach O, Hoeggerl N, Ruess D, Ullrich C (2007) The Austrian Geoid 2007 (GEOnAUT). Tech. rep., ASAP Phase III Project - Final Report, Graz, Austria

Pail R, Kühtreiber N, Wiesenhofer B, Hofmann-Wellenhof B, Of G, Steinbach O, Hoeggerl N, Ruess D, Ullrich C (2008) The Austrian Geoid 2007. Österreichische Zeitschrift für Vermessung und Geoinformation (VGI) vol 96(1) p. 3–14, Wien, Österreich

Pail R, Kühtreiber N, Wiesenhofer B, Hofmann-Wellenhof B, Ullrich C, Hoeggerl N, Imrek E, Ruess D (2009) The official Austrian geoid solution 2008: Data Method and Results. Presented at EGU, General Assembly 2009, Geophysical Research Abstracts, Vol 11, EGU2009-2974, Vienna, Austria

Pail R, Goiginger H, Schuh WD, Höck E, Brockmann JM, Fecher T, Gruber T, Mayer-Gürr T, Kusche J, Jäggi A, Rieser D (2010) Combined satellite gravity field model GOCO01s derived from GOCE and GRACE. Geophysical Research Letters vol 37(20), url: `http://dx.doi.org/10.1029/2010GL044906`

Pavlis NK, Holmes SA, Kenyon SC, Factor JK (2008) An Earth Gravitational Model to Degree 2160: EGM2008. Presented at EGU, General Assembly 2008, Geophysical Research Abstracts, Vol 10, EGU2008-A-01891, Vienna, Austria

Pavlis NK, Holmes SA, Kenyon SC, Factor JK (2012) The development and evaluation of the Earth Gravitational Model 2008 (EGM2008). Journal of Geophysical Research: Solid Earth vol 117(B4), url: `http://dx.doi.org/10.1029/2011JB008916`

Pock C (2011) Problemstellungen bei der Verwendung des Geoids als Transformationsfläche zwischen ellipsoidischen und orthometrischen Höhen. Master Thesis, Graz University of Technology, Graz, Austria

Pock C, Mayer-Gürr T, Kühtreiber N (2014) Consistent Combination of Satellite and Terrestrial Gravity Field Observations in Regional Geoid Modeling: A Case Study for Austria. In: Marti U (ed) Gravity, Geoid and Height Systems, International Association of Geodesy Symposia, vol 141, Springer International Publishing, p. 151–156, url: `http://dx.doi.org/10.1007/978-3-319-10837-7_19`

Reigber C, Lühr H, Schwintzer P (2002) Champ mission status. Advances in Space Research vol 30(2) p. 129–134, url: `http://dx.doi.org/10.1016/S0273-1177(02)00276-4`

Rieser D (2015) GOCE gravity gradients for geoid and Moho determination applying the Least Squares Collocation approach. PhD thesis, Graz University of Technology, Graz, Austria

Rinner K (1983) Stand und Zielsetzung der Geoidforschung in Österreich, Das Geoid in Österreich - Geodätische Arbeiten Österreichs für die internationale Erdmessung, vol 3. Wien, Österreich

Ruess D (1983) Aufbau des österreichischen Schweregrundnetzes ÖSGN. Presented at 3^{rd} Internationales Alpengravimetrie Kolloquium, Leoben, Österreich

Ruess D (1984) Ein digitales Höhenmodell von Österreich, Geodätische Arbeiten Österreichs für die internationale Erdmessung, vol 3. Wien, Österreich

Ruess D (1995) Das Schweregrundnetz in Österreich. EVM- Eich und Vermessungsmagazin vol 80 p. 24–36, Wien, Österreich

Ruess D (2001) Aufbau des orthometrischen Höhensystems mit verfeinerten Methoden der Schwereredukton. In: Proceedings 8^{th} Int. Meeting on Alpine Gravimetry, Leoben, Österreich, Österreichische Beiträge zur Meteorologie und Geophysik

Ruess D, Mitterschiffthaler P (2015) Rezente Höhenänderungen in Österreich abgeleitet aus geodätischen Wiederholungsmessungen. In: Proceedings of the 18^{th} Int. Geodetic Week Obergurgl, Herbert Wichmann Verlag, Berlin Offenbach, Deutschland

Ruess D, Ulrich C (2011) 20 years of International Comparison of Absolute Gravimeters (ICAG) at the Bureau International des Poids et Mesures (BIPM) in Paris with participation of the BEV. Österreichische Zeitschrift für Vermessung und Geoinformation (VGI) vol 99(2) p. 154–161, Wien, Österreich

Rülke A, Liebsch G, Sacher M, Schaefer U, Schirmer U, Ihde J (2013) Unification of European height system realizations. Journal of Geodetic Science vol 2(4) p. 343–354, url: `http://dx.doi.org/10.2478/v10156-011-0048-1`

Rummel R, Rapp R, Sünkel H, Tscherning C (1988) Comparisons of global topographic/isostatic models to the Earth's observed gravity field. OSU Report 388, Ohio State University, Department of Geodetic Science and Surveying, Columbus, USA

Sacher M, Ihde J, Celms A, Ellmann A (1999) The first UELN stage is achieved - further steps are planed. In: Report on the Symposium of the IAG Sub-commission for Europe (EUREF), Veröffentlichung der Bayerischen Kommission für die Internationale Erdmessung, vol 60, p. 87–94, Prague, Czech Republik

Schmidt H (1981) Sampling function and finite element method representation of the gravity field. Reviews of Geophysics vol 19(3) p. 421–436, url: `http://dx.doi.org/10.1029/RG019i003p00421`

Schwarz K, Sideris M, Forsberg R (1990) The use of FFT techniques in physical geodesy. Geophysical Journal International vol 100 p. 485–514, url: `http://dx.doi.org/10.1111/j.1365-246X.1990.tb00701.x`

Sjöberg LE (1999) The IAG approach to the atmospheric geoid correction in Stokes formula and a new strategy. Journal of Geodesy vol 73(7) p. 362–366, url: `http://dx.doi.org/10.1007/s001900050254`

Sjöberg LE (2010) A strict formula for geoid-to-quasigeoid separation. Journal of Geodesy vol 84 p. 699–702, url: `http://dx.doi.org/10.1007/s00190-010-0407-1`

Smith B, Sandwell D (2003) Accuracy and resolution of shuttle radar topography mission data. Geophysical Research Letters vol 30(9) p. n/a–n/a, url: `http://dx.doi.org/10.1029/2002GL016643`, 1467

Somigliana C (1929) Teoria generale del campo gravitazion ale dell ellisoide di rotazione. Mem Soc Astron Ital vol 6

Sünkel H, Bartelme N, Fuchs H, Hanafy M, Schuh W, Wieser M (1987) The Gravity Field in Austria. Austrian Geodetic Commission - Geodätische Arbeiten Österreichs für die Internationale Erdmessung vol 4 p. 47–75, Graz, Österreich

Tapley B, Bettadpur S, Watkins M, Reigber C (2004) The gravity recovery and climate experiment: Mission overview and early results. Geophysical Research Letters vol 31(9), url: http://dx.doi.org/10.1029/2004GL019920

Tikhonov A (1963) Solution of incorrectly formulated problems and the regularization method. Soviet Mathematics Doklady vol 4 p. 1035–1038

Tsoulis D (1999) Spherical Harmonic Computations with Topographic-Isostatic Coefficients. Tech. rep., Reports in the series IAPG/FESG, Munich, Germany

Tziavos I, Sideris M, Sünkel H (1996) The effect of surface density variation on terrain modeling - A case study in Austria. Proceedings of the European Geophysical XXI EGS General Assembly, The Hague, The Netherlands

USGS (2014) GTOPO30 Documentation. url: https://lta.cr.usgs.gov/GTOPO30, online, accessed 19-June-2016

Wiesenhofer B (2007) Untersuchungen zur astrogeodätischen Geoidlösung im Südosten Österreichs. Master Thesis, Graz University of Technology

Wild-Pfeiffer F (2007) Auswirkungen topographisch-isostatischer Massen auf die Satellitengradiometrie. PhD thesis, University of Karlsruhe, Karlsruhe, Germany, url: http://www.dgk.badw.de/fileadmin/docs/c-604.pdf

Wittwer T (2009) Regional gravity field modelling with radial basis functions. PhD thesis, TU Delft, Delft, The Netherlands, url: http://www.citg.tudelft.nl/fileadmin/Faculteit/CiTG/Over_de_faculteit/Afdelingen/Afdeling_Geoscience_and_Remote_Sensing/Physical_Space_Geodesy/img/Regional_gravity_field_modelling_with_radial_basis_functions_-_PhD_thesis_Tobias_Wittwer.pdf

Wolf KI (2007) Kombination globaler Potentialmodelle mit terrestrischen Schweredaten für die Berechnung der zweiten Ableitungen des Gravitationspotentials in Satellitenbahnhöhe. PhD thesis, University of Hannover, Hannover, Germany, url: http://www.dgk.badw.de/fileadmin/docs/c-603.pdf